LAPPEENRANTA
UNIVERSITY OF TECHNOLOGY

Ahti Jaatinen

Performance Improvement of Centrifugal Compressor Stage with Pinched Geometry or Vaned Diffuser

Thesis for the degree of a Doctor of Science (Technology) to be presented with due permission for public examination and criticism in Auditorium 1383 at Lappeenranta University of Technology, Lappeenranta, Finland, on the 1st of October 2009, at noon.

Acta Universitatis
Lappeenrantaensis
352

Supervisor Jari Backman
Laboratory of Fluid Dynamics
Institute of Energy Technology
Lappeenranta University of Technology
Finland

Reviewers Professor Timo Siikonen
Department of Applied Mechanics
Helsinki University of Technology
Finland

Professor Jörg Seume
Institut für Strömungsmaschinen und Fluid Dynamik - TFD
Leibniz Universität Hannover
Germany

Opponent Professor Jörg Seume
Institut für Strömungsmaschinen und Fluid Dynamik - TFD
Leibniz Universität Hannover
Germany

ISBN 978-952-214-820-9
ISBN 978-952-214-821-6 (PDF)
ISSN 1456-4491
Lappeenrannan teknillinen yliopisto
Digipaino 2009

Abstract

Ahti Jaatinen
Performance Improvement of Centrifugal Compressor Stage with Pinched Geometry or Vaned Diffuser
Lappeenranta 2009
152 pages
Acta Universitatis Lappeenrantaensis 352
Diss. Lappeenranta University of Technology
ISBN 978-952-214-820-9, ISBN 978-952-214-821-6 (PDF), ISSN 1456-4491

Centrifugal compressors are widely used for example in refrigeration processes, the oil and gas industry, superchargers, and waste water treatment. In this work, five different vaneless diffusers and six different vaned diffusers are investigated numerically. The vaneless diffusers vary only by their diffuser width, so that four of the geometries have pinch implemented to them. Pinch means a decrease in the diffuser width. Four of the vaned diffusers have the same vane turning angle and a different number of vanes, and two have different vane turning angles. The flow solver used to solve the flow fields is Finflo, which is a Navier-Stokes solver. All the cases are modeled with the Chien's $k-\epsilon$ turbulence model, and selected cases are modeled also with the $k-\omega$-SST turbulence model.

All five vaneless diffusers and three vaned diffusers are investigated also experimentally. For each construction, the compressor operating map is measured according to relevant standards. In addition to this, the flow fields before and after the diffuser are measured with static and total pressure, flow angle and total temperature measurements.

When comparing the computational results to the measured results, it is evident that the $k-\omega$-SST turbulence model predicts the flow fields better. The simulation results indicate that it is possible to improve the efficiency with the pinch, and according to the numerical results, the two best geometries are the ones with most pinch at the shroud. These geometries have approximately 4 percentage points higher efficiency than the unpinched vaneless diffusers. The hub pinch does not seem to have any major benefits. In general, the pinches make the flow fields before and after the diffuser more uniform. The pinch also seems to improve the impeller efficiency. This is down to two reasons. The major reason is that the pinch decreases the size of slow flow and possible backflow region located near the shroud after the impeller. Secondly, the pinches decrease the flow velocity in the tip clearance, leading

to a smaller tip leakage flow and therefore slightly better impeller efficiency. Also some of the vaned diffusers improve the efficiency, the increment being 1...3 percentage points, when compared to the vaneless unpinched geometry.

The measurement results confirm that the pinch is beneficial to the performance of the compressor. The flow fields are more uniform with the pinched cases, and the slow flow regions are smaller. The peak efficiency is approximately 2 percentage points and the design point efficiency approximately 4 percentage points higher with the pinched geometries than with the unpinched geometry. According to the measurements, the two best geometries are the ones with the most pinch at the shroud, the case with the pinch only at the shroud being slightly better of the two. The vaned diffusers also have better efficiency than the vaneless unpinched geometries. However, the pinched cases have even better efficiencies. The vaned diffusers narrow the operating range considerably, whilst the pinch has no significant effect on the operating range.

Keywords: centrifugal compressor, diffuser, diffuser width, pinch, vaned diffuser, computational fluid dynamics
UDC 62-226.3

Acknowledgements

I like would like to express my gratitude to professors Jaakko Larjola and Jari Backman for offering the possibilty to do this research, supervising it and guiding the process. Also the great influence of D.Sc Teemu Turunen-Saaresti on this work should be recognized. His insights, ideas and general guidance were magnificent throughout the process.

Also without naming any names, all the colleagues in the laboratory of Fluid Dynamics at Lappeenranta University of Technology must mentioned, for just being nice people to work with. The efforts of laboratory technicians Petteri Pesonen and Erkki Nikku should be mentioned for their tireless efforts in assembling, reassembling and disassembling the compressor during the measurements.

I expresse my sincere gratitude for the reviewers, professor Jörg Seume of Leibniz Universität Hannover and professor Timo Siikonen of Helsinki University of Technology for their meaningful insights and comments about this work.

I gratefully acknowledge the financial contributions of the Academy of Finland, the Finnish Funding Agency for Technology and Innovation - TEKES, and High Speed Tech Oy Ltd. Also the contribution of the CSC - IT Center for Science should be mentioned, for providing some of the computational resources used in this work.

Lastly, I would like to thank all my mates, without whom this work would have been done some years ago, but where is the fun in that? You know who you are.

Ahti Jaatinen
September 2009
Lappeenranta, Finland

Contents

Nomenclature

Latin alphabet

a	constant in $k-\omega$-SST turbulence model equations	
b	diffuser width	m
C	coefficient of discharge	
c	absolute flow velocity	m/s
c	chord length	m
C_1	closure coefficient in $k-\epsilon$ turbulence model	
C_2	closure coefficient in $k-\epsilon$ turbulence model	
C_μ	closure coefficient in $k-\epsilon$ turbulence model	
c_p	specific heat capacity in constant pressure	J/kgK
C_pr	diffuser static pressure rise coefficient	
D	diameter	m
d	diameter	m
E	empirical function in $k-\epsilon$ turbulence model	
E	relative uncertainty	%
e	measurement uncertainty	
F_1	blending function in eq. 3.21	
F_1	blending function in eqs. 3.8 and 3.11	
f_1	empirical function in $k-\epsilon$ turbulence model	
f_2	empirical function in $k-\epsilon$ turbulence model	
f_μ	empirical function in $k-\epsilon$ turbulence model	
k	kinetic energy of turbulence	J/kg
K_p	diffuser total pressure loss coefficient	

N	number of vanes in a diffuser	
N	rotational speed	1/s, rpm
p	pressure	Pa
q_{m}	mass flow	kg/s
R	specific gas constant	J/kgK
r	radius	m
R_{H}	relative humidity	%
s	distance between two diffuser vanes	m
t	time	s
u	mean velocity	m/s
x	position vector	
y	y-coordinate	
m	meridional distance	m

Greek alphabet

α	flow angle (from radial direction)	$^\circ$
β	closure coefficent in turbulence models	
β	diameter ratio	
Δ	difference	
ϵ	dissipation of kinetic energy of turbulence	W/kg
ϵ	expansibilty factor	
ϵ_o	empirical function in $k-\epsilon$ turbulence model	
η	isentropic efficiency	
γ	closure coefficent in turbulence models	
μ	molecular viscosity	kg/ms
μ_{T}	dynamic eddy viscosity	kg/ms

ν_{T}	kinematic eddy viscosity	$\mathrm{m^2/s}$
Ω	absolute value of vorticity	
ω	specific dissipation rate	$\mathrm{m^4/s^3}$
ω_{v}	water vapor content	
π	pressure ratio	
ρ	density	$\mathrm{kg/m^3}$
σ	solidity	
σ_ϵ	closure coefficient in turbulence models	
σ_{k}	closure coefficient in turbulence models	
τ	shear stress	$\mathrm{N/m^2}$
θ	diffuser vane turning angle	$^\circ$
φ	relative humidity	%

Subscripts

1	compressor inlet
2	impeller exit
$2'$	diffuser inlet
2^*	measurement radius after impeller
3	diffuser vane trailing edge
4	diffuser exit
5	compressor exit
cr	critical
i	tensor notation
j	tensor notation
n	normal component
ref	reference value

r radial component

s isentropic

t tangential component

t total state

w wall

Abbreviations

BSL baseline $k - \omega$ turbulence model

CFD computational fluid dynamics

CVD conventional vaned diffuser

DDADI diagonally dominant alternating direction implicit

DNS direct numerical solution

EARSM explicit algebraic Reynolds stress models

LES large eddy simulation

LSVD low solidity vaned diffuser

LUT Lappeenranta University of Technology

MUSCL monotonic upwind schemes for conservation laws

NACA National Advisory Comittee for Aeronautics

NASA National Aeronautics and Space Administration

PVD partially vaned diffuser

RSM Reynolds stress models

SST shear-stress transport

TKK Helsinki University of Technology

1 Introduction

Centrifugal compressors are widely used in industrial applications where a continuous flow of pressurized gas is required. They are widely used for example in combustion engine superchargers, refigeration processes and plants, the oil and gas industry, waste water treatment plants and in smaller gas turbines. It is quite easy to achieve pressure ratios up to 4 per single stage with a centrifugal compressor, which is considerable more than the typical pressure ratio of below 1.2 for an axial compressor stage. Therefore, a centrifugal compressor is smaller in physical size than an axial compressor with the same pressure ratio. Centrifugal compressors are easier and cheaper to manufacture. However, better efficiency is achieved with an axial compressor, and they are usually used in applications, such as large gas turbines, where the input power is signifcant.

A typical construction of a process centrifugal compressor consists of an inlet cone, an impeller, a diffuser, a volute or a collecting chamber, and an exit cone. The inlet and exit cones are usually used to connect the compressor to the piping. They are not neccessary, however. The input energy is transferred to the gas in the impeller. The area of the flow passage, formed by two adjacent impeller blades in the impeller, increases from the impeller inlet to the impeller outlet. This leads to decreasing relative velocity, which then leads to an increase in the static pressure. The flow leaving the impeller has a substantial amount of kinetic energy, usually around 30 to 40% of the total work input in the impeller. In order to achieve good efficiency, as much as possible of this kinetic energy must be converted into static pressure, and that is where diffusers are used. The diffuser has two main working principles. It either increases the flow area, which decreases the velocity, thus increasing the static pressure, or changes the mean flow path radius, which decreases the tangential velocity and increases the static pressure. A volute or a collecting chamber are not necessary, but either one is usually used to collect the gas coming from the diffuser to a single outlet.

Centrifugal compressor diffusers have two major categories. They can be either vaneless or vaned. A vaneless diffuser is in its most simple form just two parallel plates, leading to an increase in the flow area as the radius increases. Vaned diffusers, which can be divided to subcategories based on the design principle or geometry, change the mean flow path radius. Vaneless diffusers are used where a large operation range is needed and the manufacturing costs must be kept at the minimum. Better efficiency can be achieved with vaned diffusers, but they narrow the operating range significantly and

are much more expensive to manufacture. Vaned diffusers are typically used with higher pressure ratios and in applications where the need to adjust the flow rate is not a top priority.

The Laboratory of Fluid Dynamics at Lappeenranta University of Technology (LUT) has nearly thirty years of experience in studying and designing high speed centrifugal compressors, and for instance three of the five doctoral dissertations made in the laboratory have conserned with centrifugal compressors. In this study, an industrial one-stage centrifugal compressor is studied both numerically and experimentally. Computational fluid dynamics (CFD) is used to study the effect of diffuser width on the performance of the compressor. A vaneless diffuser is narrowed from the shroud wall or from both the hub and the shroud walls. The decrease in the diffuser width is called pinch. Five different vaneless configurations are investigated numerically: an unpinched basic geometry and four different pinched vaneless diffusers. Also the effects of different vaned diffusers are studied. Six different vaned diffusers, varying by the number of diffuser vanes and vane turning angle, are modeled numerically. The overall performance of the compressor and the flow fields before and after the diffuser are studied in the numerical part. The results are compared to the numerical results of the unpinched geometry. Some of the numerical cases are modeled with two different turbulence models, the Chien's $k-\epsilon$ and the $k-\omega$-SST, to achieve information about the differences of said models.

All five vaneless geometries and three of the vaned diffusers are then investigated experimentally. Overall performance measurements and flow field measurements are performed for each geometry, and the results are then compared to those of the vanless unpinched construction. The overall performance measurements are done in accordance with the relevant standards. The flow fields are measured before and after the diffuser with three Kiel probes to measure the total pressure, a cobra probe to measure the total pressure and flow angle, three different total temperature measurements (inserted with the Kiel probes), and in total 11 different static pressure taps. In addition to these, the atmospheric temperature and pressure and the temperatures and pressures before and after the compressor are recorded.

The objectives of this study are:

1. to achieve further understanding of the effect of pinches on the performance of a centrifugal compressors;

2. to achieve further information about the effect of vaned diffuser on the performance of a centrifugal compressor;
3. to gain more information about the differences of the $k-\epsilon$ and the $k-\omega$-SST turbulence models and their suitability for centrifugal compressor modeling;
4. to improve the efficiency of a centrifugal compressor.

The study consists of four general parts. The first one is the introduction and a literature survey in chapters one and two. The second part is the numerical part, which includes a short description of the numerical tools and turbulence models in chapter three and the numerical cases and results in chapter four. The third part contains the measurements. The measurement setup and procedures, measured geometries and the measurement results are described in chapter five. The most important results of this study are summarized and discussed in chapter six, which is the fourth and final part of this study.

The literature survey has been performed solely by the present author. Also the numerical modeling, including pre-processing, actual calculations and post-processing, has been performed entirely by the author, using existing software. Six of the eight measured vaneless and vaned cases were measured by the author. The measurement set-up, instrumentation or procedure were not designed by the author. The six cases measured by the author were also post-processed by him, with the help of a colleague, who measured the other two cases.

2 Centrifugal compressor diffusers

The centrifugal compressor diffuser is located after the impeller and usually before a volute or collector of some sort, and it is designed to convert the excess kinetic energy still existing after the impeller, to pressure. Both the impeller and the volute affect the flow field in the diffuser and the performance of the diffuser, and thus a diffuser should not be designed without considering the other two parts. A poorly designed diffuser can lead to a poor overall performance of the stage or the compressor.

The flow leaving the impeller of the centrifugal compressor is highly distorted. There is a slow flow region near the flow channel suction-side/shroud-side corner with high turbulence and losses, and a region with high radial component c_r near the pressure side with relatively stable flow and low total pressure losses (Eckardt, 1975). This phenomenon is caused by the swirling flow inside the rotor, and a vortex flow of this type is present in any unshrouded impeller (Krain, 1988). Impeller-diffuser interaction has a profound effect on impeller tip leakage flow and therefore on the losses, blockage, slip and pressure rise (Shum et al., 2000). Flow uniformity at the impeller exit becomes worse when the tip clearance increases (Tang, 2006). Also the jet-wake structure of the flow at the impeller exit gets more pronounced at higher rotational speeds and at higher mass flows when the rotational speed is kept constant (Ziegler et al., 2003b), and for a high speed centrifugal compressor the low momentum wake spans from one third to nearly a full impeller passage (Gallier et al., 2007).

The diffuser of the centrifugal compressor also affects the performance of the volute. The flow field after the diffuser affects the losses and pressure recovery of the volute (Van den Braembussche et al., 1999). When the compressor operates at off-design conditions, the circumferential pressure distribution caused by the volute influences the flow in the diffuser and possibly the flow at the impeller exit (Ayder and Van den Braembussche, 1994; Van den Braembussche et al., 1999; Hagelstein et al., 2000).

The diffusers of centrifugal compressors can be divided to two major classes: vaneless and vaned diffusers (see Fig. 2.1). Vaneless diffusers have a wider operating range, lower efficiency and lower pressure recovery than vaned diffusers.

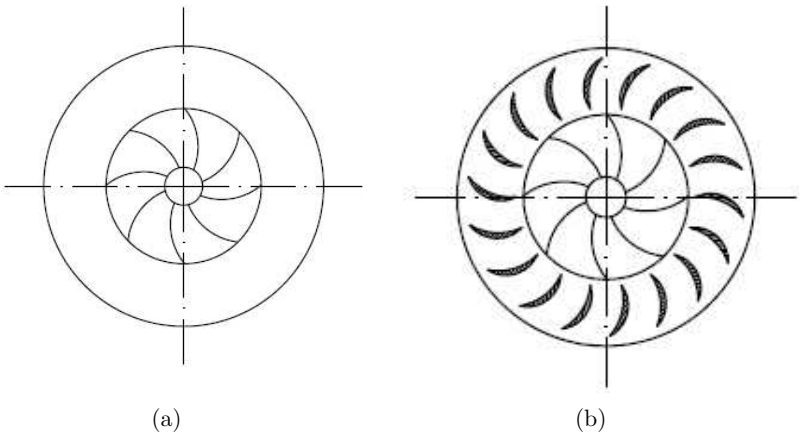

Figure 2.1: Typical diffusers: (a) vaneless and (b) vaned.

2.1 Vaneless diffuser

A vaneless diffuser is a simple geometry consisting of two parallel or almost parallel walls. The diffuser walls form an annular passage from the impeller exit to some outlet diameter. The diffuser inlet may or may not be pinched, which means that the diffuser height is smaller than the channel height at the impeller exit. Different inlet geometries of vaneless diffusers are presented in Fig. 2.2. The most important design criteria affecting the performance of the vaneless diffuser are the channel width and the radius ratio of the diffuser inlet and outlet. The conservation of mass and angular momentum yield

$$rc_{\mathrm{t}} \approx constant \tag{2.1}$$

$$q_{\mathrm{m}} = \rho c_{\mathrm{r}} 2\pi r b \tag{2.2}$$

where c_{t} is the tangential velocity, r is the radius, q_{m} is the mass flow, ρ is the density, c_{r} is the radial velocity, and b is the diffuser width. The definition of the absolute flow angle α in the diffuser is

$$\tan\alpha = \frac{c_{\mathrm{t}}}{c_{\mathrm{r}}} \tag{2.3}$$

Diffuser width b_2/d_2 has a very significant effect on the critical flow angle. The critical flow angle is the maximum diffuser inlet flow angle from radial direction, with which the flow angle at impeller exit does not exceed 90°. Reducing the channel width allows the inlet flow at the diffuser inlet to be

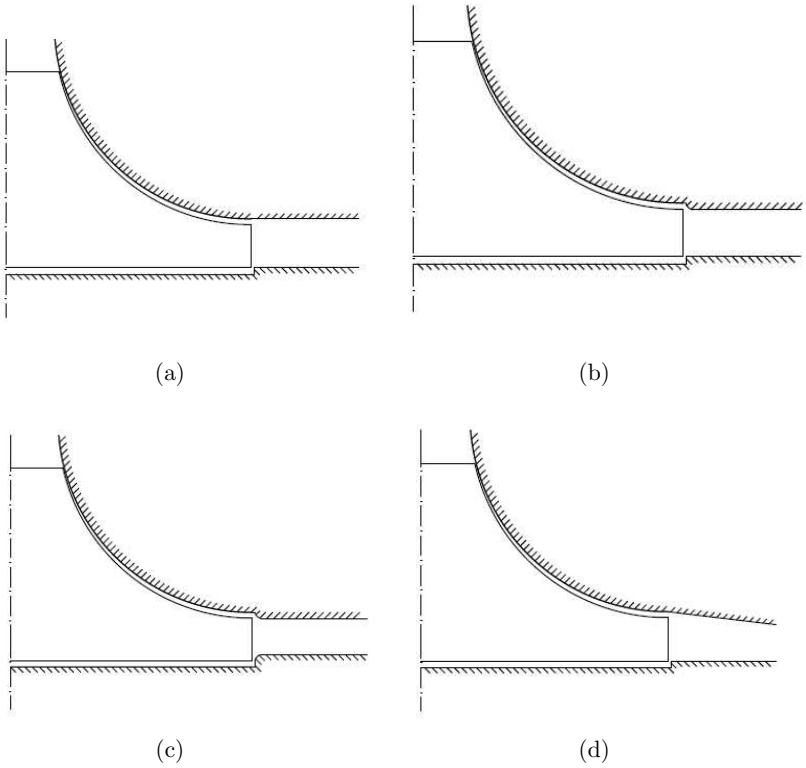

Figure 2.2: Different types of vaneless diffuser inlet geometries: (a) unpinched, (b) shroud pinch, (c) hub and shroud pinch, and (d) constant area diffuser.

more tangential without causing the compressor to stall. A longer diffuser requires more radial flow at the diffuser inlet in order to keep the diffuser at a stable operating range (Senoo and Kinoshita, 1977; Van den Braembuscsche et al., 1980). The same principle applies also to centrifugal blowers (Abidogun, 2002).

Four different vaneless diffusers were studied experimentally by Ludtke (1983). The diffusers were a parallel wall, a highly tapered, a constant area and one parallel wall with the diffuser width reduced by 47%. All the diffusers had the same outlet radius. Ludtke concludes that the diffuser with pinch had

a lower choke limit, lower surge limit and lower peak efficiency compared to the parallel wall diffuser without pinch. He also notes that reducing the diffuser width shifts the peak efficiency points closer to the respective surge points. For the constant area diffuser, the efficiency was slightly lower than with the unpinched parallel wall diffuser. The highly tapered diffuser had lower efficiency than the constant area diffuser, but higher efficiency than the diffuser with reduced width. In another study (Yingkang and Sjolander, 1987), five vaneless diffusers with constant inlet width and outlet diameter ratio but different wall taper angles were tested. One of the tested diffusers was a parallel wall, one had outlet width increased from the parallel wall, and the three others had outlet width reduced from the parallel wall diffuser. Five different impellers were used in the tests. The authors conclude that if the impeller is well-designed and well-matched, the diffuser performance is not that sensitive to details of impeller geometry, such as the number of blades or the outlet sweep angle. All the convergent diffusers had a stabilizing effect on the stability of the compressor. They note that of their limited group of different convergent diffusers, the best was the one with an almost constant area, as was the case with Ludtke's research mentioned above. Finally, the authors conclude that they would recommend that a small amount of convergence should be used routinely when designing vaneless diffusers for centrifugal compressors.

Ferrara et al. (2002a,b) have tested diffusers with three different widths $b_{2'}/b_2$ = 0.30, 0.38 and 0.64 and two different diffuser outlet radius ratios r_4/r_2 of 1.3 and 1.7. Three different pinch inlet profiles were also used in the study: quarter of a circle, almost linear and an ellipse arc. Diffusers have also been tested with two different impellers (Cellai et al., 2003b). In the study of Ferrara et al. (2002a,b) for the radius ratio 1.7, reducing the diffuser width led to increased $\alpha_{2\mathrm{cr}}$, and vice versa for the radius ratio 1.3. The pinch shape had some effect on the critical flow angle. For the radius ratio 1.7, a quarter of the circle had the largest critical flow angle for the narrowest diffusers, and the linear pinch shape was the best for the widest diffusers. For the radius ratio 1.3, the linear pinch shape had the largest critical flow angle for the narrower diffusers, and the elliptical arc had the largest critical flow angle for the wider diffusers. The pinch shape had no signifcant effect on stage performance. Reducing the diffuser width led to a higher pressure drop, and it led to lower stage efficiencies, as compared to a diffuser whose width was $b_{2'}/b_2 = 0.60$. Tang (2006) has conducted computational analysis for small centrifugal compressors. The added pinch was about the same height as the usual tip clearance for similar industrial compressors. Five different vaneless diffuser inlet geometries were studied: no pinch, and pinches with a straight

corner, a concave circle, a straight line, and a protruding circle as the pinch inlet shape. Three different mass flows were used: the design mass flow, 110% of the design flow, and 85% of the design flow. Adding pinch had only a very minor effect on compressor efficiency, all different configurations had efficiencies within 0.5 percentage points from each other. Adding pinch increased the total-to-total pressure ratio, about 0.5 for the low mass flow, slightly less for the design flow and even less for the high mass flow. The pinch shape had little effect, the concave circle and straight line being somewhat better than the rest.

Two parallel wall diffusers with different widths have been tested by Di Liberti et al. (1996). The diffusers had constant widths of 9.40 mm and 11.18 mm. The experiments were carried out at three different speed lines. The narrower of the two diffusers had better efficiency and total-to-total pressure ratio, except at low speed, where an almost identical total-to-total pressure ratio was obtained. The authors also noted that the diffuser width did not influence the overall performance of the impeller. Lee et al. (2001) have developed a direct method for optimizing the vaneless diffuser. They optimized an original vaneless diffuser which had a flat hub and curved (tapered) shroud. The optimized geometry still had a flat plate as a hub, because the transmission and motor were located at the hub side, so the hub wall was not optimized. The shroud was first convergent but the angle changed, then at radius ratio r/r_2 of approximately 1.35 the diffuser reached its minimum width, which was approximately half of the inlet width. After that the diffuser was divergent, and then again it changed to convergent when the radius ratio r/r_2 was approximately 1.55. The optimized geomery was also simulated with CFD and it was measured. The theoretically predicted optimum diffuser shape was found to be superior to the original diffuser shape.

Different pinch configurations for a high speed centrifugal compressor have been tested in a series of CFD calculations and experimental work (Turunen-Saaresti, 2004; Turunen-Saaresti et al., 2006). Computational analysis was performed for the following geometries: unpinched, 5%, and 10% pinches from the impeller exit width. The pinches were implemented at the hub wall, at the shroud wall or at both walls divided evenly. The unpinched geometry and 10% pinch divided at both walls were modeled with three different mass flows: the design flow, 1.4 times the design flow, and 0.6 times the design flow. These two geometries were also tested experimentally with the same mass flows. The numerical simulation results showed that in terms of efficiency, the best performance for the compressor was achieved with the pinch of 10% divided at both walls. The numerical results also indicated that

a pinch made to the hub wall was more beneficial than a pinch made to the shroud wall. The numerical results also showed that the pinch decreased the static pressure variations caused by the blade wakes and the higher pressure from the pressure side of the blades. The differences of different pinches were minor. The pinch also decreased the sizes of the slow velocity flow areas near the diffuser walls. The measured results showed that the pinch expandes the area of good efficiency, and it was most beneficial at high volume flow and at lower speeds. The greatest increment of efficiency was 2 percentage points when compared to the unpinched geometry.

Pinarbasi and Johnson (1994a) have carried out constant-temperature hot-wire anemometer measurements at design mass flow in the diffuser of a low-speed centrifugal compressor whose impeller had 30° backswept blading. The flow field at diffuser entry showed a jet-wake flow pattern and blade wakes. The measured results showed that the blade wake mixed out rapidly, but the passage wake mixed out slowly and the passage vortex was carried over to the diffuser. Also the variations in circumferential direction mixed out, but the variations in the axial direction tended to persist so that the flow eventually resembled a Couette flow between the diffuser walls. The authors have done similar tests with the same compressor also with mass flows of 16% below and 11% above the design mass flow (Pinarbasi and Johnson, 1995b). As at the design flow, also at the off-design flow the blade wake mixed out more rapidly than the passage wake. At the high flow rate the shear gradients from the blade and passage wakes and the secondary flows were much stronger. The stronger secondary flows at the high flow rate prevented the circumferential variations from mixing out rapidly. Stress tensor measurements (Pinarbasi and Johnson, 1996) showed that the turbulent kinetic energy levels and strong Reynolds stresses caused rapid mixing of blade wakes. The passage wake had similar turbulent kinetic energy levels, but the Reynolds stresses were much weaker and hence the passage wake mixed out slowly. The same applied also to off-design conditions (Pinarbasi and Johnson, 1994b).

Two vaneless diffusers with different width ($b_{2'}/b_2 = 0.7$ and 0.83) have been tested by Engeda (2001). The impeller had a back sweep of 19.3°. Rotating stall, presumed to be progressive impeller stall was found out with both vaneless diffuser configurations. The rotating cells ran opposite to the impeller and their relative speed was found to be constant, irrespective of impeller speed. Deep surges of vaneless configurations were triggered by the diffuser stall. With the same impeller, diffusers with widths $b_{2'}/d_{2'}$ of 0.0354 and 0.0417 were tested (Engeda, 2002). It was found out that increasing

the diffuser width shifted the onset of rotating stall to lower flow rates, and the frequensies of the rotating cells decreased. On the stall behavior and evolution from the same experimental setup mentioned above (Ferrara et al., 2002a,b), it was also concluded that the pinch shape and the diffuser width have a very small influence on the stall behaviour and evolution (Ferrara et al., 2004).

2.2 Vaned diffuser

Vaned diffusers can be divided into different categories for instance by solidity (conventional vaned diffuser (CVD), low-solidity (LSVD)), or by vane type (circular arc or flat plane). Examples of different vaned diffusers are presented in Fig.2.3. The solidity σ is defined as

$$\sigma = \frac{c}{s} \tag{2.4}$$

where c is the chord length and s is the distance between two diffuser vanes at the leading edge. A diffuser is considered to be a low solidity one when there is no throat in the cascade.

A conventional vaned diffuser, thin flat plate LSVDs and a vaneless diffuser performance have been tested for both a low Mach number process gas compressor using nitrogen and a high Mach nuber compressor using air (Hohlweg et al., 1993). For the high Mach number air compressor, it was found out that the CVD achieved at least 2.6% higher efficiency at design flow than the best LSVD. The LSVD with the largest negative incidence (-4.1 °) had the best overall performance. Its flow range was 30% higher than that of the CVD, and the efficiency was 4.9% higher than the efficiency of the vaneless configuration. Of the three tested LSVDs the one with highest absolute incidence (+0.3 °) had efficiency and stability significantly lower than the CVD. From this the authors note that positive incidences should be avoided when designing LSVDs. Also the incidence angle had a direct effect on both the operating range and efficiency, so it shoud be possible to find an optimum angle which has the best efficiency and range combination. For the low Mach number nitrogen compressor, Hohlweg et al. tested only one LSVD, and it had essentially the same design point efficiency as the CVD. Also the LSVD had a significantly smaller stability range than the CVD, and the incidence angle seemed not to be the controlling parameter. The authors note that the vane number of the LSVD might have been too low, so that it allowed large

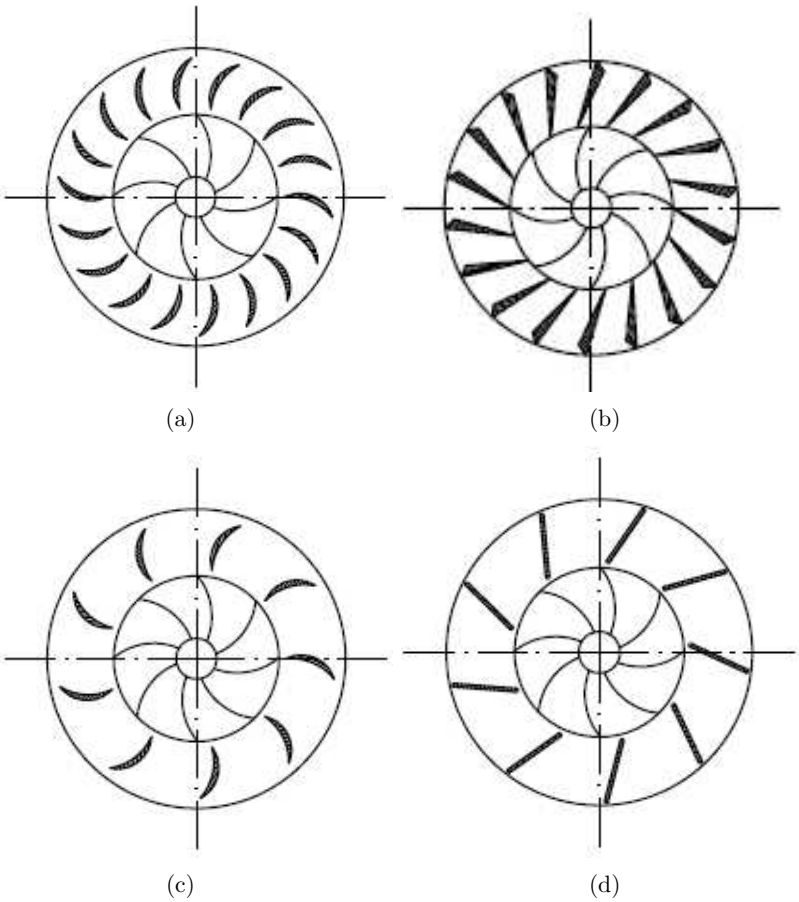

Figure 2.3: Different types of vaned diffusers: (a) cascade diffuser, (b) channel diffuser, (c) LSVD, and (d) LSVD with flat plate vanes.

stall cells to appear at lower mass flows.

A CFD study has been performed for five different low solidity vaned diffusers coupled with a high speed centrifugal impeller by Turunen-Saaresti (2004). Three different diffusers with a circular arc camberline were used. The diffusers had seven, nine and 11 vanes with NACA thickness distribution. All of those LSVDs had the design incidence angle of -2°, and the vane

turning angle was 10°. In addition, a diffuser with nine flat plate vanes, and a diffuser with nine flat plate vanes with a circular arc camber line were simulated. Also the latter two diffusers had the design incidence angle of -2°. All geometries were simulated with design mass flow, except the one with 9 vanes and NACA profile, which was also simulated with low and high mass flows. According to the numerical results, the LSVDs with the circular arc camberline and NACA thickness distribution had the highest isentropic efficiencies. A greater vane number led to a better performance of the diffuser, and the diffusers with a NACA profile were better than the ones with the constant thickness profile. In the research of Turunen-Saaresti (2004), the nine vaned LSVD with NACA thickness distribution were also investigated experimentally. Static pressure measurements and performance map measurements were performed. The LSVD had higher efficiency but slightly narrower operating range, when compared to a vaneless diffuser. The LSVDs achieved a good perfomance over a wide range of incidence angles, only very large negative or positive incidences deteriorated the efficiency. The LSVDs decreased also circumferential pressure non-uniformity at the low flow. The total pressure losses were higher with LSVD when operating at low or high flows, compared to the vaneless diffuser. The static pressure rise in the LSVD was higher at low flow. The more radial flow leaving the LSVD led to an increase in losses and decrease in pressure rise at the volute collector, especially at high and design flows.

Vaned diffusers in a high-speed centrifugal compressor stage for turbocharger applications have been investigated numerically by He and Tourlidakis (2001). Three of the CVDs had 11, 12 and 33 vanes with a vane leading edge radius ratio $r_{2'}/r_2$ of 1.07. The fourth diffuser had 22 vanes, and the vane leading edge radius ratio was 1.15. It was found out that when the number of vanes increased, the operating range became narrower. The peak efficiency changed when the vane number was changed, but there was no trend in whether it increased or decreased with respect to the vane number. When the vane number decreased, the pressure recovery coefficient increased. This applied only at the surge flow when the mass flow was kept at the same rate for different diffusers. The flow through the vaneless and semi-vaneless space became more uniform with fewer diffuser wanes. This was due to lower adverse pressure gradients in that area. As the area ratio increased, the surge flow increased. However, area ratio is not the dominant factor to influence the flow range, because the stage with fewer diffuser vanes can have a wider flow range, even if it has the same area ratio as a diffuser with more vanes.

In a series of experimental and numerical studies of two vaneless diffusers,

a conventional vaned diffuser and eight different low solidity vaneles diffusers have been investigated by Kim and Engeda (1997) and Engeda (1998, 2003).The CVD had better peak efficiency than the LSVDs or the vaneless diffusers, but it also had the narrowest operating range. LSVDs had better efficiency over a wide flow range than the vaneless diffusers, and the peak efficiency was attained at higher mass flow than with the CVD. Thus the LSVDs provided a greater stable operating margin. Concerning the LSVDs, it was found out that solidity is the major parameter affecting the LSVDs, along with the vane turning angle. When solidity decreases, the flow range becomes wider, and when solidity increases, the pressure recovery in the diffuser and the efficiency increase. The number of vanes in the LSVDs varyied from 14 to 18, and the authors conclude that it had a marginal effect on the overall performance. Kim et al. (2002) have performed an experimental and numerical study of two different types of conventional diffusers, flat plate cambered and airfoil cambered, and of a low solidity vaneless diffuser with flat plate straight vanes. The flat plate cambered diffuser had the highest peak efficiency, but it also had the narrowest flow range. The LSVD had the widest operating range and reasonably good efficiency when compared to the CVDs. The results also indicated that the surge limit is controlled by the diffuser for the CVDs and the impeller for the LSVD case. Similar results have been achieved also for a low specific speed centrifugal compressor (Issac et al., 2003): the vaneless diffuser had the widest operating range, the CVD had the highest peak efficiency, but it occured near the surge line, and the operating range was narrow. The LSVD fell in between the vaneless and the CVD in terms of efficiency and operating range.

The effect of diffuser vane height and placement have been studied for the above mentioned low specific speed compressor by Issac et al. (2004). The vane height varied from 0.2...0.9 times the diffuser width. Partial vanes with height of 0.2...0.3 were found to be beneficial in terms of flow coefficient and operating range when compared to the CVD and the LSVD. The efficiency of the partially vaned diffuser (PVD) was higher when compared to both the CVD and the vaneless diffusers. The best efficiency was achieved when the vane height was 0.4 times the diffuser width. Whether the partial vanes were positioned to the hub or to the shroud was found to have little or no effect. However, when the partial vanes were fixed to both the hub and the shroud in staggered spacing, the compressor performance improved substantially. In an another experimental study by Yoshinaga et al. (1987), where 18 different kind of partial vanes fixed to the shroud were investigated. The authors conclude that the optimum height in terms of pressure recovery was little less than half of the diffuser width, and also that the partial vanes provided

a uniform flow in the axial direction. Liu and Xu (2004) have carried out a numerical study of a high speed centrifugal compressor with PVD, and conclude that the optimum height for partial vanes was 0.4 times the diffuser width for hub vanes and 0.3 for shroud vanes, in terms of efficiency and static pressure recovery. The shroud vanes seemed to be slighly better than the hub vanes, and both were better than the vaneless diffuser.

To determine the influence of the diffuser leading edge radius ratio, pressure surcface setting angle and semi-vaneless space suction surface profile, a total of 45 channel diffusers have been studied experimentally, using two different turbocharger compressors (Clements and Artt, 1989). The pressure face angle had virtually no effect on the compressor performance over the useful operating range, provided that the suction surface profile remained unchanged. Straight wedge diffusers produced higher stage efficiencies than diffusers with a concave profile on the suction surface between the leading edge and the throat. Surge line position was almost unaffected by the changes in diffuser geometry. Optimum stage performance was achieved when the diffuser leading edge radius ratio was between 1.06 and 1.10. A CFD study using unsteady three-dimensional Reynolds-averaged Navier-Stokes simulation to define the effect of impeller-diffuser interaction on the performance of a centrifugal compressor stage has been carried out by Shum et al. (2000). Three different diffuser geometries were modeled (vaneless, and diffuser vane leading edge ratios of 1.092 and 1.054) with the same impeller. It was found that the alignment of diffuser vanes with a spatially averaged and time-averaged impeller exit flow angle is the main parameter affecting diffuser performance, so reasonably accurate prediction of diffuser performance is achievable with only using quasi-steady calculation. There is an optimum radial gap between the diffuser vanes and impeller exit, because at some decreasing radius, increasing losses overtake the benefits of smaller blockage.

To prevent stall inception in a high pressure centrifugal compressor, Cellai et al. (2003a) tested five different low solidity vaned diffusers. All diffusers had a solidity of 0.7, and the the vanes had a circular arc camber line. The number of vanes varied from 4 to 14, three different vane leading edge radius ratios were used: 1.04, 1.10 and 1.14, and also three different outlet radius ratios were used: 1.25, 1.30 and 1.35. The chord length influenced the choke mass flow, the higher the chord length was, the lower maximum flow rate was achieved. The surge mass flow was lowest when the outlet radius was highest. The stall inception mass flow was influenced by the chord length and the outlet radius. Increase in the outlet radius led to lower surge mass flows.

A channel diffuser with 16 wedge vanes coupled with a low speed backswept impeller have been investigated experimentally, using hot wire anemometry, both with design operating mass flow (Pinarbasi and Johnson, 1995a) and at off design mass flows (Pinarbasi and Johnson, 1997). The diffuser vane leading edge radius ratio was 1.1. At design speed, the impeller blade wakes mixed out rapidly within the vaneless space between the impeller exit and diffuser vanes. The mixing out was more rapid than in an equivalent vaneless diffuser. Also the flow velocities increased in the mid vane position and decreased close to the vanes. The circumferential variations in the velocity mixed out rapidly in the near vane position. Some variations existed still at the mid vane position well into the diffuser. Also at the off-design conditions the blade wakes mixed out rapidly, and it took approximately half the radial distance in the vaned diffuser when compared with a vaneless diffuser. The vane-to-vane pressure gradient decayed rapidly when operating at flows below the design flow, and it persisted throughout the diffuser when operating at flows above the design flow.

Laser Doppler Velocimetry measurements have been done for a single stage high subsonic centrifugal compressor with a vaned diffuser with 24 circular-arc vanes (Stahlecker and Gyarmathy, 1998). The diffuser vane leading edge radius ratio was 1.16, and the compressor was operated at a rotational speed where the incidence was zero. The above mentioned rapid jet-wake mixing-out was observed also in this research. The time-averaged streamwise velocity profiles from hub to tip along the diffuser stream path revealed that significant diffusion occured only at the hub side. The flow deficiency near the shroud, yielding from the impeller, decayed before the diffuser throat because of the high Reynolds stresses transmitting energy from the hub to the shroud. In other words, the flow uniformalization between the impeller exit and diffuser throat (accelerating flow near the shroud and decelerating near the hub) was due to turbulent shear work. If the turbulent and deterministic (caused by the impeller jet-wake flow structure) fluctuations were separated, the deterministic fluctuation intensity damped out quickly along the stream path, in planes parallel to the diffuser walls, the turbulent fluctuation intensity decreased gradially at the shroud and increased at the hub. Finally the axial turbulent fluctuations were generally quite low when compared to wall parallel fluctuations.

Justen et al. (1999) studied a highly loaded centrifugal compressor impeller with 23 vaned wedge diffusers experimentally. In a series of experiments, unsteady pressure measurements were performed at three different operating

speeds: 0.6, 0.7 and 0.8 times the design operating speed. Two different radial gaps between the impeller exit and vane leading edge were tested: 1.06 and 1.10. Also two different vane setting angles were used: 14.5 and 16.5 ° (from tangential direction). The pressure fluctuations revealed that the semi-vaneless space, especially closer to the vane suction side, was influenced by unsteady impeller-diffuser interactions, and this unsteadiness did not decay even with a larger radial gap. At the choke limit, the diffuser throat acted as a convergent/divergent nozzle, resulting in a separated region on the vane pressure side. Operating points near the choke limit were determined by supersonic flow and shocks in the diffuser channel, even though the diffuser inlet flow was subsonic. At flows below the stable operating range, the beginning reverse flow was characterized by a slight pressure drop at the diffuser exit, while the impeller inlet and exit along with diffuser throat showed a positive pressure rise. Simultaneously, the whole rotor moved abruptly towards the shroud. Severe pressure oscillations occured at the impeller exit and at the diffuser throat as long as reverse flow occured. These oscillations eventually dampened shortly before the pressure minimum was reached.

For the above mentioned stage, also steady pressure and laser-2-focus velocimeter measurements have been performed (Ziegler et al., 2003a,b). Steady probe measurements were performed at the speed of 0.8 times the design speed. For a diffuser with a vane setting angle of 16.5° (from tangential direction), the radial gap between the impeller exit and vane leading edge was varied from 1.04 to 1.18, and for a diffuser whose vane setting angle was 12.5° (from tangential direction), the leading edge radius ratio was varied from 1.06 to 1.18. Probe measurements were also performed for a vaneless diffuser for purposes of comparison. Laser measuremets were also performed for the above mentioned geometries at the same speed. In addition to probe and laser measurements, the compressor map was also measured. The compressor map showed a rising total pressure ratio and efficiency with the reducing radial gap. The impeller showed slightly higher work input for smaller radial gaps, while the impeller efficiency hardly changed. The flow field at the diffuser exit seemed to be more uniform at smaller radial gaps. According to the authors, the reason for this was that the reducing radial gap led to an unloading of the diffuser vane pressure side, which is usually highly loaded. Due to lower Mach numbers at diffuser exit at smaller radial gaps, the total pressure loss in the collector was smaller. Also the slip at the impeller exit was not effected by the diffuser. In general, small radial gaps were recommended, if a wide operating range was not the priority.

3 Numerical procedure

Different diffuser geometries were investigated numerically. The quasi-stedy approach was used. The inlet cone, impeller and diffuser were modeled. The volute was not modeled. In the cases where the vaneless diffuser was analyzed, only one impeller passage (full blade to full blade) and the corresponding section of the vaneless diffuser and the inlet cone were modeled. When vaned diffusers were investigated, the whole impeller, diffuser and inlet cone were modeled. The ideal gas equation of state was used to solve the properties of the working fluid (dry air).

The numerical calculations were made with the Finflo flow solver, which is a Navier-Stokes solver developed at Helsinki University of Technology (TKK). Finflo uses the finite-volume technique for spatial dicretization, Roe's flux-difference splitting for the inviscid fluxes, and thin layer approximation to evaluate the viscous fluxes. For the primary flow variables and conservative turbulent variables, the MUSCL approach is used. The discretized equations are integrated in time by using the DDADI-factorization. More details and the governing equations can be found for example in the user's guide (Siikonen et al., 2004) or cases where Finflo has been used (Rautaheimo et al., 1999; Turunen-Saaresti, 2004; Tang, 2006).

3.1 Turbulence modeling

Direct numerical solution (DNS) and large eddy simulations (LES), which are able to model the turbulence more accurately, are impractical to use in most engineering problems because of the time they consume, even with todays computing resources. The same applies to the Reynold stress models (RSM). The two-equation turbulence models that are based on the Boussinesq approximation are still widely used. In recent years more emphasis have been given to explicit algebraic Reynolds stress models (EARSM), in which part of the process on the RSM-level is trasferred onto the two-equation modelling level. The more advanced numerical methods (DNS, LES, RSM and EARSM), should give more accurate results, especially about details in flow fields, but most of them still require more research and development.

Two recent dissertations made in the Laboratory of Fluid Dynamics at LUT consider CFD in centrifugal compressors (Turunen-Saaresti, 2004; Tang, 2006). The Finflo flow solver has been used also in these dissertations. Both authors conclude on the basis of their literature survey and available com-

putational resources that Chien's $k-\epsilon$ turbulence model (Chien, 1982) was the most suitable for their purposes. On the basis of this and laboratory practice, Chien's $k-\epsilon$ model is used also in this thesis. In addition, some calculations have been made using Menter's shear-stress transport $k-\omega$-SST turbulence model (Menter, 1992), which is derived from the original $k-\omega$ model by Wilcox (1988). Both turbulence models, Chien's $k-\epsilon$ and the $k-\omega$-SST are implemented in the Finflo solver.

3.1.1 Chien's $k-\epsilon$ turbulence model

Chien's $k-\epsilon$ turbulence model is a low Reynolds number turbulence model. The general approach of Chien's $k-\epsilon$ model is the same as that of Jones and Launder (Jones and Launder, 1972). In low Reynolds number turbulence models, the wall functions are not used, and the boundary layer is calculated using empirical functions, if the grid density is sufficient. The grid size should be dense near the walls, meaning that y^+ should be close to unity. y^+ is defined as

$$y^+ = y_\mathrm{n}\frac{\rho u_\mathrm{T}}{\mu_\mathrm{w}} = y_\mathrm{n}\frac{\sqrt{\rho\tau_\mathrm{w}}}{\mu_\mathrm{w}} \tag{3.1}$$

where y_n is the normal distance from the wall, u_T is the friction velocity, μ_w is the molecular viscosity on the wall, and τ_w is the shear stress on the wall.

In Chien's $k-\epsilon$ turbulence model, the dynamic eddy viscosity μ_T is

$$\mu_\mathrm{T} = \frac{C_\mu f_\mu \rho k^2}{\tilde{\epsilon}} \tag{3.2}$$

where C_μ is a closure coefficient, f_μ is an empirical function, k is the turbulent kinetic energy, and $\tilde{\epsilon}$ is

$$\tilde{\epsilon} = \epsilon - \epsilon_0 \tag{3.3}$$

where ϵ is the dissipation of turbulent kinetic energy. ϵ_0 is the value of ϵ at the wall ($y=0$). The kinetic energy of turbulence k is

$$\frac{\partial(\rho k)}{\partial t} + \frac{\partial(\rho u_\mathrm{j} k)}{\partial x_\mathrm{j}} = \tau_\mathrm{ij}\frac{\partial(\rho u_\mathrm{i})}{\partial x_\mathrm{j}} - \rho\epsilon + \frac{\partial}{\partial x_\mathrm{j}}\left[\left(\mu + \frac{\mu_\mathrm{T}}{\sigma_\mathrm{k}}\right)\frac{\partial k}{\partial x_\mathrm{j}}\right] \tag{3.4}$$

where the u is the mean velocity in specific co-ordinate direction, x is the position vector in a given co-ordinate direction, σ_k is a closure coefficient and subscripts i and j are tensor notations. The dissipation rate is

$$\frac{\partial(\rho\tilde{\epsilon})}{\partial t}+\frac{\partial(\rho u_{\mathrm{j}}\tilde{\epsilon})}{\partial x_{\mathrm{j}}}=C_1 f_1\frac{\tilde{\epsilon}}{k}\tau_{\mathrm{ij}}\frac{\partial(\rho u_{\mathrm{i}})}{\partial x_{\mathrm{j}}}-C_2 f_2\frac{\tilde{\epsilon}^2}{k}+E+\frac{\partial}{\partial x_{\mathrm{j}}}\left[\left(\mu+\frac{\mu_{\mathrm{T}}}{\sigma_\epsilon}\right)\frac{\partial\tilde{\epsilon}}{\partial x_{\mathrm{j}}}\right] \quad (3.5)$$

where C_1, C_2 and σ_ϵ are closure coefficients, and f_1, f_2, f_μ, ϵ_0 and E are empirical functions. The closure coefficients and the empirical functions are given in table 3.1. The turbulent Reynolds number $\mathrm{Re_T}$ is defined as

$$\mathrm{Re_T}=\frac{\rho k}{\tilde{\epsilon}\mu_{\mathrm{T}}} \quad (3.6)$$

Table 3.1: Closure coefficients and empirical functions in Chien's $k-\epsilon$ turbulence model

$C_1 = 1.35$	$f_1 = 1$
$C_2 = 1.80$	$f_2 = 1 - 0.22e^{\frac{-Re_{\mathrm{T}}^2}{36}}$
$C_\mu = 0.09$	$f_\mu = 1 - e^{-0.0115y^+}$
$\sigma_{\mathrm{k}} = 1.00$	$\epsilon_0 = 2\mu\frac{\rho k}{y^2}$
$\sigma_\epsilon = 1.30$	$E = -2\mu\frac{\rho\tilde{\epsilon}}{y^2}e^{\frac{-y^+}{2}}$

Finflo uses 1.44 for C_1 and 1.92 for C_2, which are based on the most commonly used coefficients (Siikonen et al., 2004).

3.1.2 $k-\omega$-SST turbulence model

Menter's $k-\omega$-SST turbulence model is based on the so called baseline model (BSL) by the same author (Menter, 1992), which is modified from the $k-\omega$ model of Wilcox (Wilcox, 1988).

In the BSL model, the turbulent kinetic energy is

$$\frac{\partial(\rho k)}{\partial t}+\frac{\partial(\rho u_{\mathrm{j}}k)}{\partial x_{\mathrm{j}}}=P_{\mathrm{k}}-\beta^*\rho\omega k+\frac{\partial}{\partial x_{\mathrm{j}}}\left[(\mu+\sigma_{\mathrm{k}}\mu_{\mathrm{t}})\frac{\partial k}{\partial x_{\mathrm{j}}}\right] \quad (3.7)$$

and the specific dissipation rate is

$$\begin{aligned}\frac{\partial(\rho\omega)}{\partial t}+\frac{\partial(\rho u_{\mathrm{j}}\omega)}{\partial x_{\mathrm{j}}} &= \gamma P_\omega-\beta\rho\omega^2+2(1-F_1)\sigma_\omega 2\frac{\mu_{\mathrm{t}}}{k}\frac{\partial k}{\partial x_{\mathrm{j}}}\frac{\partial\omega}{\partial x_{\mathrm{j}}}\\ &+ \frac{\partial}{\partial x_{\mathrm{j}}}\left[(\mu+\sigma_\omega\mu_{\mathrm{t}})\frac{\partial\omega}{\partial x_{\mathrm{j}}}\right] \quad (3.8)\end{aligned}$$

where ω is the specific dissipation rate and β^*, γ, σ_k and σ_ω are closure coefficients. The production terms in equations 3.7 and 3.8 P_k and P_ω are defined as follows

$$P_\mathrm{k} = \mu_\mathrm{t} \frac{\partial u_\mathrm{i}}{\partial x_\mathrm{j}} \left(\frac{\partial u_\mathrm{i}}{\partial x_\mathrm{j}} + \frac{\partial u_\mathrm{j}}{\partial x_\mathrm{i}} \right) - \frac{2}{3} \rho k \delta_\mathrm{ij} \frac{\partial u_\mathrm{i}}{\partial x_\mathrm{j}} \tag{3.9}$$

$$P_\omega = \rho \frac{\partial u_\mathrm{i}}{\partial x_\mathrm{j}} \left(\frac{\partial u_\mathrm{i}}{\partial x_\mathrm{j}} + \frac{\partial u_\mathrm{j}}{\partial x_\mathrm{i}} \right) - \frac{2}{3} \rho \omega \delta_\mathrm{ij} \frac{\partial u_\mathrm{i}}{\partial x_\mathrm{j}} \tag{3.10}$$

A given closure coefficient ϕ in equation 3.7 or 3.8 is calculated from

$$\phi = F_1 \phi_1 + (1 - F_1) \phi_2 \tag{3.11}$$

where ϕ denotes a specific closure coefficient (σ_k, σ_ω, etc.). The function F_1 is

$$F_1 = \tanh(A_1^4) \tag{3.12}$$

$$A_1 = \max \left[\min \left(\frac{\sqrt{k}}{0.09 \omega y}; 0.45 \frac{\omega}{\Omega} \right); \frac{400\nu}{y^2 \omega} \right] \tag{3.13}$$

where y is the distance to the next surface, and Ω is the absolute value of vorticity. The kinematic eddy viscosity is defined as

$$\nu_\mathrm{T} = \frac{k}{\omega} \tag{3.14}$$

The actual SST model starts from the idea that unlike eddy-viscosity models, the full Reynolds-stress models account for transport of the principal turbulent shear stress by inclusion of the term

$$\frac{D\tau}{Dt} \equiv \frac{\partial \tau}{\partial t} + u_\mathrm{k} \frac{\partial \tau}{\partial x_\mathrm{k}} \tag{3.15}$$

The shear stress in a boundary layer is assumed to be proportional to the turbulent kinetic energy

$$\tau = \rho a_1 k \tag{3.16}$$

where the constant $a_1 = 0.03$ (Finflo uses $a_1 = 0.031$). On the other hand, the definition of the shear stress is

$$\tau = \mu \frac{\partial u}{\partial y} \tag{3.17}$$

For conventional two-equation models, the shear stress relation can be rewritten to give

$$\tau = \rho\sqrt{\frac{\text{Production}_\text{k}}{\text{Dissipation}_\text{k}}}a_1 k \tag{3.18}$$

For adverse pressure gradients, the ratio of production versus dissipation of turbulent kinetic energy might be significantly larger than one. This leads to over-prediction of turbulent kinetic energy with equation 3.18. In order to satisfy equation 3.16, the eddy viscosity is redefined as

$$\nu_\text{T} = \frac{a_1 k}{\frac{\partial u}{\partial y}} \tag{3.19}$$

Equation 3.19 stipulates that the shear stress does not change more rapidly than $\rho a_1 k$. However, it leads to infinitely high eddy-viscosities when $\partial u/\partial y$ reaches zero. In adverse pressure gradients, the production is larger than dissipation for the largest part of the boundary-layer ($\partial u/\partial y > a_1\omega$). Expression

$$\nu_\text{T} = \frac{a_1 k}{\max\left(a_1\omega; \frac{\partial u}{\partial y}\right)} \tag{3.20}$$

dictates that equation 3.19 is used for most of the adverse pressure gradient regions, such as the wake region of the boundary layer, whereas equation 3.14 is used for the rest of the boundary layer.

The above-mentioned modification to the SST model is limited only to boundary layer flows. This is done in the same way as in the BSL model, by applying a blending function F_2. Now the eddy viscosity becomes

$$\nu_\text{T} = \frac{a_1 k}{\max\left(a_1\omega; \frac{\partial u}{\partial y}F_2\right)} \tag{3.21}$$

where the blending function is

$$F_2 = \tanh(A_2^2) \tag{3.22}$$

$$A_2 = \max\left(2\frac{\sqrt{k}}{0.09\omega k}; \frac{400\nu}{y^2\omega}\right) \tag{3.23}$$

The other parameter in Eq.3.23 has a constant 400 in the numerator. Finflo uses the value 500 instead of 400. The closure coefficients to be used in equations 3.7 and 3.8 are obtained by using equation 3.11 with the coefficients presented in Table 3.2 (set 1 for near wall region and set 2 for free shear layers). For $\sigma_{\omega 1}$ in the first set, Finflo uses 0.5 instead of 0.65. The changes made by the programmers to Finflo, considering the correlations, are based on the work by Hellsten and Laine (1997); Hellsten (1998, 2004).

Table 3.2: Coefficients for equation 3.11.

Set 1	Set 2
$\sigma_{\mathrm{k}1} = 0.85$	$\sigma_{\mathrm{k}2} = 1.00$
$\sigma_{\omega 1} = 0.65$	$\sigma_{\omega 2} = 0.856$
$\beta_1 = 0.0750$	$\beta_2 = 0.0828$
$\beta^* = 0.09$	$\beta^* = 0.09$
$\kappa = 0.41$	$\kappa = 0.41$
$\gamma_1 = \frac{\beta_1}{\beta^*} - \frac{\sigma_{\omega 1}\kappa^2}{\sqrt{\beta^*}}$	$\gamma_2 = \frac{\beta_2}{\beta^*} - \frac{\sigma_{\omega 2}\kappa^2}{\sqrt{\beta^*}}$

3.2 Boundary conditions

The inlet boundary conditions were given in the beginning of the inlet cone. The total entalphy and the momentum distributions were given, whereas the static pressure distribution was extrapolated from the computational domain. Also the turbulence intensity and the non-dimensional turbulent viscosity μ_{T}/μ were defined at the inlet boundary. The flow was assumed to be fully axial, and constant distributions were applied. However, the momentum and turbulence quantities were given time to develop in the inlet cone before the flow reached the impeller.

Outlet boundary conditions were defined at the diffuser exit at a radius ratio of $r/r_2 = 1.68$. At the outlet boundary, a constant static pressure distribution was given and the velocity gradients were zero. The assumption of constant pressure distribution at the diffuser exit is only valid at design operating conditions. At off-design conditions the volute causes circumferential pressure distortions at the diffuser. The outlet boundary conditions used here did not take into account the circumferential pressure distortions at off-design conditions. When using these boundary conditions, it is not neccessary to

model the volute, but it causes inaccuracy if off-design calculations are to be performed.

In the cases of vaneless diffusers where only one passage was modeled, cyclic periodical boundary conditions were used at the side faces of the vaneless diffuser and inlet cone. The same boundary condition was applied also to the side faces of full blade tip clearance blocks to ensure periodicity there.

When the vaned diffusers were modeled, mixing plane boundary condition was used between the impeller exit and diffuser inlet. This boundary condition averages the flow quantities in the circumferential direction. Mixing plane boundary condition was used in order to avoid time accurate simulations.

4 Numerical results

During the course of the research and the literature survey, the focus was on the effect of the pinch and conventional vaned diffuser to the performance of an existing centrifugal compressor stage, originally designed with a vaneless unpinched diffuser.

It seems that it is possible to improve the performance of an existing centrifugal compressor stage by adding a pinch, but it remains unclear how much pinch should be added and where the pinch would be most beneficial. In order to find an answer to this, five different vaneless geometries were investigated numerically, one without a pinch and four with different pinches.

Considering CVDs, it is clear that it is possible to improve the efficiency of the existing centrifugal compressor stage. The main interest was to find out how the number of vanes or the vane turning angle affects the overall performance of the said stage. Six different CVD geometries with different number of vanes and vane turning angles were investigated numerically.

A coarse grid sensitity study was performed. This was done by computing the vaneless unpinched geometry with three different grids having a different number of cells. In addition, the results of the previous grid levels (2nd and 3rd) for the least dense grid were also investigated.

In order to have more certainty in the CFD-process, a code validation case was also modeled. A NASA low-speed centrifugal compressor whose geometry data and measurement results are well documented (Hathaway et al., 1995) was chosen to be the case. The results of the Finflo calculations were compared to these measurement results.

All diffuser simulations in this study were modeled with the same inlet cone and impeller. The impeller was unshrouded, with seven full and seven splitter blades. The blade backsweep at the impeller exit was 40° from the radial direction. The stage design total-to-total pressure ratio $\pi_{\mathrm{t-t}}$ was 1.78, and the specific rotational speed was 0.8. The compressor has been originally designed to be used in waste water treatment plants. Tip clearance was modeled for every case.

4.1 NASA low-speed compressor

To have more certainty in the CFD-results, a NASA low-speed compressor was modeled. There are extensive laser anemometer measurements of the same geometry (Hathaway et al., 1995). The surface grid that was used to compute the compressor is shown in Fig. 4.1. The case was calculated with both the $k - \epsilon$ and the $k - \omega$-SST turbulence models.

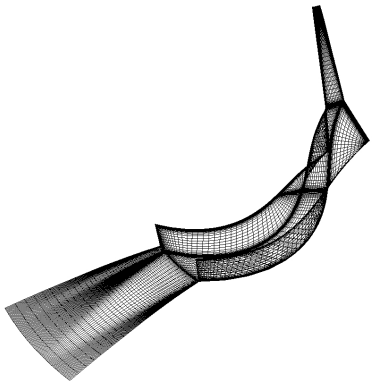

Figure 4.1: NASA low-speed compressor surface grid (inlet cone and diffuser shroud not shown)

The radial and tangential velocities normalized with the impeller exit circumferential speed in both the measurements and the CFD at the impeller inlet and outlet are presented in Fig. 4.2 and Fig. 4.3, respectively. The CFD results at the impeller inlet correlate quite well with the measured ones (Fig. 4.2). Both the radial and tangential velocities match the measured velocities extremely well in the middle of the channel (in circumferential direction). The greatest differences are nearer to the hub suction surface. In all cases, the tangential velocity near the suction surface is greater with the CFD than what the measurements suggest. There are no significant differences between the two turbulence models.

The velocities in the CFD results at the impeller exit (Fig. 4.3) also correlate quite well with the measured ones. The best accuracy is achieved near the hub, where the CFD predicts marginally higher velocities than what the measured velocities are. In the mid channel (between the hub and the shroud), the CFD results suggest slightly slower radial velocity. The $k - \omega$-SST turbulence model predicts a slightly slower tangential velocity, and the

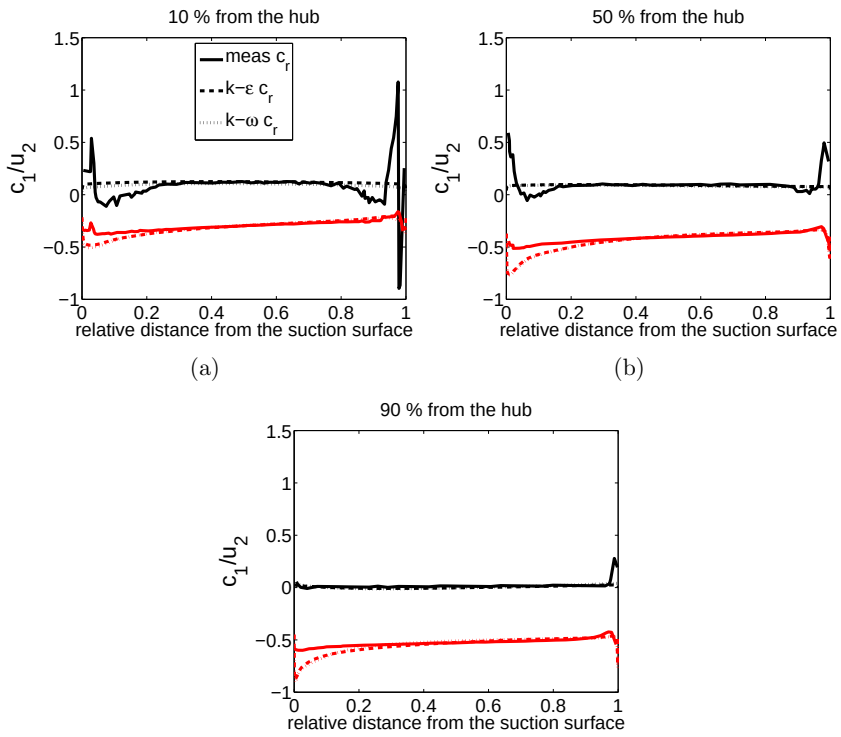

Figure 4.2: Calculation and measurement results at the impeller inlet: (a) 10% from the hub, (b) 50% from the hub, and (c) 90% from the hub. Radial velocity in black and tangential in red. Measurements by Hathaway et al. (1995).

$k - \epsilon$ turbulence model predicts somewhat higher tangential velocity. Most differences are near the shroud, where the calculated velocites are smaller than the measured ones. Also, the velocity profile is quite similar. At the impeller exit, the differences between the two turbulence models are minor except, near the shroud, where the $k - \epsilon$ model predicts the velocity better.

In general, the CFD results are quite satisfactory. There are no siqnificant differences between the measurement results and the CFD results. Most differences are near the hub at the impeller inlet and near the shroud at the impeller exit. The same case with the Finflo solver has been studied also by Rautaheimo et al. (1999). They conclude that Chien's $k - \epsilon$ model pre-

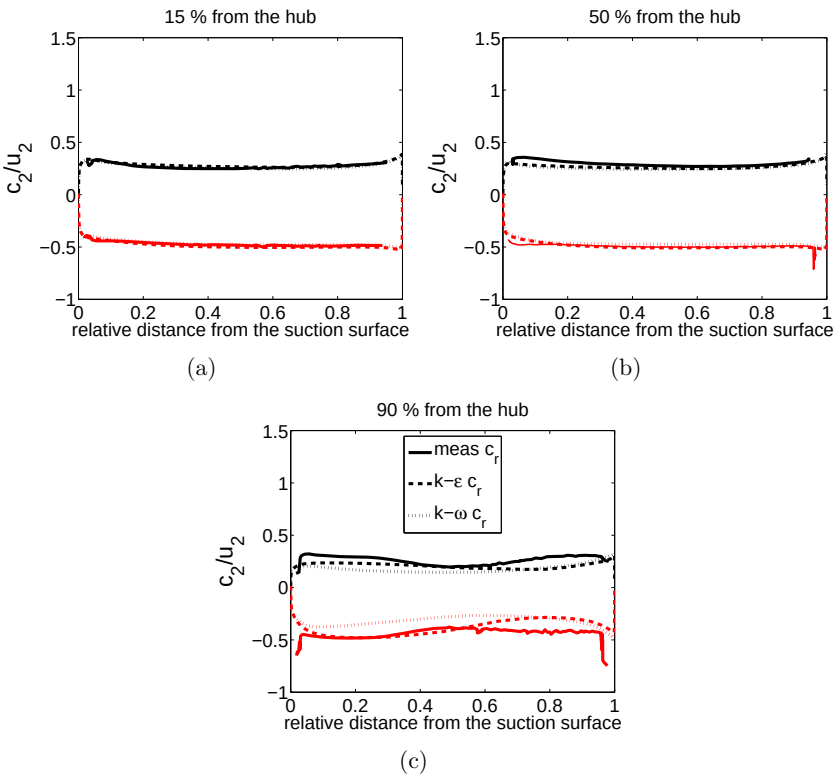

Figure 4.3: Calculation and measurement results at the impeller exit: (a) 15% from the hub, (b) 50% from the hub, and (c) 90% from the hub. Radial velocity in black and tangential in red. Measurements by Hathaway et al. (1995).

dicts the total values, such as total pressure ratio and efficiency well. The efficiency predictions are quite good even with a very coarse grid, although the velocity fields could not be solved accuratly. The velocity fields in the impeller agree qualitatively well with a denser grid.

4.2 Grid sensitivity

To ascertain the CFD results further, a coarse grid sensitivity study was performed. This was done by calculating the unpinched vaneless diffuser with three different grids, which differed from each other only by cell number. In

addition to this, results from the second and third grid level for the grid with least points were inspected. All five cases and their respective cell numbers are presented in Table 4.1. All grid sensitivity calculations have been performed with the $k - \epsilon$ turbulence model.

Table 4.1: Cases and their respective cell numbers in the grid sensitivity study.

grid	grid level	number of cells
grid 1	III	12 885
grid 1	II	88 843
grid 1	I	595 950
grid 2	I	1 222 716
grid 3	I	1 939 146

Total-to-total efficiency, non-dimensionalized with the design efficiency of the compressor stage, and the pressure ratio from the inlet to the diffuser outlet as a function of cell number are presented in Fig. 4.4. Both values have been calculated with mass flow averaged values. The efficiency is defined as

$$\eta_{\mathrm{tt},14} = \frac{T_{\mathrm{ts4}} - T_{\mathrm{t1}}}{T_{\mathrm{t4}} - T_{\mathrm{t1}}} \tag{4.1}$$

The efficiency is smallest with the least number of cells (grid 1 level III). For the first and second grid levels in grid 1, the efficiency increases when the number of cells increases. With grid 2 and grid 3, the efficiency decreases, and there is no significant difference between them. The pressure ratio is lowest with the lowest cell number. When the number of cells increases, the pressure ratio behaves like the efficiency, except that it is lower with gird 3 than with grid 2.

The diffuser total pressure loss coefficient and the diffuser static pressure rise coefficient are presented in Fig. 4.5. The total pressure loss coefficient is defined as

$$K_{\mathrm{p}} = \frac{p_{\mathrm{t}2^*} - p_{\mathrm{t4}}}{p_{\mathrm{t}2^*} - p_{2^*}} \tag{4.2}$$

where subscript 2* denotes the radius ratio of $r_{2^*}/r_2 = 1.036$, which corresponds to the radius with which the measurements after the impeller have been made. The pressure rise coefficient is defined as

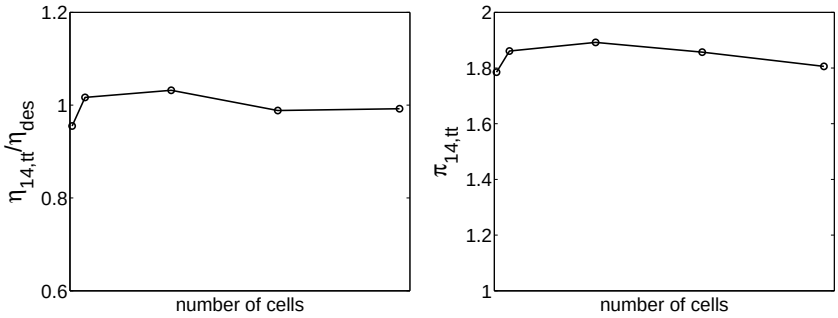

(a) (b)

Figure 4.4: Total-to-total (a) isentropic efficiency and (b) pressure ratio as a function of the number of cells.

$$C_{\mathrm{pr}} = \frac{p_4 - p_{2^*}}{p_{\mathrm{t}2^*} - p_{2^*}} \tag{4.3}$$

In grid 2 and grid 1, levels I and II, there are no major differences between the pressure rise and loss coefficients. The case with the least cells has a somewhat higher pressure loss coeffient and lower pressure rise coefficient, and the case with the most cells has a clearly higher pressure loss coefficient and a somewhat lower pressure rise coefficient.

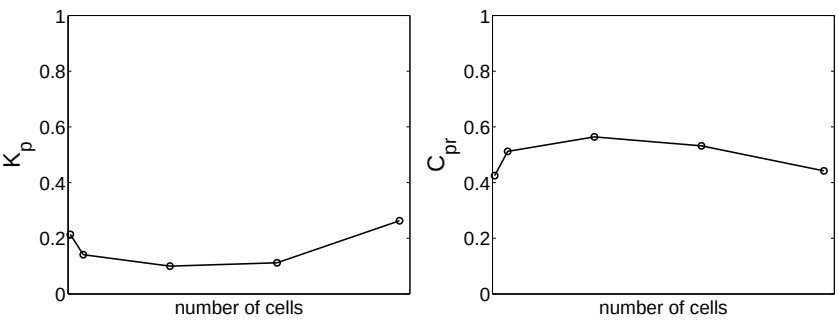

(a) (b)

Figure 4.5: (a) Total pressure rise coefficient and (b) static pressure rise coefficient as a function of the number of cells.

The radial and tangential velocity profiles at the diffuser inlet and outlet are

presented in Fig. 4.6 and Fig. 4.7. The radial velocity profile at the impeller exit, Fig. 4.6, shows that the case with the least cells differs most from the others. It seems that when the cell number increases, there is not so much difference between the other cases, except very near the shroud, where the case with the most cells differs from the others. The radial velocity profiles at the diffuser exit, Fig. 4.6, show that the cases with the least and the most cells differ from the other three. Those cases show the least uniform velocity profile, with higher velocity near the hub and lower near the shroud.

The tangential velocity profiles at the impeller exit, Fig. 4.7, also show that the cases with the most and the least cells differ from the other three cases. The case with the most cells shows higher tangential velocities at the impeller exit, near the shroud, while the case with the least cells has the lowest tangential velocity. The tangential velocity profiles at the diffuser exit, Fig. 4.7, follow the same trend. The cases with the most and the least cells differ from the other three. At the hub, all cases have similar profiles. At the height of 20% from the hub, the two extreme cases begin to differ from the middle three. The case with the least cells has slightly lower tangential velocities at the shroud, and the case with the most cells has the lowest tangential velocity near the shroud, only approximately half of that of the middle three cases.

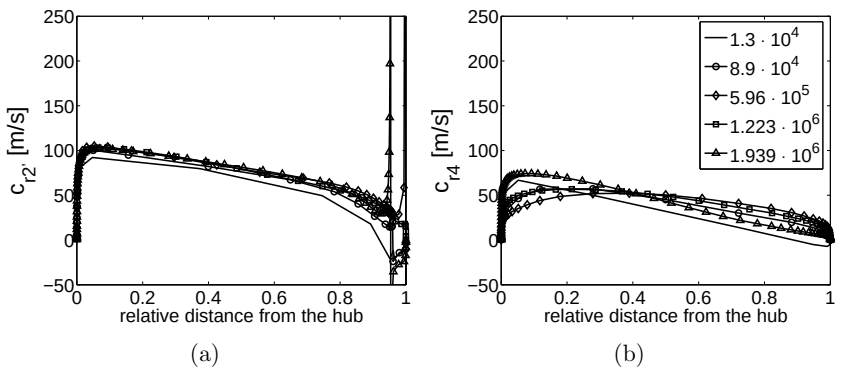

Figure 4.6: Radial velocity distribution at the diffuser (a) inlet and (b) outlet.

The cases with the most and least cells differ more from the other three cases than the other three cases differ from each other. The efficiency and pressure ratio seem to be least affected by the number of cells. The cases with two highest cell numbers have almost the same efficiency. The pressure rise and loss coefficients differ more than the pressure ratios. This, coupled with the

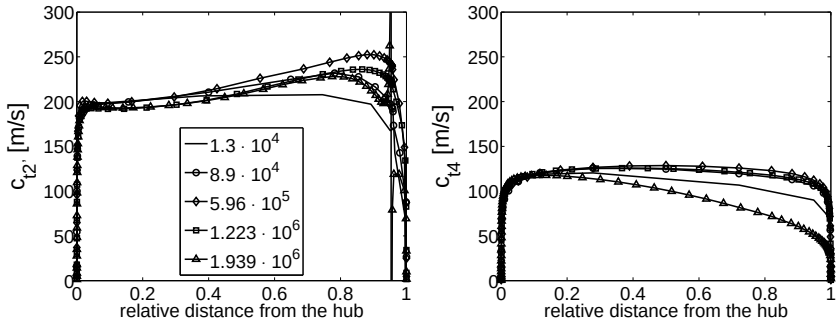

(a) (b)

Figure 4.7: Tangential velocity distribution at the diffuser (a) inlet and (b) outlet.

velocity profiles, seems to indicate that total grid undependency is perhaps not achieved for the diffuser. The radial velocity and pressure distributions in the diffuser for different grid sensitivity cases are presented in Figure 4.8.

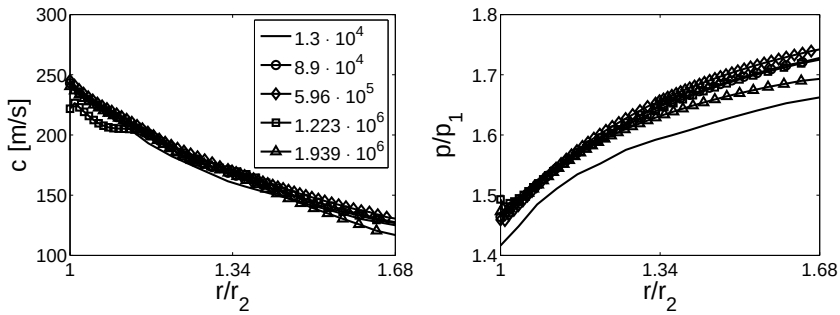

(a) (b)

Figure 4.8: Radial (a) velocity and (b) pressure distributions in the diffuser.

It seems that for the grid with the most cells, the velocity decelerates more in the diffuser. However, also the static pressure rise is the lowest for the said grid, excluding the case with least cells. This means that pressure losses in the diffuser are higher with this grid, as indicated in Figure 4.5. The differences in the radial profiles become evident when the radius ratio is approximately $r/r_2 = 1.34$, which is in the middle of the diffuser. The diffuser grid has

been constructed so that, in the radial direction, the grid is denser at the impeller exit, and then becomes less dense towards the diffuser exit. The reasoning for this is that the flow is more complex at the impeller exit, so the grid should be denser there. It seems that the grid should have been denser also near the diffuser exit. For the other parts it seems that the results are insensitive to the grid.

4.3 Convergence

The convergence of each simulation was monitored. Most important parameters were the L_2 norm of residuals of density, momentum in the $x-$, y- and z-direction, energy, turbulent kinetic energy, and dissipation of turbulent kinetic energy. In addition to these, the average pressure and the average temperature were also important. Examples of convergence history for the $k-\epsilon$ and the $k-\omega$-SST turbulence models for the above mentioned parameters in a vaneless diffuser with $b_{2'}/b_2 = 0.906$ and pinch at the shroud are presented in Fig. 4.9 and Fig. 4.10. Also other parameters, like the mass flow at the inlet, at the outlet and randomly between different blocks, the total energy, total turbulent kinetic energy, and total dissipation of turbulent kinetic energy were also monitored. Only the 1st grid level was used in the simulations. In all simulations were the $k-\epsilon$ turbulence model was used and for the unpinched and vaned diffuser with the $k-\omega$-SST model, the Courant's number was 0.8. For the pinched vaneless diffusers Courant's number of 0.2 was used.

4.4 Vaneless and vaned diffusers

4.4.1 The cases

A tip clearance was modeled to the impeller in all the cases. The modeled tip clearance was 5% of the blade height at the impeller exit. During the measurements, this estimate was found to be very close to the actual tip clearance when the compressor was running. For the vaneless cases, only one impeller passage (from full blade to full blade) and the corresponding sections of diffuser and inlet cones vere modeled, whilst for the vaned diffusers the whole impeller, diffuser and inlet cone were modeled.

Five different vaneless diffuser geometries were modeled. One of the cases was the unpinched original geometry. Three of the other diffusers had widths $b_{2'}/b_2$ of 0.903, 0.854 and 0.806 with the pinch evenly divided for the hub and the shroud. The fifth geometry had the diffuser width $b_{2'}/b_2$ of 0.903

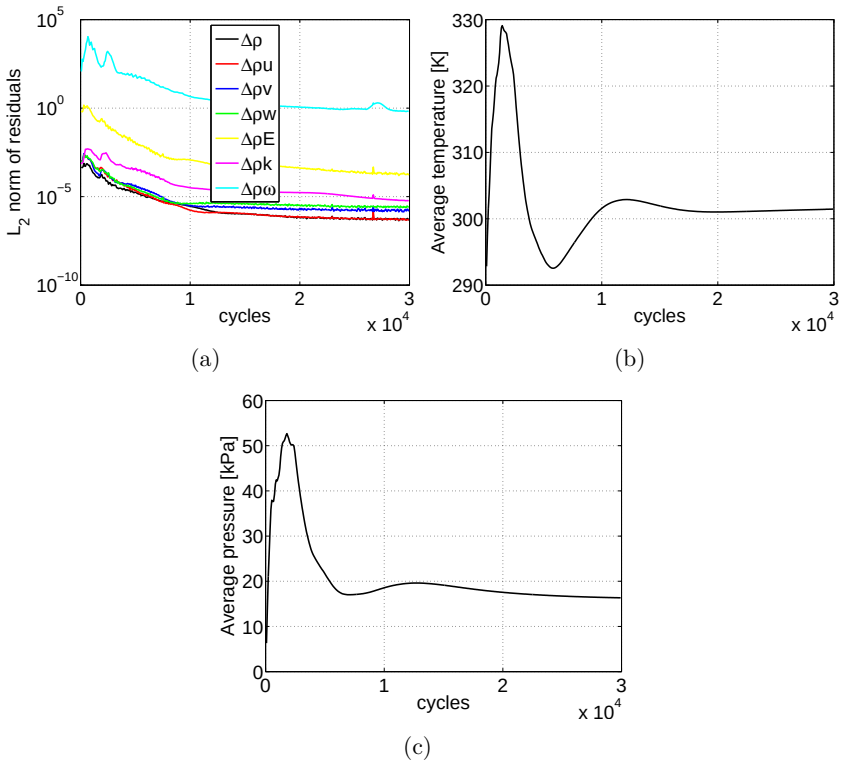

Figure 4.9: Convergence history of $b_{2'}/b_2 = 0.906$, pinch at shroud, $k - \epsilon$ turbulence model (a) L_2 norm of residuals, (b) average temperature, and (c) average pressure.

and the the pinch was implemented only to the shroud. It should be noted that the fifth geometry had the same actual amount of pinch at the shroud as the fourth geometry, which was the narrowest one. A summary of the vaneless diffuser geometries is given in Table 4.2. All the cases were modeled with both the $k - \omega$-SST and $k - \epsilon$ turbulence models, with the design mass flow and the design rotational speed of the original compressor. In all vaneless geometry calculations, a grid with approximately $1.4 \cdot 10^6$ cells was used, except for the unpinched case, which was modeled with approximately $1.2 \cdot 10^6$ cells. This was concluded to enough, based on the grid sensitivity study described above.

The surface grid of the unpinched diffuser in shown in Fig. 4.11. The inlet

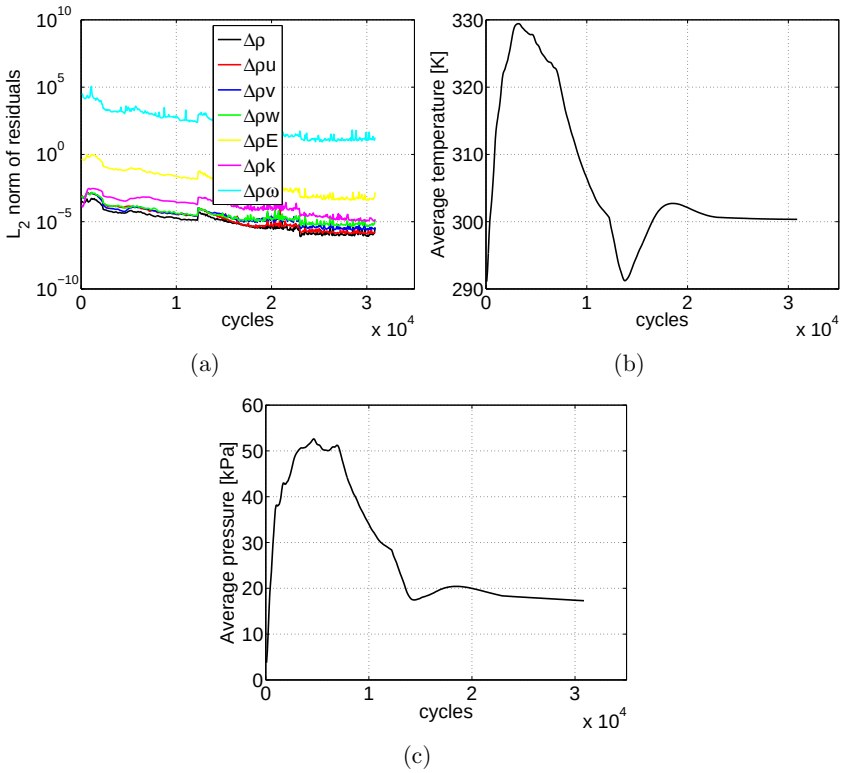

Figure 4.10: Convergence history of $b_{2'}/b_2 = 0.906$, pinch at shroud, $k-\omega$-SST turbulence model (a) L_2 norm of residuals, (b) average temperature, and (c) average pressure.

Table 4.2: Vaneless diffuser constructions.

Case	$b_{2'}/b_2$	$r_{2'}/r_2$	$b_{2'}/r_2$	r_4/r_2	pinch	turbulence model
1	1.000	1.00	0.1217	1.68	unpinched	$k-\epsilon$, $k-\omega$-SST
2	0.903	1.01	0.1098	1.68	hub & shroud	$k-\epsilon$, $k-\omega$-SST
3	0.854	1.01	0.1039	1.68	hub & shroud	$k-\epsilon$, $k-\omega$-SST
4	0.806	1.01	0.0979	1.68	hub & shroud	$k-\epsilon$, $k-\omega$-SST
5	0.903	1.01	0.1098	1.68	shroud	$k-\epsilon$, $k-\omega$-SST

cone is included in the figure, but the shroud plate is not shown. All the pinches were modeled to be rounded (quarter of a circle). Examples of the

pinch are shown in Fig. 4.12.

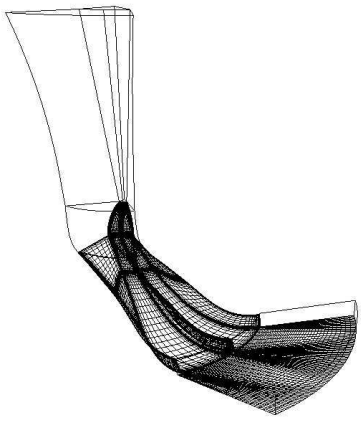

Figure 4.11: Surface grid of the compressor with unpinched geometry, with the inlet cone shown. The shroud plate is not shown.

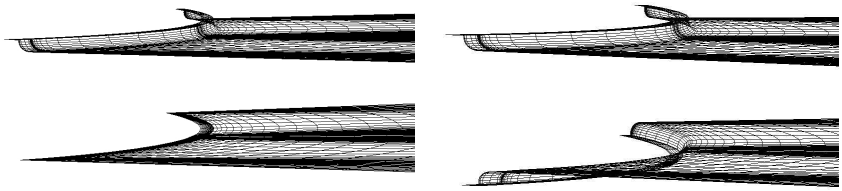

(a) (b)

Figure 4.12: Details of two different pinched constructions (a) $b_{2'}/b_2 = 0.903$, pinch at the shroud, and (b) $b_{2'}/b_2 = 0.806$, pinch at the hub and at the shroud.

Six different vaned diffusers were also modeled at the design operating rotational speed and at the design mass flow. The effect of vane number N

was tested by modeling diffusers with 15, 17, 19 and 23 vanes. The effect of the vane turning angle θ was tested by modeling the 23-vaned diffuser with three different vane turning angles: 10°, 15° and 20°. All the diffusers were circular arc chamber line diffusers with thickness distribution described by Seidel (1994). The summary of the geometries and the used turbulence models are presented in Table 4.3, and the surface grids are presented in Fig. 4.13. Each of the grids used to simulate the vaned diffuser cases had approximately $6.5 \cdot 10^5$ cells. Because a whole of the impeller, diffuser and inlet cone was modeled in the vaned diffuser cases, the $6.5 \cdot 10^5$ cells correspond approximately to $0.9 \cdot 10^5$ cells, when compared to the vaneless simulations. This is close to grid 1, level 2 in the grid sensitivity study, still giving reasonably acceptable results.

Table 4.3: Vaned diffuser constructions.

Case	N	$\theta[°]$	σ	$r_{2'}/r_2$	r_3/r_2	r_4/r_2	turbulence model
n15,θ10	15	10	2.65	1.10	1.68	1.68	$k-\epsilon$, $k-\omega$-SST
n17,θ10	17	10	2.82	1.10	1.64	1.68	$k-\epsilon$, $k-\omega$-SST
n19,θ10	19	10	2.80	1.10	1.58	1.68	$k-\epsilon$
n23,θ10	23	10	2.76	1.10	1.48	1.68	$k-\epsilon$
n23,θ15	23	15	2.56	1.10	1.48	1.68	$k-\epsilon$
n23,θ20	23	20	2.46	1.10	1.48	1.68	$k-\epsilon$, $k-\omega$-SST

4.4.2 Overall compressor performance

The isentropic total-to-static efficiencies of the impeller and the stage (meaning here the impeller and the diffuser combined) of different vaneless geometries are presented in Table 4.4. The values in the table are compared to the unpinched geometry:

$$\Delta\eta = \eta_{\text{case}} - \eta_{\text{unpinched}} \tag{4.4}$$

For the vaneless diffusers, the $k-\epsilon$ turbulence model predicts that both the impeller and the stage efficiencies are lower when the diffuser is pinched. The impeller efficiency is least detoriorated for the diffuser $b_{2'}/b_2 = 0.903$ with the pinch only at the shroud. All other geometries have the same impeller efficiency, which is slightly worse than that of the shroud pinch case. For the stage efficiencies, the best pinched geometry is the one with the largest pinch ($b_{2'}/b_2 = 0.806$) and the worst is the $b_{2'}/b_2 = 0.903$, pinch both at the hub

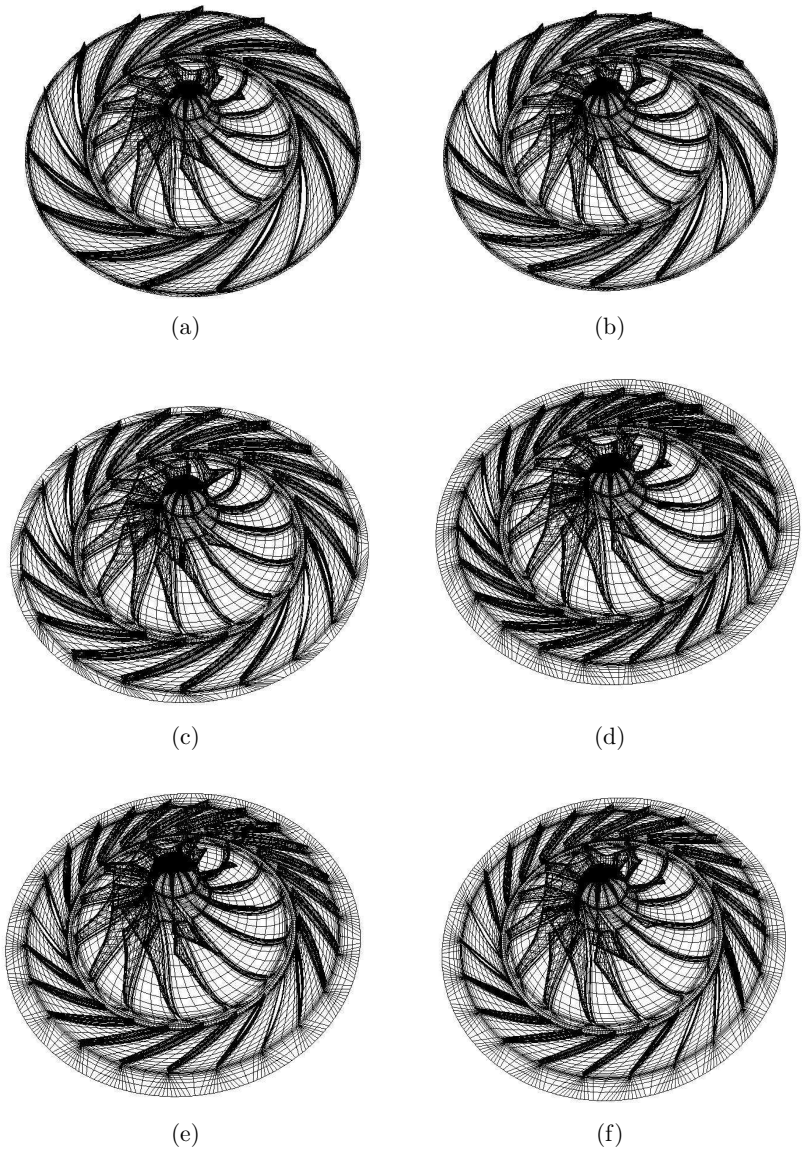

Figure 4.13: Surface grids for the vaned diffuser calculations (a) $N15, \theta 10$, (b) $N17, \theta 10$, (c) $N19, \theta 10$, (d) $N23, \theta 10$, (e) $N23, \theta 15$, and (f) $N23, \theta 20$

and at the shroud, which has 5 percentage points lower efficiency than the

Table 4.4: Total-to-static isentropic efficiency of vaneless diffusers compared to the efficiency of the unpinched geometry.

	$k-\epsilon$		$k-\omega$-SST	
Case	$\Delta\eta_{\mathrm{ts},2^*}$	$\Delta\eta_{\mathrm{ts},4}$	$\Delta\eta_{\mathrm{ts},2^*}$	$\Delta\eta_{\mathrm{ts},4}$
$b_{2'}/b_2 = 0.903$	-0.02	-0.05	-0.01	-0.07
$b_{2'}/b_2 = 0.854$	-0.02	-0.03	-0.01	0.03
$b_{2'}/b_2 = 0.806$	-0.02	-0.02	0.01	0.04
$b_{2'}/b_2 = 0.903$ (shroud)	-0.01	-0.03	0.04	0.04

unpinched geometry.

The $k-\omega$-SST model predicts better impeller efficiencies for the two cases with the greatest shroud pinch and better stage efficiencies for all the pinched geometries, except for $b_{2'}/b_2 = 0.903$, pinch both at the hub and the shroud. The $b_{2'}/b_2 = 0.903$, pinch at the hub and at the shroud has 7 percentage points lower stage efficiency than the unpinched construction. This indicates extremely poor diffuser performance for this geometry. The geometry with the pinch only at the shroud has clearly the best impeller efficiency (4 percentage points better than the unpinched one). The stage efficiency for the case with shroud pinch only is also 4 percentage points better than the efficiency of the unpinched geometry. This might indicate that even though the shroud pinch has the best impeller efficiency, the diffuser does not work as well as in the other pinched cases. According to the $k-\omega$-SST model results, it is possible to improve the stage efficiency by implementing the pinch. Also it seems that the pinch also improves the impeller efficiency.

Even though the $k-\epsilon$ model results suggest that adding pinch detoriorates the impeller and stage efficiencies, it seems that the stage efficiency deteriorates more than the impeller efficiency. For both turbulence models, the $b_{2'}/b_2 = 0.903$, with pinch at the hub and at the shroud, is the worst geometry. For the $k-\epsilon$ model, the one with the most pinch is the least poor geometry and, for the $k-\omega$-SST model the one with pinch only at the shroud has the best impeller efficiency and shared best stage efficiency with the geometry with the most pinch. A rough generalization of the efficiencies is that the narrower the diffuser width, the better the efficiency.

The impeller and stage efficiencies for vaned diffusers are presented in Table 4.5. For the $k-\epsilon$ turbulence model, all the vaned diffusers seem to enhance

the impeller efficiency, except n23,θ15 and n23,θ20, which have the same impeller efficiency than the unpinched baseline geometry. However, only three of the six vaned diffuser geometries have better stage efficiency than the unpinched geometry; n15,θ10, n23,θ15 and n23,θ20. For the stage efficiency, it seems that a larger vane turning angle means better efficiency. The effect of the vane number is not so clear, as the geometries with the least and the most vanes have the best efficiencies. Looking at the $k-\omega$-SST turbulence model results, the effect to the impeller efficiency is similar to the one with the $k-\epsilon$ model. For the stage efficiency, the one with least vanes (also the one with the longest vanes) has the best efficiency, the one with most vanes (also the shortest vanes) has the second best stage efficiency, and the one with 17 vanes falls between these two cases.

Table 4.5: Total-to-static isentropic efficiency of vaned diffusers compared to the efficiency of the unpinched vaneless geometry.

	$k-\epsilon$		$k-\omega$-SST	
Case	$\Delta\eta_{\mathrm{ts},2^*}$	$\Delta\eta_{\mathrm{ts},4}$	$\Delta\eta_{\mathrm{ts},2^*}$	$\Delta\eta_{\mathrm{ts},4}$
n15,θ10	0.01	0.02	0.01	0.05
n17,θ10	0.01	0.00	0.01	0.01
n19,θ10	0.03	0.00	-	-
n23,θ10	0.02	0.00	-	-
n23,θ15	0.00	0.01	-	-
n23,θ20	0.00	0.02	0.00	0.03

The impeller and the stage total-to-static pressure ratios for the vaneless diffusers are presented in Table 4.6. Similar to the efficiency, the pressure ratios of different geometries are also compared to the unpinched geometry.

The $k-\epsilon$ model predicts lower impeller pressure ratios and even lower stage pressure ratios for the narrower diffusers. It seems that there is no notable difference between the different pinches. The $k-\omega$-SST model predicts all pinched geometries to have higher impeller pressure ratios than the unpinched geometry. Looking at the stage pressure ratios, only the $b_{2'}/b_2 = 0.903$ (hub and shroud) has to some extent a higher stage pressure ratio than the unpinched one. All the other vaneless geometries have a lower stage pressure ratio than the unpinched one. The pinch makes the flow path shorter in the diffuser, and thus there is less space for the flow to decelerate, which should lead to lower static pressure at the diffuser outlet. The shorter flow path

Table 4.6: Total-to-static pressure ratios of vaneless constructions compared to the unpinched geometry.

	$k-\epsilon$		$k-\omega$-SST	
Case	$\Delta\pi_{\mathrm{ts},2^*}$	$\Delta\pi_{\mathrm{ts},4}$	$\Delta\pi_{\mathrm{ts},2^*}$	$\Delta\pi_{\mathrm{ts},4}$
$b_{2'}/b_2 = 0.903$	-0.04	-0.08	0.03	0.01
$b_{2'}/b_2 = 0.854$	-0.04	-0.07	0.02	-0.12
$b_{2'}/b_2 = 0.806$	-0.04	-0.06	0.03	-0.10
$b_{2'}/b_2 = 0.903$ (shroud)	-0.04	-0.08	0.04	-0.13

should lead to lower friction losses. However, the pinch must increase the flow velocity to fulfill the continuation equation, which should lead to slightly higher friction losses.

The impeller and stage total-to-static pressure ratios for the vaned cases are presented in Table 4.7. The $k-\epsilon$ model results predict that all the vaned geometries have lower pressure ratios than the unpinched geometry. The $k-\omega$-SST model results indicate higher impeller pressure ratios, the highest for the n15,θ10, and about half of that for the n17,θ10 and the n20,θ20. The stage pressure ratios are lower than those of the unpinched geometry for the n17,θ10 and n20,θ20.

Table 4.7: Total-to-static pressure ratios for the vaned costructions compared to the unpinched vaneless geometry

	$k-\epsilon$		$k-\omega$-SST	
Case	$\Delta\pi_{\mathrm{ts},2^*}$	$\Delta\pi_{\mathrm{ts},4}$	$\Delta\pi_{\mathrm{ts},2^*}$	$\Delta\pi_{\mathrm{ts},4}$
n15,θ10	-0.02	-0.02	0.11	0.04
n17,θ10	-0.03	-0.06	0.06	-0.05
n19,θ10	0.00	-0.03	-	-
n23,θ10	-0.02	-0.03	-	-
n23,θ15	-0.03	-0.03	-	-
n23,θ20	-0.02	-0.01	0.06	-0.06

When the diffuser performance is considered, the total pressure loss and static pressure rise coefficients are compared. The coefficients for the vaneless cases are presented in Table 4.8. Like the efficiencies and pressure ratios, also the

pressure loss and rise coefficents are compared to the those of the unpinched geometry. The pressure loss coefficient is calculated with Eq. 4.2, and the pressure rise coefficient with Eq. 4.3.

Table 4.8: Total pressure loss and static pressure rise coefficients for the vaneless diffusers compared to the unpinched geometry

	$k-\epsilon$		$k-\omega$-SST	
Case	ΔK_{p}	ΔC_{pr}	ΔK_{p}	ΔC_{pr}
$b_{2'}/b_2 = 0.903$	0.18	-0.12	0.02	-0.09
$b_{2'}/b_2 = 0.854$	0.16	-0.08	-0.06	-0.08
$b_{2'}/b_2 = 0.806$	0.15	-0.08	-0.09	-0.11
$b_{2'}/b_2 = 0.903$ (shroud)	0.16	-0.10	-0.05	0.05

The $k-\epsilon$ model predicts higher pressure losses and lower pressure rises for the pinched geometries. The $k-\omega$-SST model, on the other hand, predicts lower pressure losses and lower pressure rise coefficients for the $b_{2'}/b_2 = 0.806$ and 0.854. This seems to be in line with the speculations presented above that the shorter flow path leads to a lower static pressure rise and lower total pressure losses in the diffuser. The $b_{2'}/b_2 = 0.903$ (hub & shroud) has a higher pressure loss coefficient and lower pressure rise coefficient, whilst for the $b_{2'}/b_2 = 0.903$ (shroud), it is the other way round.

The total pressure loss and static pressure rise coefficients of the vaned diffuser are presented in Table 4.9. Considering the $k-\epsilon$ turbulence model results, it seems logigal that all the vaned diffusers have a higher pressure loss coefficient. The lower the turning angle (longer flow path), the higher the pressure loss. Also the higher the turning angle, the higher the pressure rise coefficient. About the effect of the vane number, it is hard to say anything. The $k-\omega$-SST turbulence model results predict lower pressure loss and even a higher pressure rise coefficient than the $k-\epsilon$ turbulence model results.

As regards the different indicators of the overall compressor performance, it seems quite possible to improve the performance of a centrifugal compressor by implementing a narrower diffuser (pinch) according to the $k-\omega$-SST turbulence model results. The $k-\omega$-SST model predicts the geometry $b_{2'}/b_2$ = 0.903 (shroud) to be the best. For the vaned diffusers, it seems that the one with the least vanes (15) or the one with the most vanes (23) and the largest vane turning angle (20°) are the two best options.

Table 4.9: Total pressure loss and static pressure rise coefficients for the vaned diffusers compared to the unpinched vaneless geometry

	$k-\epsilon$		$k-\omega$-SST	
Case	ΔK_{p}	ΔC_{pr}	ΔK_{p}	ΔC_{pr}
n15,θ10	0.07	0.07	-0.01	0.27
n17,θ10	0.12	-0.01	-0.03	0.16
n19,θ10	0.09	0.03	-	-
n23,θ10	0.09	-0.01	-	-
n23,θ15	0.08	0.06	-	-
n23,θ20	0.05	0.12	-0.07	0.22

4.4.3 Flow fields

The velocity and flow angle profiles before and after the diffuser are mass flow averaged in the circumferential direction. Absolute flow angles (from the radial direction) before and after the diffuser for the vaneless diffusers with the $k-\epsilon$ turbulence model are presented in Figure 4.14. Before the diffuser, there are no major differences between the different pinched geometries, the trend being that the narrower the diffuser, the more radial the flow is. The unpinched geometry has slightly more tangential flow, and the difference between the unpinched and different pinched cases is larger than the differences between the different pinched cases. After the diffuser, the effects of different pinches are more evident. The unpinched case has clearly more tangential flow nearer the hub, the difference being almost 20° at the hub. At the channel widths b/b_{shroud} of approximately 0.5 and above, the geometry $b_{2'}/b_2 = 0.903$ (hub & shroud) has the maximum tangential flow. Nearer to the hub, the different pinched geometries have similar angle profiles, differences become evident when the relative distance from the hub b/b_{shroud} is approximately 0.3 and above. Nearer to the shroud, the geometry with the largest pinch has the maximum radial flow. The case with the second largest pinch has the second most radial flow. The unpinched geometry has the third most radial flow, and the case with pinch only at the shroud has the second most tangential flow.

Absolute flow angle distributions before and after the diffuser for the vaneless diffusers with the $k-\omega$-SST turbulence model are presented in Figure 4.15. Like with the $k-\epsilon$ model, also the $k-\omega$-SST model results indicate that there are no major differences between the different pinched cases. At

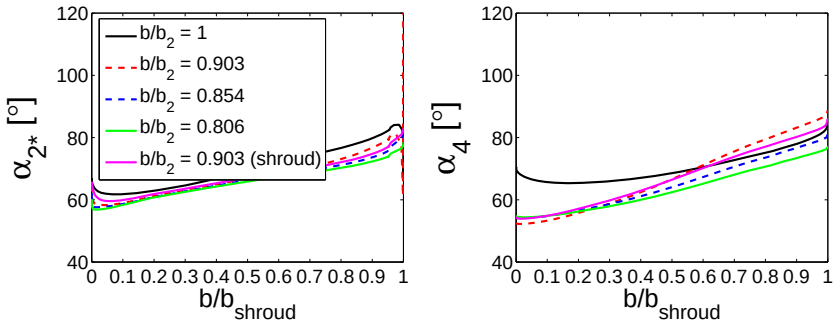

(a) (b)

Figure 4.14: Absolute flow angels for different vaneless geometries (a) before and (b) after the diffuser, $k - \epsilon$ turbulence model.

the diffuser inlet, the unpinched geometry has quite a large backflow area near the shroud (spanning for about 20% from the shroud). So it seems that adding the pinch clearly makes the flow field at the diffuser inlet more homogenous. After the diffuser the case $b_{2'}/b_2 = 0.903$ (hub & shroud) has total flow failure in the diffuser. For about the 40% of the channel width from the shroud, the flow direction reverses. This explains the very poor efficiency for this geometry. Possible benefits of the pinch for the other geometries are seen, however. The unpinched geometry has still a backflow area near the shroud. The other pinched geometries have no such area.

Absolute flow velocity profiles before and after the diffuser for the vaneless diffusers with the $k - \epsilon$ model are presented in Figure 4.16. The flow velocity profiles at the diffuser inlet show a similar trend as the flow angle distributions. The unpinched geometry has slightly lower velocity throughout the diffuser width. There are no significant differences between the different pinched geometries. After the diffuser, the unpinched geometry has the highest flow velocity. The geometry with pinch only at the shroud has the second highest flow velocity. For the three geometries with pinch both at the hub and the shroud there are no significant differences.

Absolute flow velocity profiles with the $k - \omega$-SST turbulence model for the vaneless diffusers at the diffuser inlet and diffuser outlet are presented in Figure 4.17. The $k - \omega$-SST model results show more differences between the different geometries, especially near the shroud. The unpinched geometry has the largest slow flow region near the shroud, while the geometry with

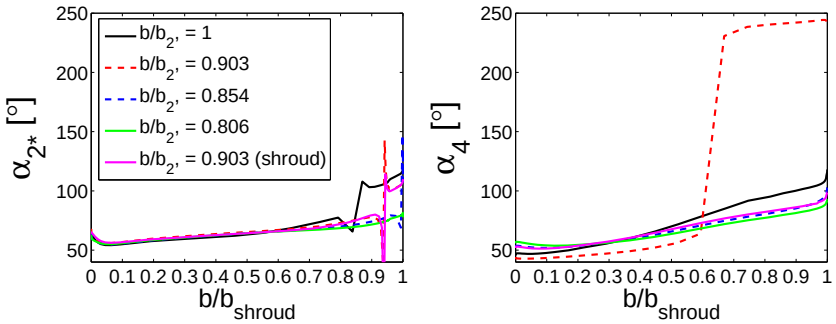

(a) (b)

Figure 4.15: Absolute flow angels for different vaneless geometries (a) before and (b) after the diffuser, $k-\omega$-SST turbulence model.

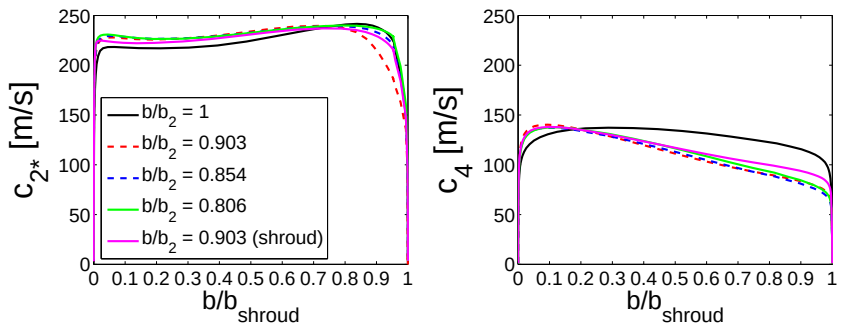

(a) (b)

Figure 4.16: Absolute flow velocities for different vaneless geometries(a) before and (b) after the diffuser, $k-\epsilon$ turbulence model.

pinch only at the shroud shows the second largest slow flow region. The case $b_{2'}/b_2 = 0.903$ (hub & shroud) has the third largest slow flow region, and the case with most pinch has the smallest slow flow region. After the diffuser, the reversed flow of the $b_{2'}/b_2 = 0.903$ (hub & shroud) also alters the velocity profile. The unpinched case has the second lowest flow velocities. For the other three geometries, there are no great differences between the velocity profiles. The shroud pinch has the slowest velocity and the one with the most pinch has the largest velocity of the three geometries.

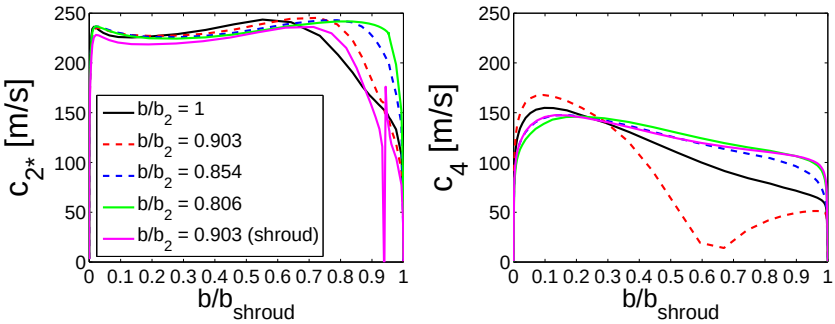

(a) (b)

Figure 4.17: Absolute flow velocities for different vaneless geometries(a) before and (b) after the diffuser, $k-\omega$-SST turbulence model.

The radial and tangential velocity components are calculated using the flow angle and the absolute flow velocity. The radial velocity is defined as

$$c_{\mathrm{r}} = \cos\alpha \cdot c \tag{4.5}$$

and the tangential velocity is defined as

$$c_{\mathrm{r}} = \sin\alpha \cdot c \tag{4.6}$$

The radial and tangential velocity distributions before and after different vaneless diffusers with the $k-\epsilon$ turbulence model are presented in Figures 4.18 and 4.19, respectively. Before the diffuser, it seems that the implementation of the pinch has more effect than the actual amount of the pinch. The unpinched geometry has the lowest radial velocity, and the other geometries have slightly higher radial velocities. The case with most pinch has the highest velocity, and then, logically, when the amount of pinch decreases, the radial velocity decreases. The direct effect of the amount of pinch is seen more clearly in the velocity profiles after the diffuser. The unpinched geometry has clearly lower radial velocity nearer to the hub. In the tangential velocity profiles there are no significant differences with different pinches. The unpinched geometry has the highest tangential velocity near the shroud at the diffuser inlet and clearly the highest tangential velocity after the diffuser. After the diffuser, the shroud pinch geometry has the second highest tangential velocity.

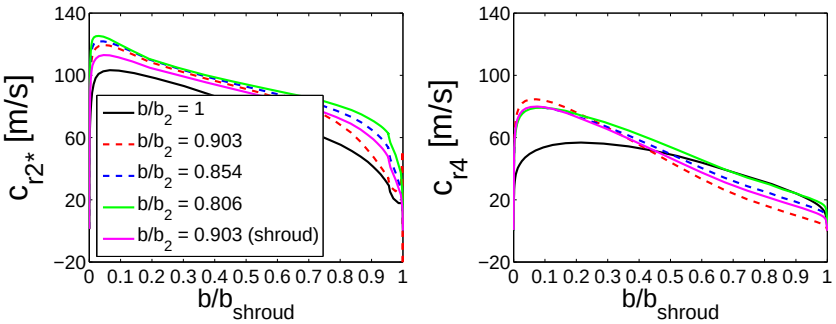

(a) (b)

Figure 4.18: Radial velocities for different vaneless geometries(a) before and (b) after the diffuser, $k - \epsilon$ turbulence model.

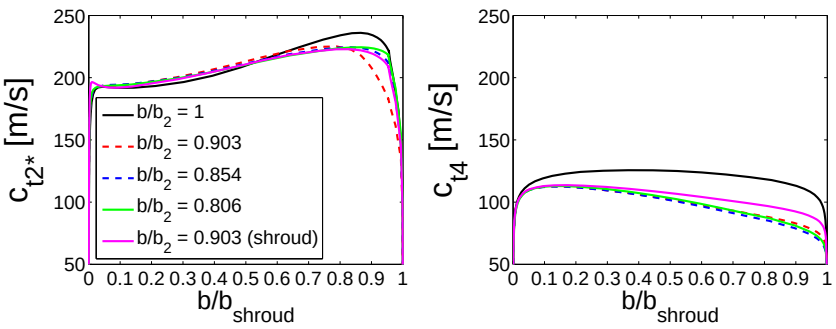

(a) (b)

Figure 4.19: Tangential velocities for different vaneless geometries(a) before and (b) after the diffuser, $k - \epsilon$ turbulence model.

Radial and tangential velocity profiles for different vaneless diffusers with the $k - \omega$-SST turbulence model are presented in Figures 4.20 and 4.21, respectively. The stabilizing effect of pinch is seen clearly. After the impeller, the unpinched geometry has quite a large backflow area, while the case with most pinch has the most uniform radial velocity profile. After the diffuser, the reverse flow for the $b_{2'}/b_2 = 0.903$, pinch at the hub and at the shroud is clearly shown. The unpinched geometry has quite a large slow radial velocity region near the shroud, where the radial velocity is around zero. The case with the most pinch has the highest radial velocity, as it should have. The

tangential velocity profiles are similar to those of the $k-\epsilon$ model, except the $b_{2'}/b_2 = 0.903$, pinch at the hub and at the shroud. It seems that increasing the pinch decreases the boundary layer thickness. One explanation for the very poor (or non-existing) diffuser performance for the $b_{2'}/b_2 = 0.903$, pinch at the hub and at the shroud diffuser might be that the actual amount of pinch is smaller than the boundary layer for the unpinched geometry, so that it would not possess the stabilazing effect the other pinches do. However, the small amount of pinch would still be enough to disturb the flow, causing the boundary layer to separate later.

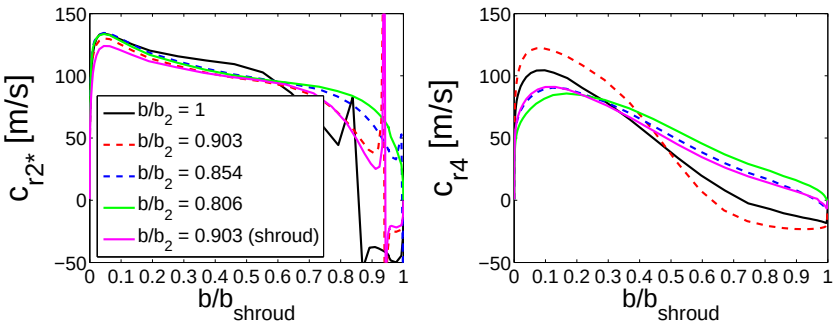

(a) (b)

Figure 4.20: Radial velocities for different vaneless geometries(a) before and (b) after the diffuser, $k-\omega$-SST turbulence model.

Efficiency comparisons (Table 4.4) suggest that the pinch also might improve the impeller efficiency. The major reason is most likely the stabilizing effect the pinch seems to have on the flow field at the impeller exit. In order to find other possible explanations for the better impeller efficiencies, the relative tangential velocities in the tip clearance over the full blade for different vaneless diffusers are presented in Figure 4.22. For the $k-\epsilon$ turbulence model there are some indications that adding the pinch has some effect for the flow in the tip clearance. It seems that the amount of pinch at the shroud is the parameter affecting the flow velocity in the tip clearance most. The cases with least pinch at the shroud have slightly lower flow velocity in the tip cleareance than the unpinched, while the two geometries with the most pinch at the shroud have significanly lower relative tangential velocities over the blade. The $k-\omega$-SST turbulence model results show a similar trend, but the differences are more evident. The case with the least pinch at the shroud have somewhat lower relative tangential velocity at the tip clearance. The

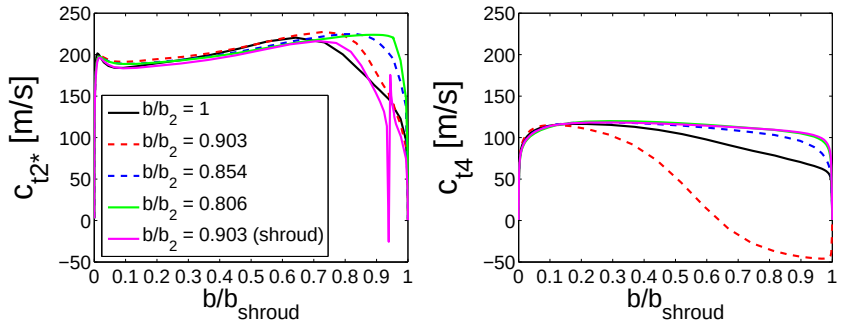

(a) (b)

Figure 4.21: Tangential velocities for different vaneless geometries(a) before and (b) after the diffuser, $k-\omega$-SST turbulence model.

cases with more pinch at the shroud have significantly lower velocity in the tip clearance than the unpinched geometry. The effect is seen for the last 15% of the meridional distance of the full blade. Lower tangential velocity at the tip clearance leads to lower tip leakage flow, and this should lead to lower secondary flow and losses, which should then lead to higher impeller efficiency.

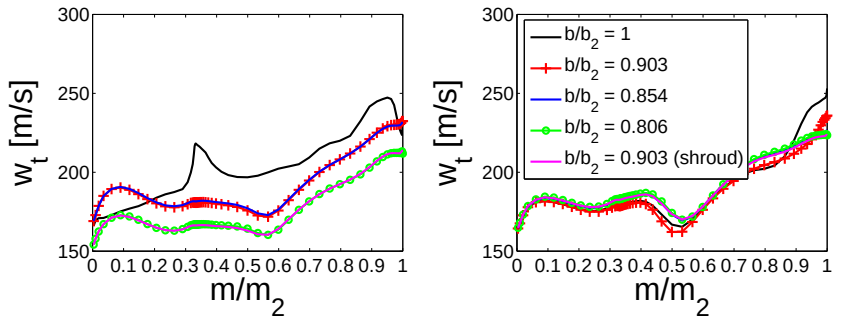

(a) (b)

Figure 4.22: Relative tangential velocity in the tip clearance over the full blade with both turbulence models: (a) $k-\epsilon$ model (b) $k-\omega$-SST model.

The absolute flow angles for the different vaned geometries are presented in Figures 4.23, 4.24 and 4.25. There are no major differences in the flow angles

before the diffuser between the vaned and vaneless diffusers for the $k-\epsilon$ model. The effect of vane number is clearly seen in the velocity profiles after the diffuser. The more vanes there are (the shorter the vanes), the more tangential the flow is. The effect of the vane turning angle is also evident in Figure 4.24. There are no significant differences between the different vane turning angles before the diffuser. After the diffuser, the vane with the largest turning angle has the most radial flow. Reducing the turning angle leads to more tangential flow, the difference between the geometries with most and least vane turning being as much as almost 20°. Considering the differences between the two turbulence models, it seems that before the diffuser there are only minor differences, except for the 15-vaned diffuser. For the 15-vaned diffuser, the $k-\omega$-SST model predicts more tangential flow at the diffuser inlet. There are no such backflow regions in the vaned diffusers, as in the unpinched vaneless diffuser. In general there are even less differences between the turbulence models in the flow angles after the diffuser. However, for the 23-vaned diffuser with the largest vane turning angle, the $k-\omega$-SST model predicts a reversed flow near the hub, which $k-\epsilon$ model did not predict.

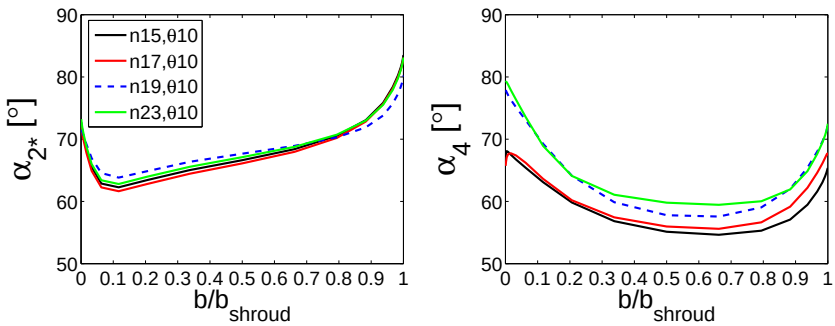

(a) (b)

Figure 4.23: Absolute flow angels for vaned diffusers with different vane number (a) before and (b) after the diffuser, $k-\epsilon$ turbulence model.

The absolute flow velocity profiles before and after the diffuser for the diffusers with the same vane turning angle are presented in Figure 4.26. For the $k-\epsilon$ turbulence model, the flow velocities after the impeller in the diffusers with the same vane turning angle but different vane number are exactly the same, except for the 19-vaned diffuser, which has somewhat lower flow velocity. At the diffuser outlet, the diffuser with most vanes has the highest absolute flow velocity, with the velocity decreasing when the vane number

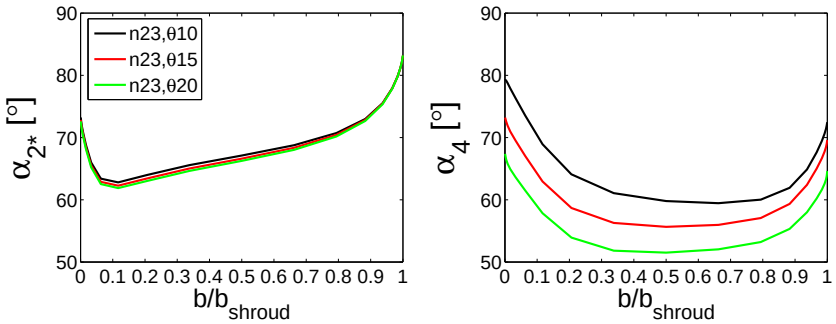

(a) (b)

Figure 4.24: Absolute flow angels for vaned diffusers with different vane turning angle (a) before and (b) after the diffuser, $k - \epsilon$ turbulence model.

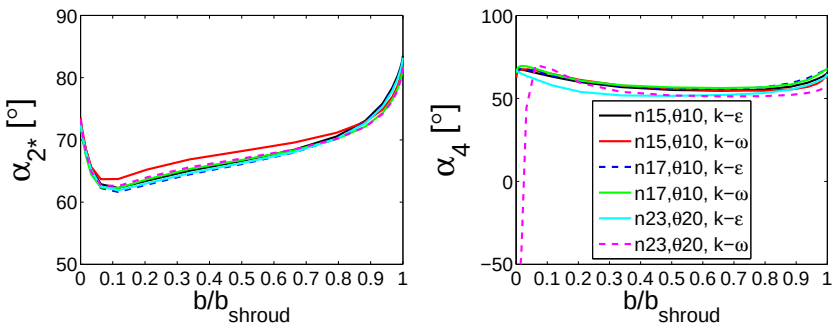

(a) (b)

Figure 4.25: Absolute flow angels for vaned diffusers with both turbulence modeles(a) before and (b) after the diffuser.

decreases. The flow velocities are lower than those of the vaneless diffusers. The same velocity profiles for the diffusers with different vane turning angles are presented in Figure 4.27. There are no differences whatsoever in the flow velocities before the diffuser. After the diffuser, the geometry with the largest vane turning angle has the slowest velocity, and the velocity increases when the turning angle decreases. The flow velocity profiles with both turbulence models are presented in Figure 4.28. There are no major differences between the turbulence models. In general the velocity profiles after the diffuser resemble those of the unpinched geometry, but the velocities are slower for the

vaned geometries.

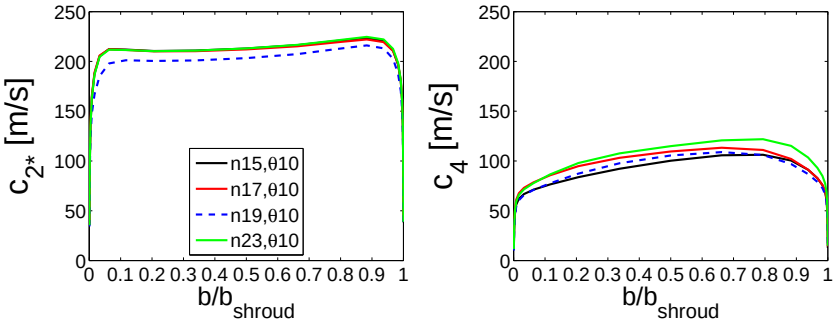

(a) (b)

Figure 4.26: Absolute flow velocities for vaned diffusers with different vane number (a) before and (b) after the diffuser, $k - \epsilon$ turbulence model.

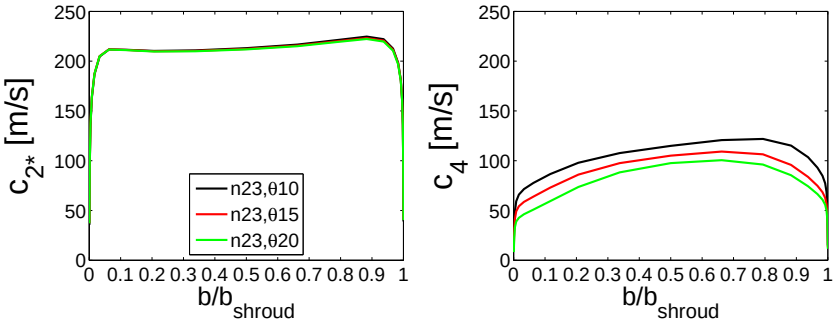

(a) (b)

Figure 4.27: Absolute flow velocities for vaned diffusers with different vane turning angle (a) before and (b) after the diffuser, $k - \epsilon$ turbulence model.

The radial components of the absolute flow velocity before and after the diffuser in the diffusers with the same vane turning angle and the $k - \epsilon$ turbulence model are presented in Figure 4.29. The radial velocities before the diffuser for all the vaned geometries, except the 19-vaned one, are quite similar to those of the unpinched vaneless diffuser. The 19-vaned diffuser has lower radial velocity. After the diffuser, the 17-vaned diffuser has the highest

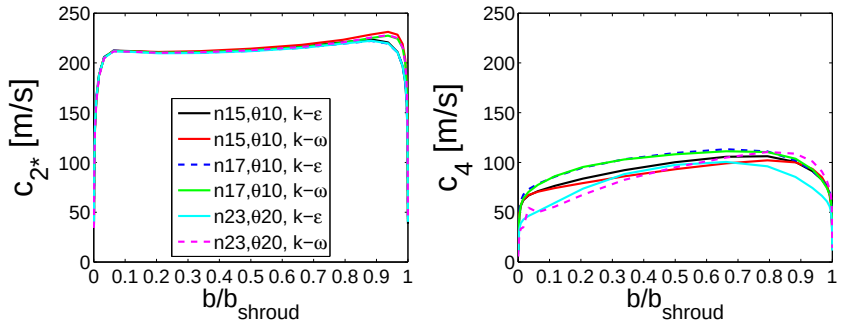

(a) (b)

Figure 4.28: Absolute flow velocities for vaned diffusers with both turbulence models (a) before and (b) after the diffuser.

radial velocity, the-15 vaned has the second highest, and the 19-vaned one has the lowest radial velocity. The radial velocities with the $k-\epsilon$ turbulence model for different vane turnign angles are presented in Figure 4.30. The vane turning angle seems to have only a minor effect on the radial velocity. This seems to be the case before and after the diffuser. The radial velocity distribution for the two turbulence models are presented in Figure 4.31. The differences before the diffuser are minor. The $k-\omega$-SST turbulence model predicts slighlty lower flow velocities than the $k-\epsilon$ model. For the 15 and 17-vaned diffusers, the radial velocity profiles after the diffuser with both turbulence models resemble each other. For the n23,θ20 diffuser, the $k-\omega$-SST model indicates reversed flow at the hub. In general the radial velocity profiles before the diffuser resemble that of the unpinched vaneless diffuser. After the diffuser the, radial velocity profiles differ. Unlike for the vaneless unpinched geometry, for the vaned diffuser the radial velocity is higher nearer the shroud and lower nearer the hub.

The tangential velocities before and after the diffuser for different vane numbers with the $k-\epsilon$ turbulence model are presented in Figure 4.32. The diffuser with 19 vanes has slightly lower tangential velocity before the diffuser than the other three. The trends of the tangential velocities before the vaned diffusers are similar to that of the unpinched vaneless diffuser. The velocities for the vaned diffuser are somewhat slower. At the diffuser outlet, the diffuser with most vanes has the highest tangential velocity, and the one with the least vanes has the highest tangential velocity. The effect of the vane turning angle on the tangential velocity profile is shown in Figure 4.33.

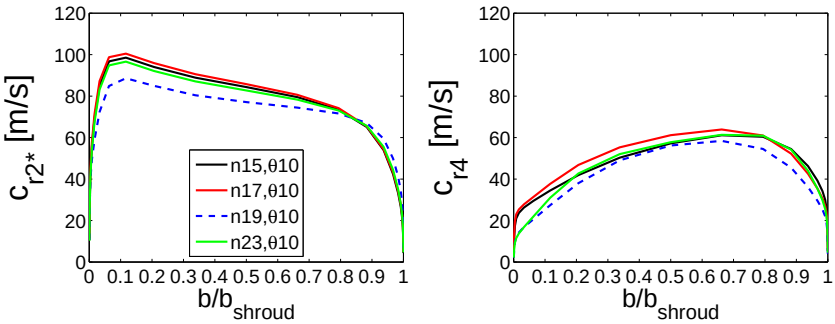

(a) (b)

Figure 4.29: Absolute radial flow velocities for vaned diffusers with different vane numbers (a) before and (b) after the diffuser, $k - \epsilon$ turbulence model.

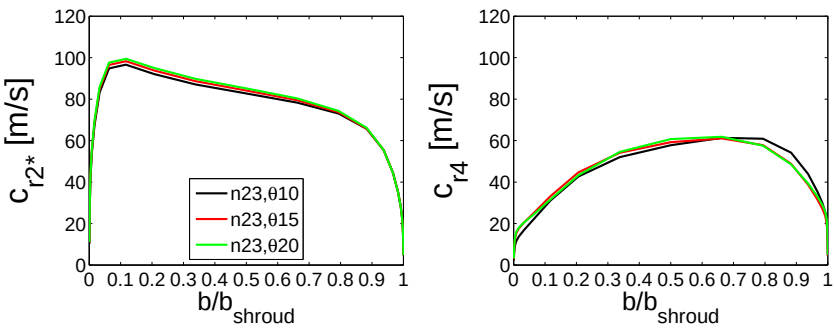

(a) (b)

Figure 4.30: Absolute radial flow velocities for vaned diffusers with different vane turning angle (a) before and (b) after the diffuser, $k - \epsilon$ turbulence model.

There are no significant differences between the different turning angles before the diffuser. At the diffuser outlet, the diffuser with the largest vane turning has the lowest tangential velocity, and the one with the least vane turning has the highest tangential velocity. The difference of the turbulence models are shown in Figure 4.34. The turbulence model does not have much impact on the tangential velocity.

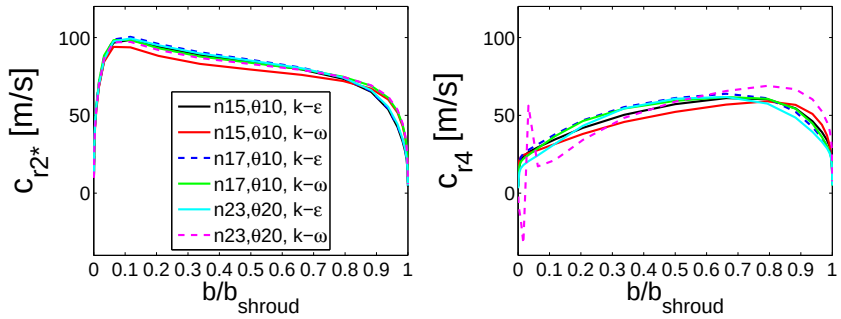

(a) (b)

Figure 4.31: Absolute radial flow velocities for vaned diffusers with both turbulence models (a) before and (b) after the diffuser.

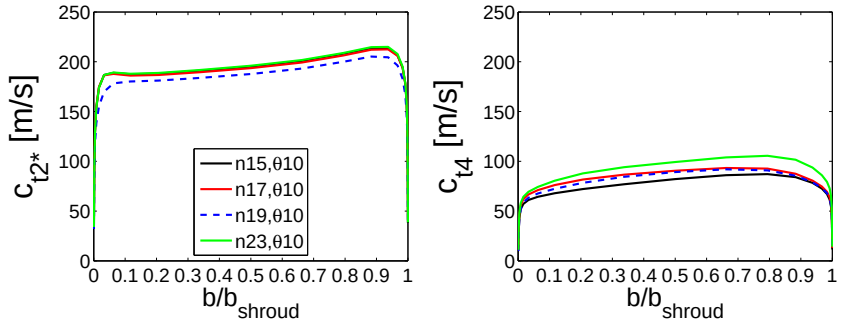

(a) (b)

Figure 4.32: Absolute tangential flow velocities for vaned diffusers with different vane numbers (a) before and (b) after the diffuser, $k - \epsilon$ turbulence model.

4.5 Comparison between the $k - \epsilon$ and $k - \omega$-SST turbulence models

Streamlines in the vaneless diffuser for selected cases (unpinched, $b_{2'}/b_2 = 0.903$ and $b_{2'}/b_2 = 0.903$ (shroud)), with both $k-\epsilon$ and $k-\omega$-SST turbulence models are presented in Figures 4.35, 4.36 and 4.37. In the streamline figures it is clearly seen that the $k - \omega$-SST turbulence model predicts the flow to be more complex at the impeller exit. With the $k - \epsilon$ model, there is a clear back flow area only just after the impeller for the unpinched construction.

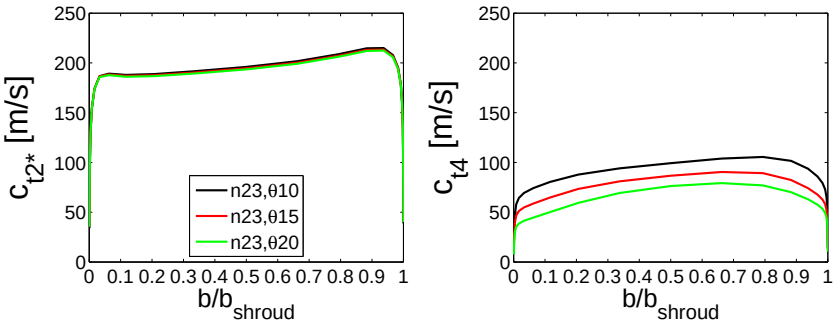

(a) (b)

Figure 4.33: Absolute tangential flow velocities for vaned diffusers with a different vane turning angle (a) before and (b) after the diffuser, $k-\epsilon$ turbulence model.

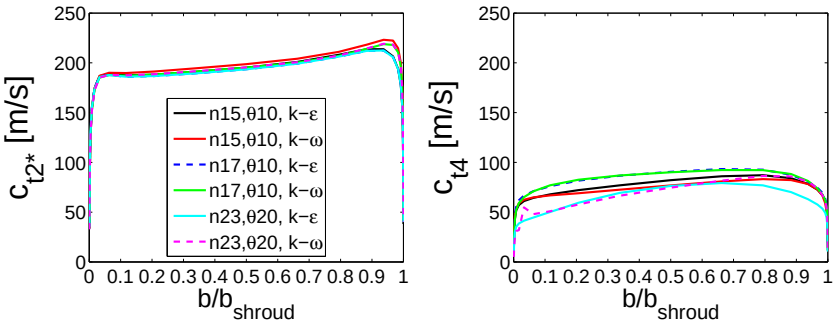

(a) (b)

Figure 4.34: Absolute tangential flow velocities for vaned diffusers with both turbulence models (a) before and (b) after the diffuser.

The $k-\omega$-SST model predicts that there is a back flow area immediately after the impeller with all three geometries. In these figures, the anomalities in the $b_{2'}/b_2 = 0.903$ diffuser shown in Figure 4.15, are not seen. To illustrate the anomality with the streamlines, an another streamline figure for this diffuser is presented in Figure 4.38. Qualitatively, the differences of the two turbulence models are clear. With the $k-\omega$-SST turbulence model in the upper part of the diffuser, the flow direction is more clearly towards the impeller.

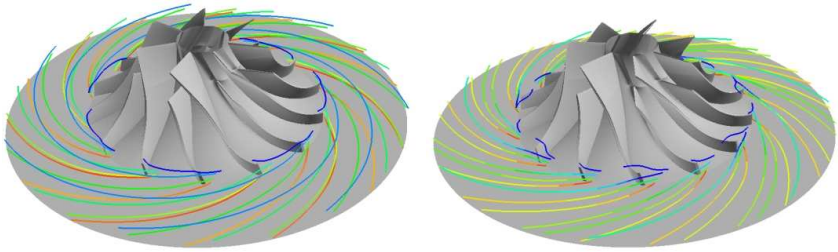

(a) (b)

Figure 4.35: Streamlines in the unpinched vaneless diffuser. The colder the color, the nearer to the shroud the streamline is. (a) $k-\epsilon$ and (b) $k-\omega$-SST.

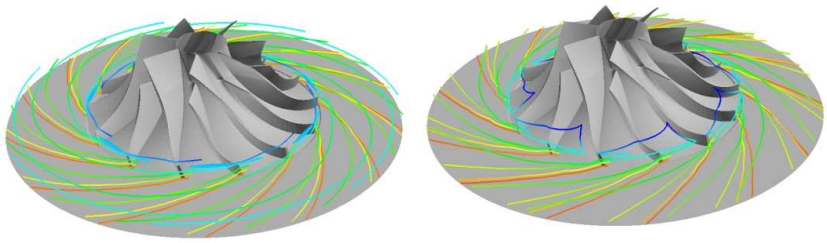

(a) (b)

Figure 4.36: Streamlines in the $b_{2'}/b_2 = 0.903$ vaneless diffuser. The colder the color, the nearer to the shroud the streamline is. (a) $k-\epsilon$ and (b) $k-\omega$-SST.

To compare the two turbulence models further, radial velocity profiles after the impeller and diffuser, near the shroud and the hub, for the three geometries, are presented in Figures 4.39, 4.40 and 4.41. With the unpinched geometry after the impeller, near the hub, the $k-\omega$-SST model predicts somewhat higher radial velocity than the $k-\epsilon$ model, but the profiles are more or less similar. Near the hub, after the diffuser the $k-\omega$-SST model

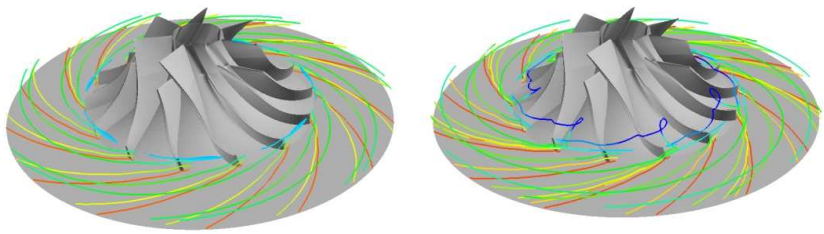

(a) (b)

Figure 4.37: Streamlines in the $b_{2'}/b_2 = 0.903(shroud)$ vaneless diffuser. The colder the color, the nearer to the shroud the streamline is. (a) $k-\epsilon$ and (b) $k-\omega$-SST.

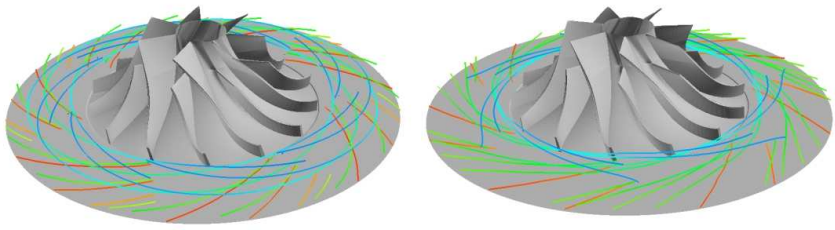

(a) (b)

Figure 4.38: Streamlines in the $b_{2'}/b_2 = 0.903$ vaneless diffuser. The colder the color, the nearer to the shroud the streamline is. (a) $k-\epsilon$ and (b) $k-\omega$-SST.

predicts higher radial velocity, and a thicker boundary layer. Near the shroud the differences are more evident. After the impeller, the $k-\omega$-SST model predicts that the flow is reversed. Also after the diffuser, the $k-\omega$-SST model predicts that the flow is reversed, and the velocity is smaller than after the impeller. The $k-\epsilon$ model does not predict reversed flow, neither before the

diffuser nor after it.

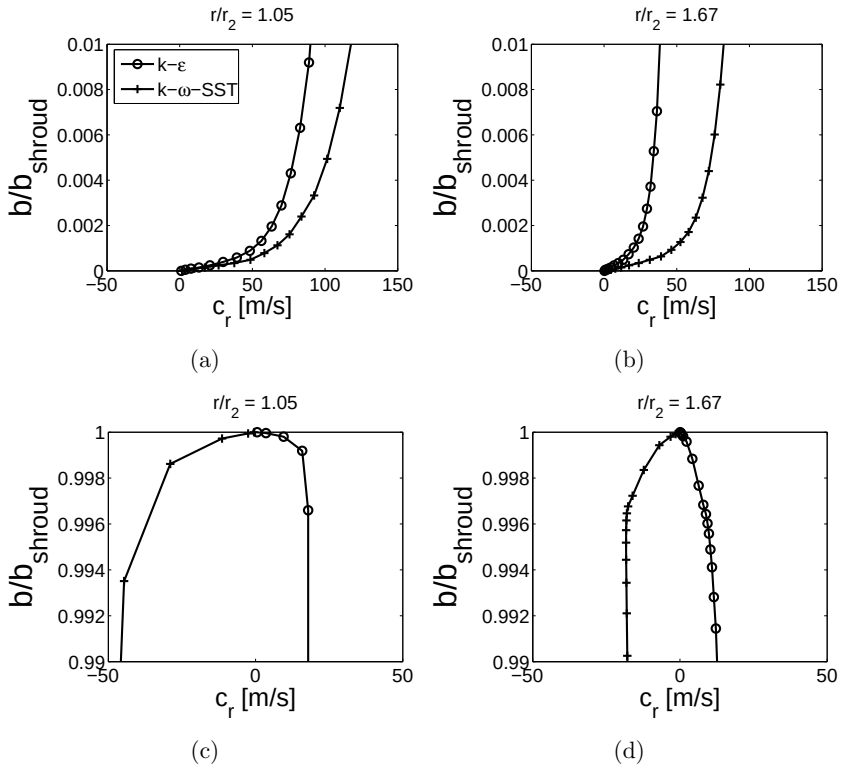

Figure 4.39: Radial velocity profiles in the unpinched vaneless diffuser (a) after the impeller, near the hub, (b) after the diffuser, near the hub, (c) after the impeller near the shroud, and (d) after the diffuser, near the shroud.

For the $b_{2'}/b_2 = 0.903$ vaneless diffuser (Fig. 4.40), the trend near the hub is similar to that of the unpinched case. There are no major differences in the velocity profiles after the impeller, near the hub. After the diffuser, near the hub, the $k - \omega$-SST model predicts higher radial velocity and a somewhat thicker boundary layer. Near the shroud, the $k - \epsilon$ turbulence model predicts that the flow is separated after the impeller, and after the diffuser, the $k - \epsilon$ model predicts the flow velocity to be near zero, but slighly on the positive side, so it seems that the boundary layer is reattached and the flow is not separated any more. Near the shroud, the $k - \omega$ model predicts a reversed flow before and after the diffuser.

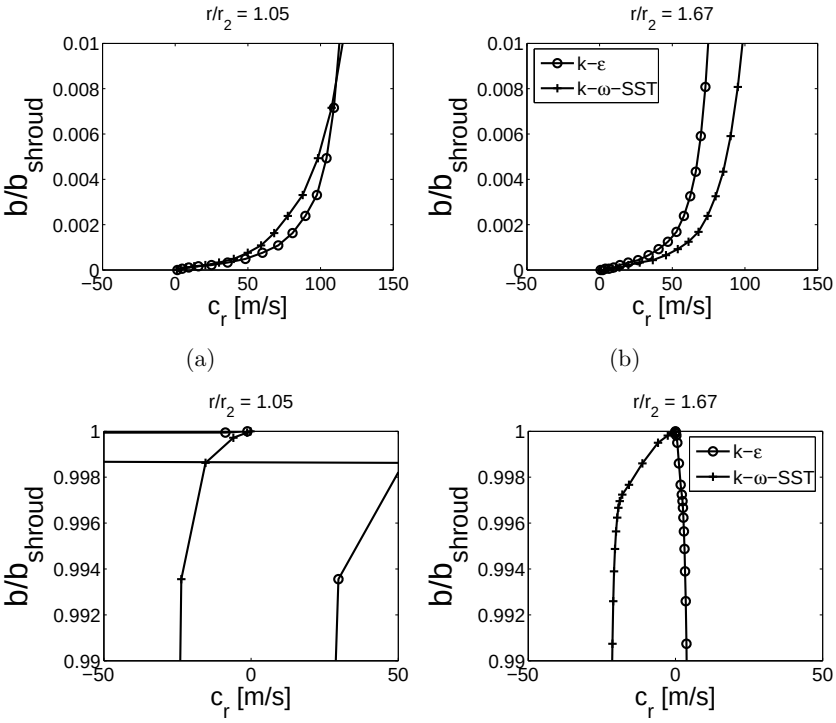

(a) (b)

(c) (d)

Figure 4.40: Radial velocity profiles in the $b_{2'}/b_2 = 0.903$ vaneless diffuser (a) after the impeller, near the hub, (b) after the diffuser, near the hub, (c) after the impeller near the shroud, and (d) after the diffuser, near the shroud.

For the $b_{2'}/b_2 = 0.903$ (shroud) vaneless diffuser (Fig. 4.41), near the hub, the velocity profiles are almost the same with both turbulence models. Unlike in the other cases, here the $k-\omega$-SST predicts slightly lower radial velocities. Near the shroud the trend is similar to that of the unpinched vaneless diffuser, the $k-\omega$-SST model predicts reversed flow, whilst the $k-\epsilon$ model does not.

The radial velocity distributions with both turbulence models, near the shroud and the hub, for the 15-vaned diffuser with the vane turning angle of 10° at the leading edge, in the middle of the passage, and at the trailing edge, are presented in Figures 4.42 and 4.43, respectively. Near the shroud, there

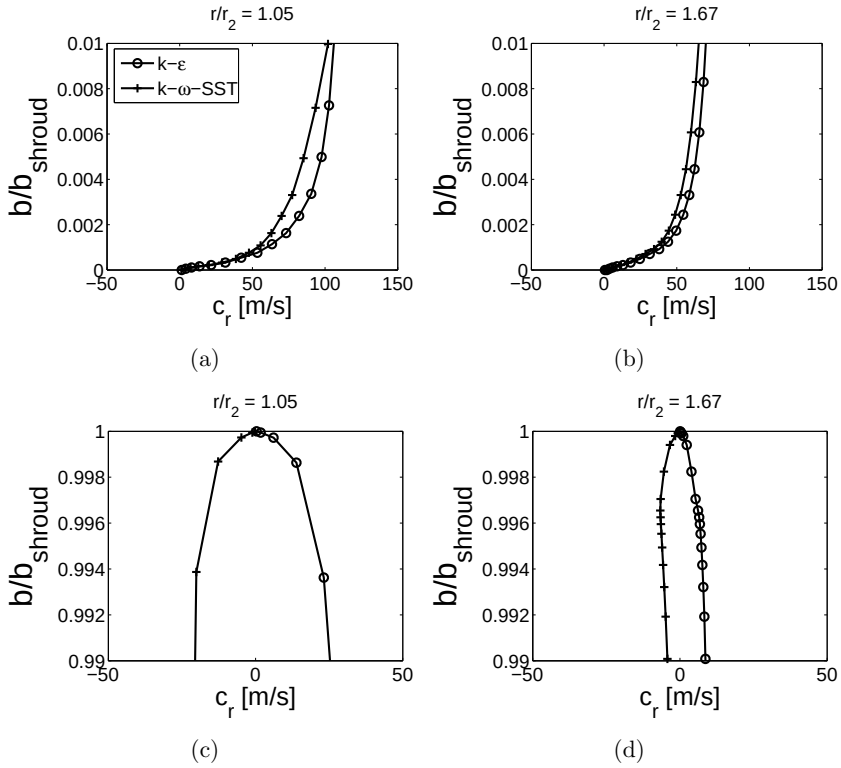

Figure 4.41: Radial velocity profiles in the $b_{2'}/b_2 = 0.903$ (shroud) vaneless diffuser (a) after the impeller, near the hub, (b) after the diffuser, near the hub, (c) after the impeller near the shroud, and (d) after the diffuser, near the shroud.

are only minor differences in the velocity profiles. At the leading edge and in the middle of passage, the $k - \omega$-SST turbulence model predicts slightly higher radial velocity. At the trailing edge there are no differences in the velocity profiles. Interestingly, near the hub, the $k - \omega$-SST model predicts somewhat slower radial velocities at the leading edge and in the middle of the passage. At the trailing edge there are no differences between the turbulence models.

Similar profiles near the shroud and the hub for the 17-vaned diffuser, with the vane turning angle of 10° are presented in Figures 4.44 and 4.45, respectively. Near the shroud, the profiles are similar between the turbulence

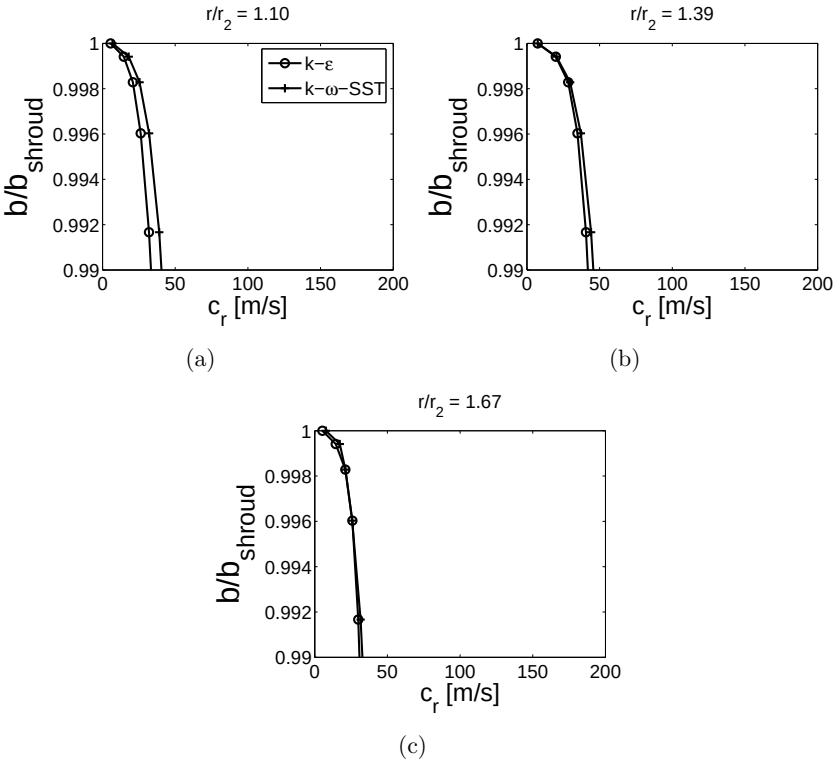

Figure 4.42: Radial velocity profiles near the shroud in the vane passage for the 15-vaned diffuser, with the vane turning angle of 10° (a) at the leading edge, (b) in the middle, and (c) at the trailing edge.

models, except at the leading edge, where the $k-\epsilon$ model predicts slightly lower radial velocities. Near the hub the turbulence models predict almost the same radial velocities at the leading and trailing edge. In the middle of the passage, the $k-\omega$-SST predicts somewhat lower radial velocities.

Radial velocity profiles with both turbulence models near the hub and shroud, for the 23-vaned diffuser with the vane turning angle of 20°, are presented in Figures 4.46 and 4.47, respectively. With this diffuser the differences between the two turbulence models are the largest. Near the shroud, the $k-\omega$-SST model predicts significantly lower radial velocities at the leading edge and in the middle of the passage. At the trailing edge the profiles are quite similar to each other. Also near the hub, at the leading edge and in the middle of

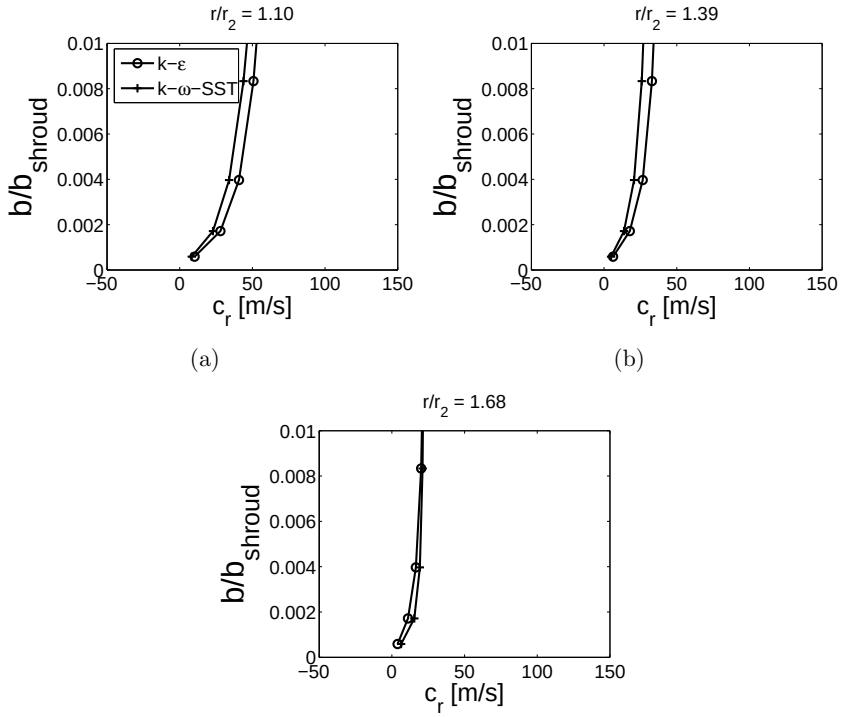

Figure 4.43: Radial velocity profiles near the hub in the vane passage for the 15-vaned diffuser, with the vane turning angle of 10° (a) at the leading edge, (b) in the middle, and (c) at the trailing edge.

the passage, the $k-\omega$-SST model predicts clearly lower radial velocities. At the trailing edge, the $k-\omega$ turbulence model predicts the flow to separate, whilst the $k-\epsilon$ does not.

Radial velocity contours in the diffuser vane passage for the 15-vaned diffuser, with both turbulence models, are presented in Figure 4.48. There are some differences in the contours, between the two turbulence models. The $k-\epsilon$ model predicts somewhat higher radial velocities. The high velocity areas are larger at the leading edge near the pressure side, in the middle of passage (in the stream direction) and at the trailing edge near the suction side. The $k-\omega$-SST model predicts slightly larger slow velocity areas, especially at the trailing edge near the suction side. The differences between the

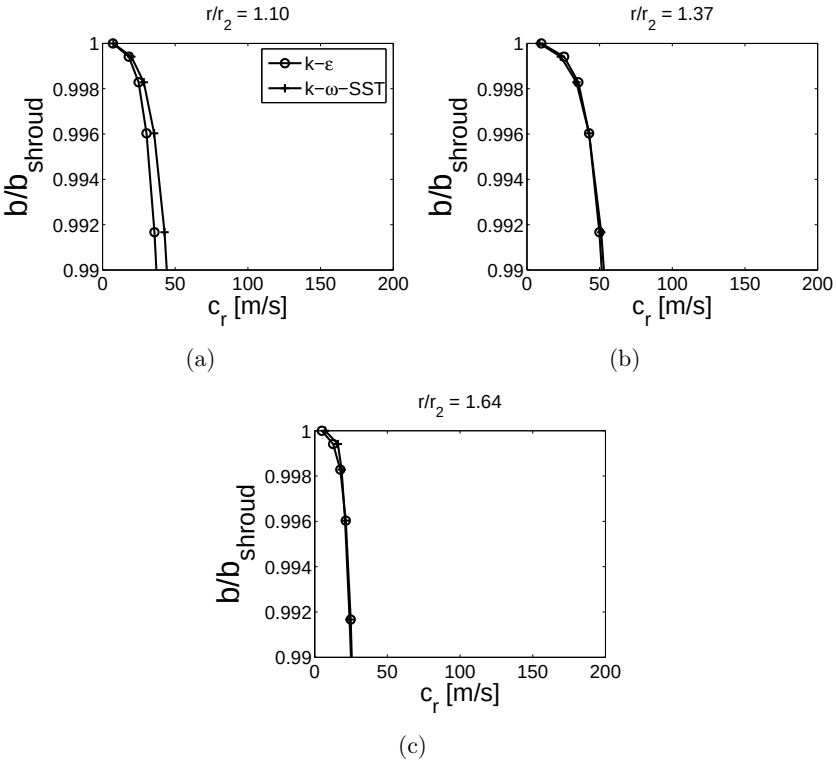

Figure 4.44: Radial velocity profiles near the shroud in the vane passage for the 17-vaned diffuser, with the vane turning angle of 10° (a) at the leading edge, (b) in the middle, and (c) at the trailing edge.

turbulence models are similar with the 17-vaned diffuser (Figure 4.49). With both diffusers the high velocity area is near the pressure side at the leading edge, and near the suction side at the trailing edge. This applies with both turbulence models.

Radial velocity contours in the 23-vaned diffuser with the vane turning angle of 20°, with both turbulence models, are presented in Figure 4.50. Here the differences between the two turbulence models are more evident. The $k-\epsilon$ turbulence model predicts larger radial velocity area at the leading edge, and the area is located near hub at the pressure side. In the middle of passage, the $k-\epsilon$ model predicts the high radial velocity area to be near the suction side, and the maximum to be nearer to the hub. At the trailing edge,

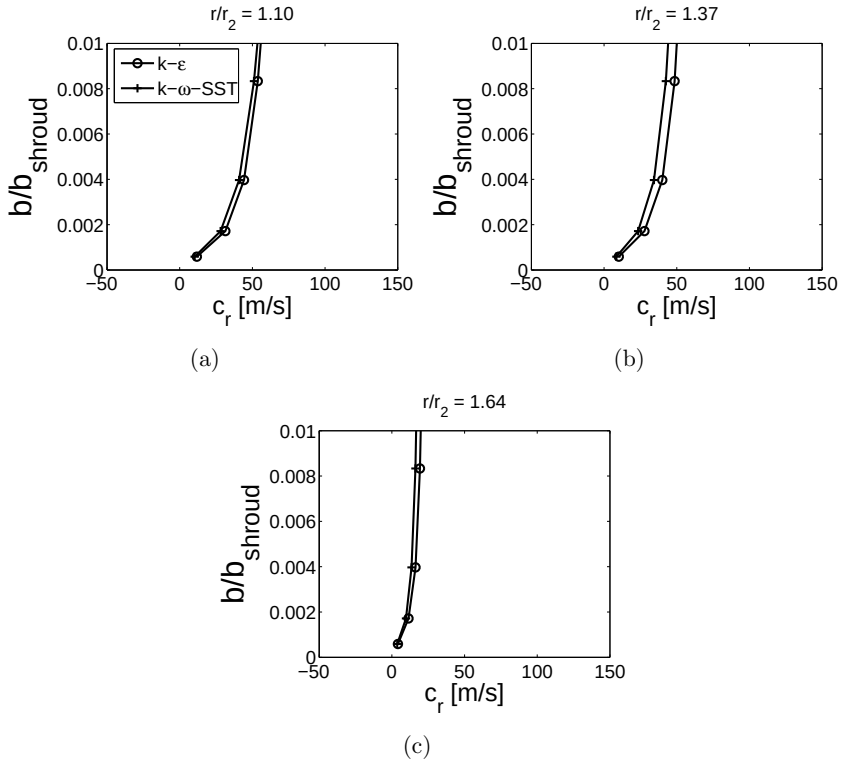

Figure 4.45: Radial velocity profiles near the hub in the vane passage for the 17-vaned diffuser, with the vane turning angle of 10° (a) at the leading edge, (b) in the middle, and (c) at the trailing edge.

the large velocity area is located in the middle of passage, slight peak being nearer to the suction side, and there are slow velocity areas at each corner of the passage. The $k-\omega$-SST model predicts smaller high velocity are at the leading edge. In the middle of the passage, the $k-\omega$-SST model predicts the high velocity area to be near the pressure side, and the peak radial velocity is lower than with the $k-\epsilon$ model. There is a small separated area at the hub near the suction side. At the trailing edge, the peak velocity area is near the pressure side shroud corner, and the peak velocity is higher than with the $k-\epsilon$. The separated area is increased extending for more than half the channel width (in circumferential direction) at the hub.

In general, the $k-\omega$-SST model predicts the flow to be more complex, and

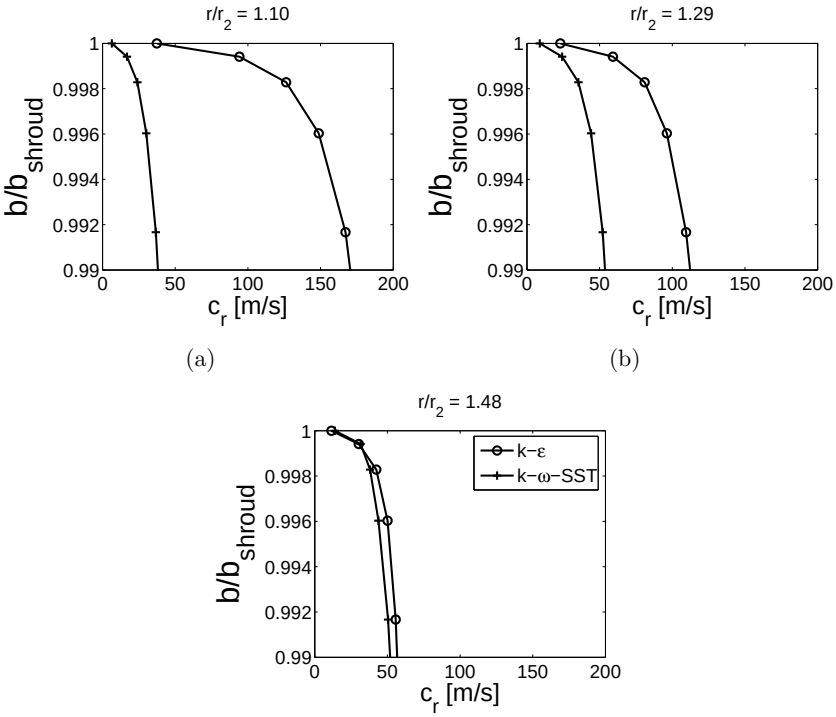

Figure 4.46: Radial velocity profiles near the shroud in the vane passage for the 23-vaned diffuser, with the vane turning angle of 20° (a) at the leading edge, (b) in the middle, and (c) at the trailing edge.

that there are backflow areas near the shroud. For the vaneless diffusers, the $k-\omega$-SST turbulence model predicts that there is a backflow region near the shroud, which extends all the way to the diffuser exit. Also for the 23-vaned diffuser with the vane turning angle of 20° at the trailing edge, the $k-\omega$-SST model indicats that the flow is separated near the hub. These results seem reasonable, bearing in mind that in general, the $k-\omega$ models are better in decelerating flows and when there is an adverse pressure gradient (Wilcox, 1998). Both these conditions are found in the diffuser. The matter of which turbulence model predicts the flow better, will be discussed below in chapter 5, when the measurement results are compared to numerical results.

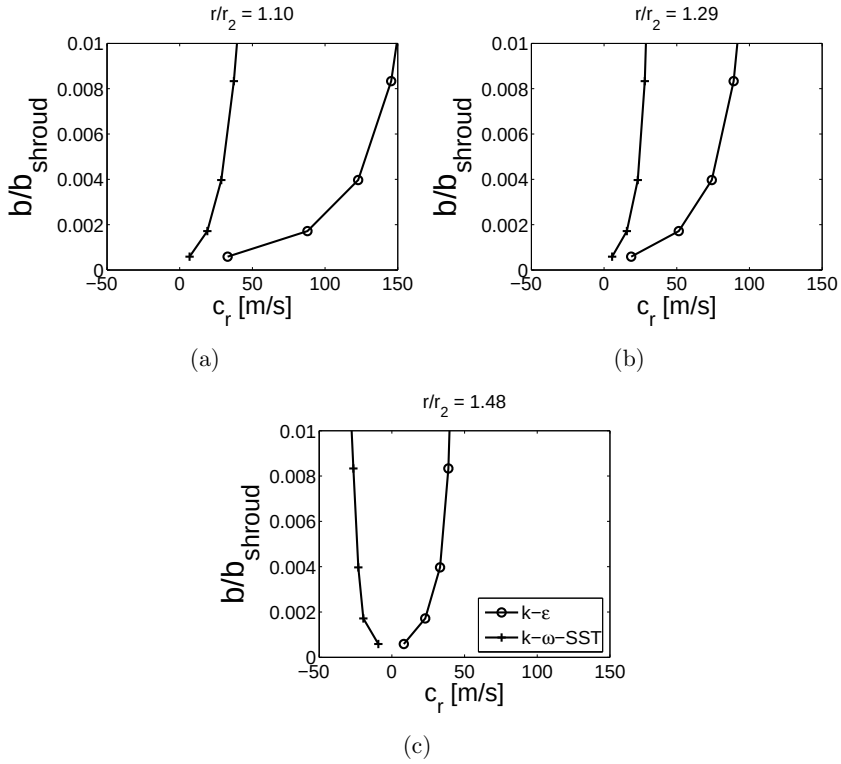

Figure 4.47: Radial velocity profiles near the hub in the vane passage for the 23-vaned diffuser, with the vane turning angle of 20° (a) at the leading edge, (b) in the middle, and (c) at the trailing edge.

4.6 Conclusions

The $k - \epsilon$ turbulence model predicts that the implementation of the pinch weakens both the impeller and stage isentropic efficiencies. Also the impeller and stage total-to-static pressure ratios are worse for the pinched geometries. The total pressure loss coefficients are higher and the static pressure rise coefficients lower for the pinched geometries. There are no major differences between the different pinches in the velocity or angle profiles before the diffuser. After the diffuser, there are no major differences in the velocity and angle profiles between the different pinched cases. It seems that just adding the pinch has more effect on the flow field than the actual amount of pinch.

It seems, however, according to the $k - \omega$-SST turbulence model, that it

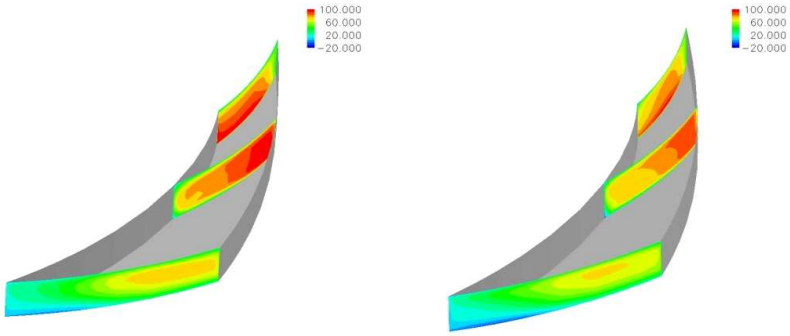

(a) (b)

Figure 4.48: Radial velocity contours in the diffuser vane passage, 15-vaned diffuser, (a) $k - \epsilon$, and (b) $k - \omega$-SST.

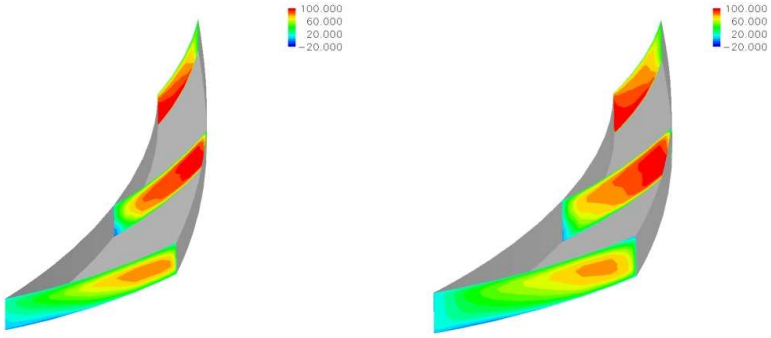

(a) (b)

Figure 4.49: Radial velocity contours in the diffuser vane passage, 17-vaned diffuser, (a) $k - \epsilon$, and (b) $k - \omega$-SST.

would be possible to improve the preformance of a centrifugal compressor with pinch. The impeller efficiencies are better for the two geometries with most pinch at the shroud wall. The geometry $b_{2'}/b_2 = 0.903$ (shroud) has 4 percentage points and the geometry $b_{2'}/b_2 = 0.806$ 1 percentage point better impeller efficiency than the unpinched geometry. All pinched geometries have better stage efficiency than the unpinched, except for the $b_{2'}/b_2 = 0.903$ (hub & shroud). The impeller total-to-static pressure ratios are slightly higher

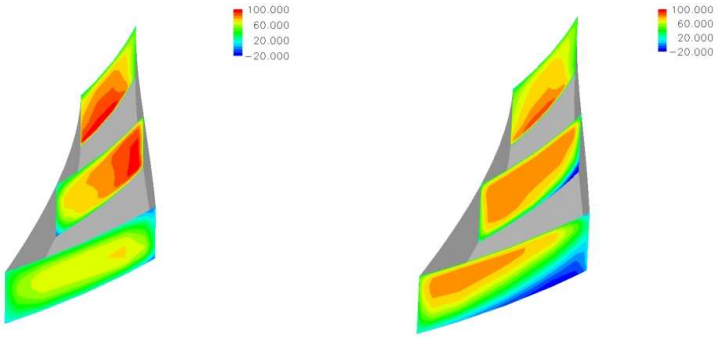

(a) (b)

Figure 4.50: Radial velocity contours in the diffuser vane passage, 23-vaned diffuser, vane turning angle 20°, (a) $k - \epsilon$, and (b) $k - \omega$-SST.

and the stage total-to-static pressure ratios lower for the pinched geometries than for the unpinched geometry. The total pressure loss coefficients are somewhat lower for the pinched geometries, except for the $b_{2'}/b_2 = 0.903$ (hub & shroud). The static pressure rise coefficients are lower for all pinched geometries, except for the $b_{2'}/b_2 = 0.903$ (shroud). The pressure losses and the pressure rises should be lower because of the shorter flow path in the pinched diffuser.

Considering the flow angle and velocity profiles, the benefits of sufficient pinch are clearly seen. The pinch, if sufficient, removes the backflow regions near the shroud, which should lead to higher efficiencies. Also the pinch makes the tangential relative velocities over the tip clearance smaller, leading to lower secondary flows and losses and to more a uniform flow field. However, it seems that too small pinch might be extremely harmful for the performance of the diffuser itself. All in all, it seems that the two cases with the most pinch at the shroud, the $b_{2'}/b_2 = 0.903$ (shroud) and the $b_{2'}/b_2 = 0.806$ (hub and shroud), are the two best geometries. This might suggest that pinch implemented to the shroud wall is more beneficial than pinch implemented at the hub wall. It should be noted that it seems that complete grid undependency was not achieved in the diffuser, and in the future more consideration should be given to the diffuser grid.

The vaned diffuser results with the $k - \epsilon$ turbulence model indicate that

all the cases with the vaned diffuser have slighlty better impeller efficiency than the unpinched vaneless one, but only three of them have better stage efficiency (n15,θ10, n23,θ15 and n15,θ20). The $k-\omega$-SST turbulence model predicts all the vaned diffusers to have the same or almost the same impeller efficiency and better stage efficiency than the unpinched vaneless geometry. For the total-to-static pressure ratios, the $k-\epsilon$ model predicts all the geometries to have the same or worse impeller pressure ratio and worse stage pressure ratio. The $k-\omega$-SST model predicts all the geometries to have better impeller pressure ratios but worse stage pressure ratios, except for the n15,θ10, which has also a better stage pressure ratio. The $k-\epsilon$ model predicts all the vaned diffusers to have higher loss coefficients. Also the pressure rise coefficients are higher, except for the n17,θ10 and n19,θ10, which have slightly lower pressure rise coefficients. The $k-\omega$-SST model predicts that all the vaned geometries have lower pressure loss and higher pressure rise coefficients.

The number of vanes, the vane turning angle or the turbulence model have only a minor effect or no effect at all on the angle or velocity profiles before the diffuser. After the diffuser, it seems that more vanes means more tangential flow. This is most likely due to the shorter vane length. The absolute flow velocity and its tangential components are highest for the diffuser with the most vanes, and decreasing the vane number decreases both. The effect of vane number to radial velocity is not so straightforward, because when the vane number is the lowest, the flow velocity is the slowest and the flow angle largest, and when the vane number is the highest, the flow velocity is the fastest and the flow angle smallest. The radial velocity is calculated with the velocity and the flow angle. The effect of velocity is linear, and the effect of the flow angle is non-linear. Increasing the vane turning angle makes the flow more radial. Also increasing the turning angle decreases the absolute and tangential velocities after the impeller. The effect of the vane turning angle towards radial velocity after the diffuser is minor according to $k-\epsilon$ model. In general, the effect of the turbulence model on the angle and velocity distributions is minor. The only significant difference, which is a major one, is that for the n23,θ20 the $k-\omega$-SST model predicts flow separation at the hub. In general, the vaned diffuser with least vanes (15) and the one with most vanes (23) are the two best geometries. In terms of vane turning angle, a greater turning angle seems to be better, until separation occurs. In this case 15° would be the best case. The vaned diffuser simulations should probably have had more cells, to gain more accurate results.

5 Measurements

The centrifugal compressor measurement station in the laboratory of Fluid Dynamics at LUT complies with the standards ISO 5167 Measurement of Fluid Flow by Means of Pressure Differential Devices Inserted in Circular Cross Section Conduits Running Full, and ISO 5389 Turbocompressors - Performance Test Code (ISO, 2003, 2005). A schematic view of the test station is presented in Figure 5.1.

The compressor used in the measurements (Figure 5.2) is designed to be used in the waste water treatment process. It has a design total-to-total stage pressure ratio $\pi_{\mathrm{tt},1-5}$ of 1.78. During the measurements, when a different diffuser was installed the axial, clearance between the impeller and casing was measured to ensure that the tip clearance stayed constant for each construction.

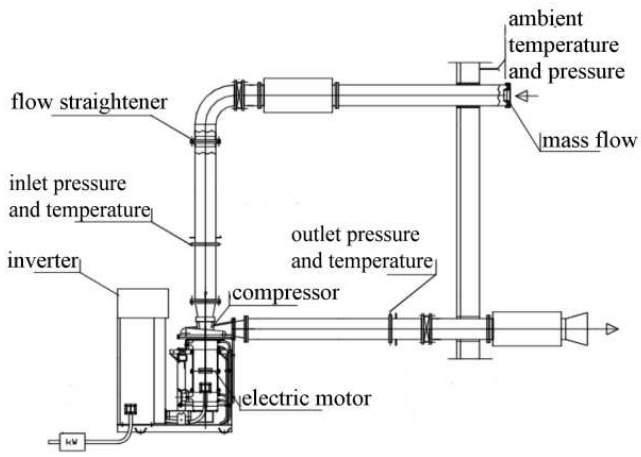

Figure 5.1: Schematics of the centrifugal compressor test station at LUT. Figure by Laboratory of Fluid Dynamics/LUT.

5.1 Measurement procedure

5.1.1 Overall compressor performance measurements

In the compressor overall performance measurements, the compressor was insulated to achieve better accuracy. For each geometry, the measurements

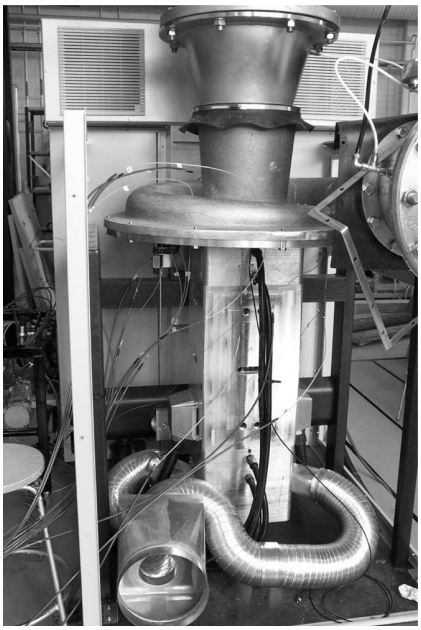

Figure 5.2: Compressor used in the measurements. Photo courtesy of Teemu Turunen-Saaresti/LUT.

began at the lowest rotational speed, and after a given rotational speed curve was measured, the rotational speed was increased. For a given rotational speed, the measurements began at the choke. At the choke, when throttling the valve only increased the pressure ratio but did not affect the mass flow, the compressor ran approximately 15 minutes for each point before the point was recored. When throttling the valve caused the mass flow to decrease, the compressor was left to run approximately 30 minutes, before a point was recorded. This was then repeated until the stall line was reached. In total of 5-13 different mass flow points were measured for each rotational speed. For the highest rotational speeds at choke and near choke mass flows, the limiting factor was the cooling of the electric motor running the compressor, so these points were not measured or they were measured sooner. The maximum relative measurement uncertainties for the mass flow, efficiency and pressure ratio in the operating map measurements with the 95.4% confidence interval were:

$$\begin{aligned} E_{\mathrm{q_m},95.4} &= \pm 0.48\% \\ E_{\eta,95.4} &= \pm 1.34\% \\ E_{\pi,95.4} &= \pm 0.93\% \end{aligned} \tag{5.1}$$

The calculation procedure for the measurement uncertainty is given in Appendix A. These uncertainties were also applied in the flow field measurements when the mass flow, the efficiency or the pressure ratio were considered.

5.1.2 Flow field measurements

The location of the static pressure taps and probe traverses are presented in Figure 5.3. A three-holed cobra-probe was used to measure the flow angle and total pressure before ($r_{2^*}/r_2 = 1.036$) and after the diffuser ($r_4/r_2 = 1.67$). The cobra-probe was first calibrated and nulled using free jet flow. In the nulling process, the probe and the traversion device were set so that the flow angle showed 0° when the pressure difference between the farthest holes were zero. The circumferential location for the cobra-probe was 194°. Three different Kiel probes were used to measure the total pressure, and along with each Kiel probe a thermocouple was also fitted so that the total temperature was also measured. The Kiel probes were fitted at the same radii as the cobra-probe, and the circumferential locations for the Kiel probes were 14°, 104° and 284°.

Static pressures before and after the diffuser were measured at the same radii as the total pressure and flow angle. Four different circumferential locations (0°, 90°, 180°, and 270°) were used. At the circumferential location of 180° the static pressure was also measured at radii $r/r_2 = 1.1$, 1.26 and 1.47.

The flow fields were measured using the design rotational speed and three different mass flows. For the vaneless diffusers, the mass flows were: the design flow, $0.58 \times q_{\mathrm{m,des}}$ and $1.38 \times q_{\mathrm{m,des}}$. For the vaned diffuser, the mass flows were: the design flow, $0.65 \times q_{\mathrm{m,des}}$ and $1.20 \times q_{\mathrm{m,des}}$.

The probe traverse holes and the static pressure taps were originally designed to measure the flow field in a vaneless diffuser. This led to problems when the vaned diffusers were measured. For example one of the Kiel probes (Kiel no. 2 at 284°) could not be fitted when the n15,θ10 diffuser was measured, simply because one of the vanes blocked the traverse hole. Also some of the

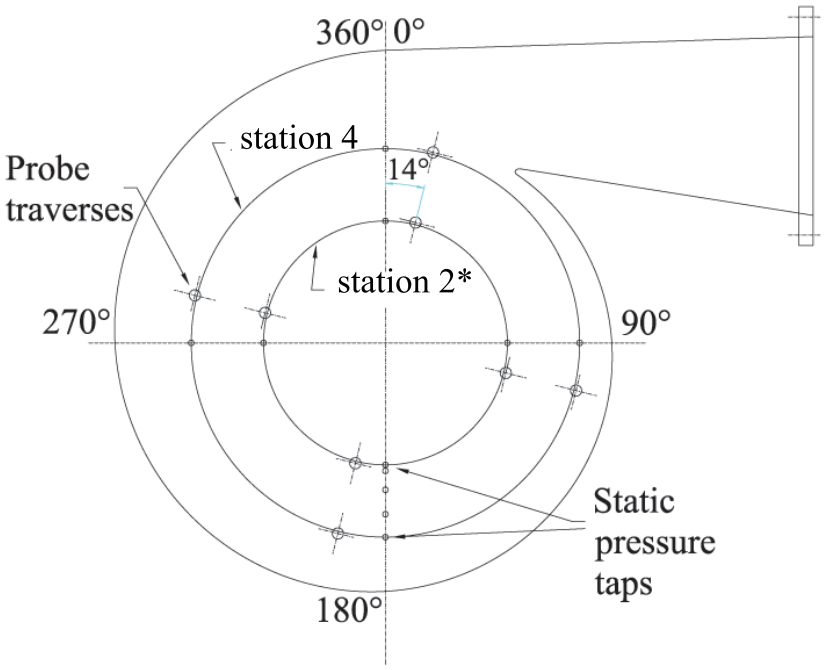

Figure 5.3: Location of static pressure taps and probe traverses. Figure courtesy of Teemu Turunen-Saaresti/LUT

static pressure taps were close to the vanes. A detail of the problem is presented in Figure 5.4.

Maximum relative uncertainties with the 95.4 % confidence interval in the flow field measurements for the flow velocity, the flow angle, the radial and the tangential components of the velocity and the static pressures were:

$$\begin{aligned} E_{\mathrm{c}} &= \pm 5.4\% \\ E_{\alpha} &= \pm 1.4\% \\ E_{\mathrm{c_r}} &= \pm 5.5\% \\ E_{\mathrm{c_t}} &= \pm 5.5\% \\ E_{\mathrm{p}} &= \pm 0.25\% \end{aligned} \tag{5.2}$$

The calculation procedure is explained in Appendix A.

Figure 5.4: Details of the static pressure taps in the diffuser and cobra probe traverse location after the diffuser.

5.2 Measured cases

All the five vaneless diffusers discussed in the previous chapter were measured. Details of the measured vaneless geometries are presented in Table 5.1, and an example of a shroud plate is presented in Fig 5.5.

Table 5.1: Measured vaneless geometries

Case	$b_{2'}/b_2$	$r_{2'}/r_2$	$b_{2'}/r_2$	r_4/r_2	pinch
1	1.000	1.00	0.1217	1.68	unpinched
2	0.903	1.01	0.1098	1.68	hub & shroud
3	0.854	1.01	0.1039	1.68	hub & shroud
4	0.806	1.01	0.0979	1.68	hub & shroud
5	0.903	1.01	0.1098	1.68	shroud

On the basis of the numerical results, three of the six vaned diffusers were chosen for measurements: n15,θ10, n23,θ10 and n23,θ15. Details of the measured vaned diffusers are presented in Table 5.2. These were chosen because the geometries with the most and the least vanes seemed to be the best, according to the CFD results. The geometry with the most vane turning was not chosen because it seemed, according to the CFD results, that the flow separated in the diffuser. All the vaned diffusers are presented in Fig. 5.6.

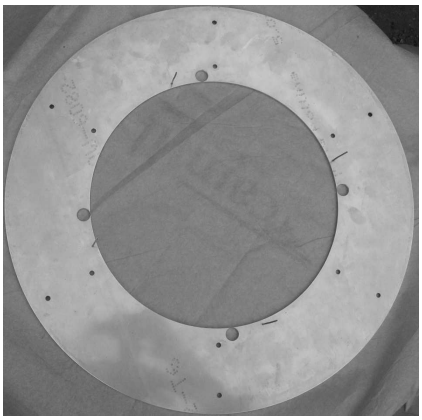

Figure 5.5: Photo of a shroud plate for the diffuser measurements. Photo taken from above so the flow is on the underside of the plate.

Table 5.2: Measured vaned diffuser geometries.

Case	N	$\theta[°]$	σ	$r_{2'}/r_2$	r_3/r_2	r_4/r_2
n15,θ10	15	10	2.65	1.10	1.68	1.68
n23,θ10	23	10	2.76	1.10	1.48	1.68
n23,θ15	23	15	2.56	1.10	1.48	1.68

5.3 Measurement results

Two of the vaneless geometries, unpinched and $b_{2'}/b_2 = 0.854$, were measured, and some of the results were published by Turunen-Saaresti (2004). Some of the measurement results are presented here to the keep the logic and continuation of this work intact. Selected measurement results of all the vaneless diffusers are also presented in Turunen-Saaresti et al. (2009).

5.3.1 Overall compressor performance

The measurement station intakes atmospheric air. Obviously the atmospheric conditions vary during the measurements, so the measured values must be converted to the corresponding reference values. This ensures that the performance measurements done under different conditions are comparable with each other. The conversion to reference values is done with applying

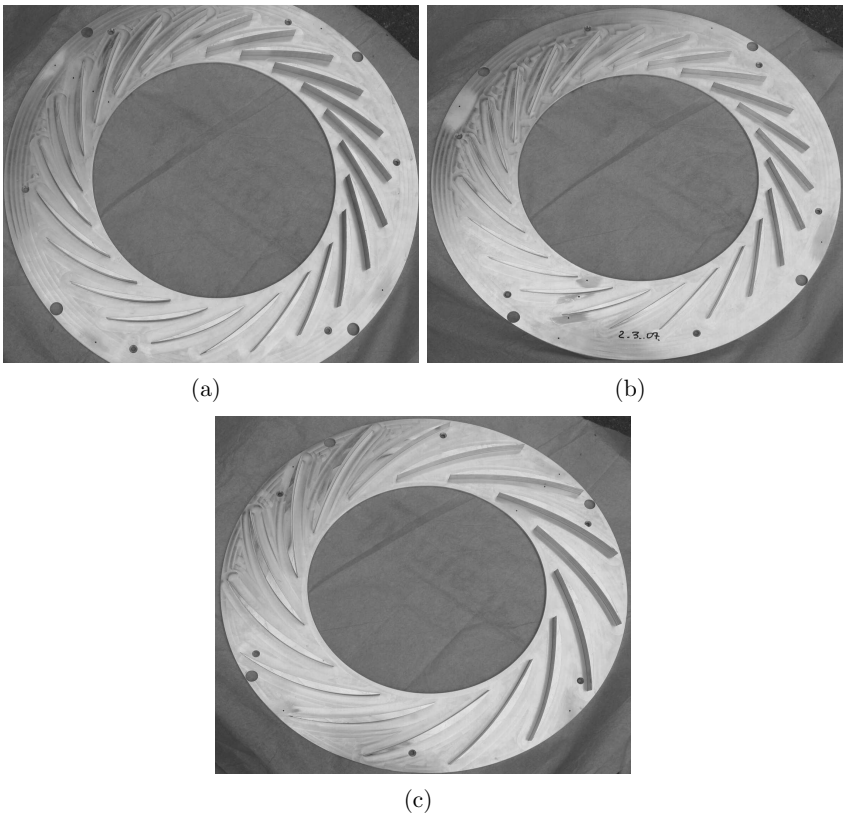

(a) (b)

(c)

Figure 5.6: Photos of different measured vaned diffusers. (a) n23,θ10, (b) n23,θ15 and (c) n15,θ10.

the reference total pressure $p_{\mathrm{t1,ref}} = 101.3$ kPa, the reference total temperature $T_{\mathrm{t1,ref}} = 288$ K, and the reference relative humidity $R_{\mathrm{H}} = 60\%$. The reference relative humidity is used to calculate the specific gas constant R. The above-mentioned reference values are then used to calculate the reference mass flow $q_{\mathrm{m,ref}}$ and the reference rotational speed N_{N}, which are are calculated as

$$q_{\mathrm{m,ref}} = q_{\mathrm{m}} \frac{p_{\mathrm{t1,ref}}}{p_{\mathrm{t1}}} \sqrt{\frac{T_{\mathrm{t1}} R}{T_{\mathrm{t1,ref}} R_{\mathrm{ref}}}} \tag{5.3}$$

$$N_{\mathrm{ref}} = N \sqrt{\frac{T_{\mathrm{t1,ref}} R_{\mathrm{ref}}}{T_{\mathrm{t1}} R}} \tag{5.4}$$

where the subscript ref denotes a given reference value and the values without the subscript ref are the actual measured values. When the results are processed, in total eight measurements are taken for a given operating point, and the average value of the measurements are given as a single operating point. Eight consecutive measurement corresponds to two minutes of compressor running time.

Compressor operating maps for the vaneless constructions are presented in Figures 5.7, 5.9, 5.8, 5.10 and 5.11. The operating maps are non-dimensionalised by dividing the efficiencies with the design efficiency of the unpinched vaneless geometry. Also the rotational speeds are divided with the design rotational speed, and the mass flows are divided with the design mass flow of the original geometry.

All the pinched cases had approximately 2 percentage points units higher peak efficiency than the unpinched geometry. Also the peak efficiency area was located around the design operating point with the pinched geometry, whereas with unpinched geometry the peak efficiency was reached only with lower rotational speeds and mass flows than the design rotational speed and the design mass flow. Comparing the efficiency at the design point, it is up to 4 percentage points higher with the pinched geometries. Pinch has only minor effect on the operating range, making it slightly narrower near the stall. When comparing different pinches with each other, it seems that there are no major differences between them. The cases with most pinch at the shroud ($b_{2'}/b_2 = 0.806$ and $b_{2'}/b_2 = 0.903$ (shroud)), have slightly wider peak efficiency area than the other two.

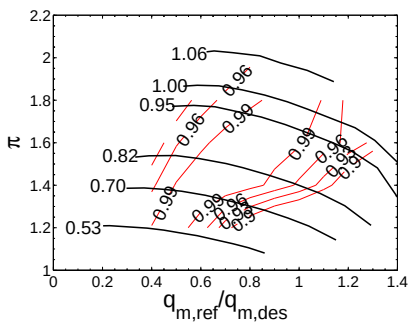

Figure 5.7: Operating map for the vaneless $b_{2'}/b_2 = 1.00$ construction

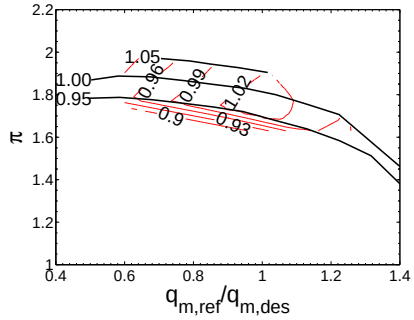

Figure 5.8: Operating map for the vaneless $b_{2'}/b_2 = 0.903$ construction

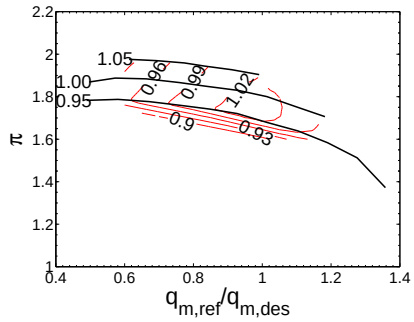

Figure 5.9: Operating map for the vaneless $b_{2'}/b_2 = 0.854$ construction

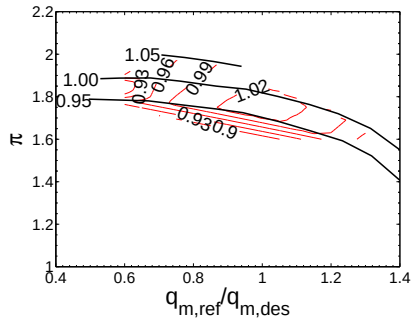

Figure 5.10: Operating map for the vaneless $b_{2'}/b_2 = 0.806$ construction

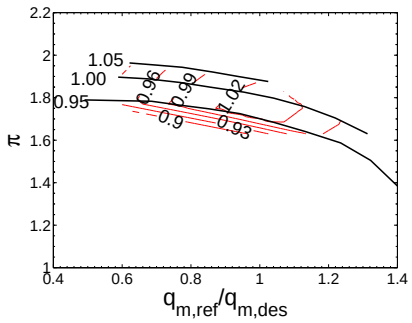

Figure 5.11: Operating map for the vaneless $b_{2'}/b_2 = 0.903$ (shroud) construction

Operating maps for the vaned diffusers are presented in Figures 5.12, 5.13 and 5.14. Two of the vaned geometries (n15,θ10 and n23,θ10) had approximately 2% units higher peak efficiency than the vaneless unpinched geometry. The third diffuser had the same peak efficiency. All the peak efficiencies were attained at higher rotational speeds than with the unpinched geometry. Also the peak efficiency shifted marginally to lower mass flows than the design mass flow. The width of the peak efficiency area is roughly the same for the vaned diffusers as it was for the vaneless diffusers. The vaned diffusers have notably narrower operating range. The stall lines have moved toward higher mass flows, indicating that the diffuser is the first to stall. Also the vaned diffuser choke is clearly visible in the operating maps. At a specific mass flow point for each rotational speed, the pressure rise plunges if the throttle valve is opened more. The mass flow does not increase after that point.

The isentropic total-to-total efficiencies over the whole stage at three different rotational speeds as a function of the mass flow for the vaneless geometries are presented in Figure 5.15, and the total-to-total stage pressure ratios in Figure 5.16. Considering the design and the lower rotational speeds, near the design mass flow all the pinched geometries have higher efficiency than the unpinched geometry. At lower mass flows there are no major differences between any vaneless geometries. At higher mass flows and at design rotational speed the $b_{2'}/b_2 = 0.854$ and at lower than design operating speed, the $b_{2'}/b_2 = 0.903$ (hub & shroud) seems to have slightly lower efficiency than the unpinched geometry. At a higher rotational speed, all the pinched geometries have higher efficiency than the unpinched geometry over the whole measured range. All in all, there are no major differences between the pinches. It

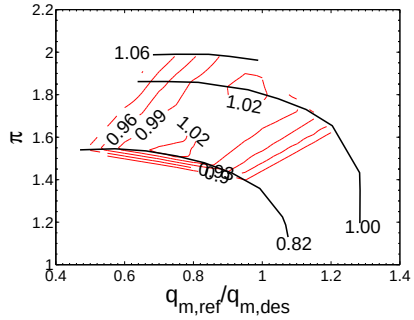

Figure 5.12: Operating map for the vaned diffuser n15,θ10

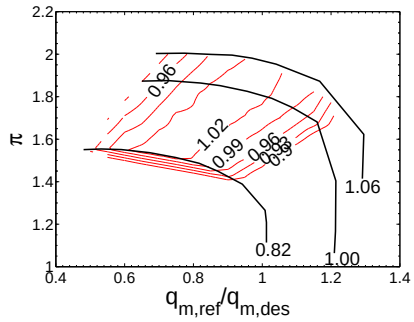

Figure 5.13: Operating map for the vaned diffuser n23,θ10

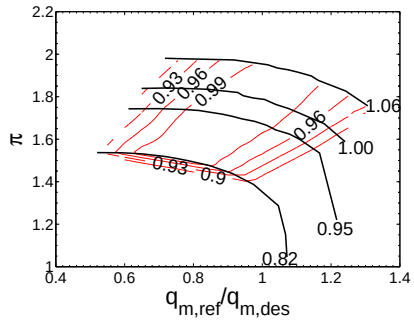

Figure 5.14: Operating map for the vaned diffuser n23,θ15

also seems that for the design and the lower rotational speeds, the peak

efficiency of the unpinched geometry is attained at lower mass flows than for the pinched geometries. At the design and lower rotational speeds, the total-to-total pressure ratios of different geometries behave similarly as the efficiencies. At the higher rotational speed, the unpinched geometry has the highest pressure ratio.

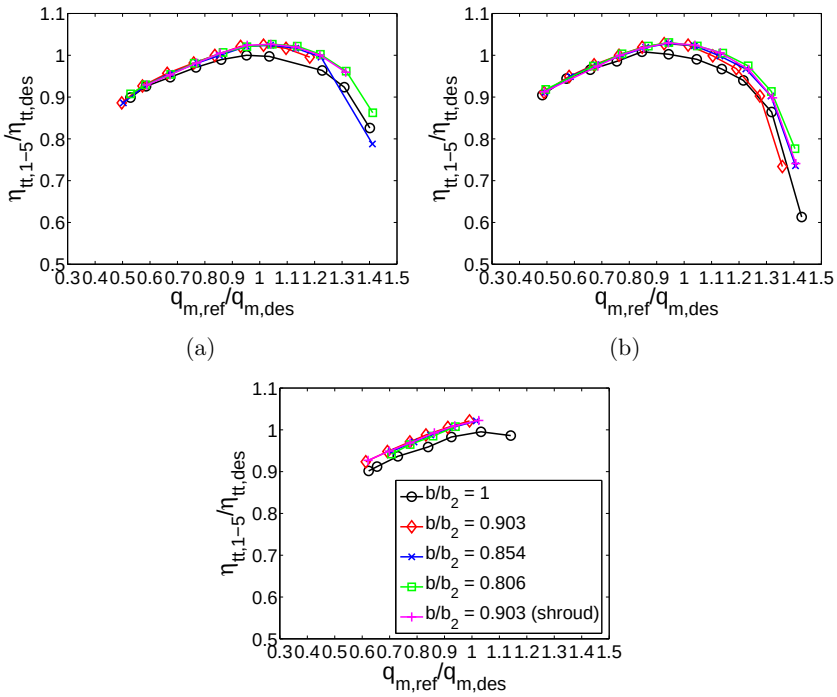

Figure 5.15: Isentropic total-to-total stage efficiencies of the vaneless geometries. (a) $N/N_{\mathrm{des}} = 1.00$, (b) $N/N_{\mathrm{des}} = 0.95$ and (c) $N/N_{\mathrm{des}} = 1.05$.

The isentropic total-to-total stage efficiencies and total-to-total pressure ratios for the vaned diffusers are presented in Figures 5.17 and 5.18, respectively. The peak efficiency is higher for the vaned diffusers at the design and at higher flows than for the unpinched vaneless diffuser. The peak efficiencies of the vaned diffusers are located at slightly lower mass flows than for the vaneless unpinched diffuser. At lower mass flows, there are no major differences between the vaned and vaneless unpinched diffusers. The pressure ratio is higher for the vaned diffusers at the design and at lower rotational

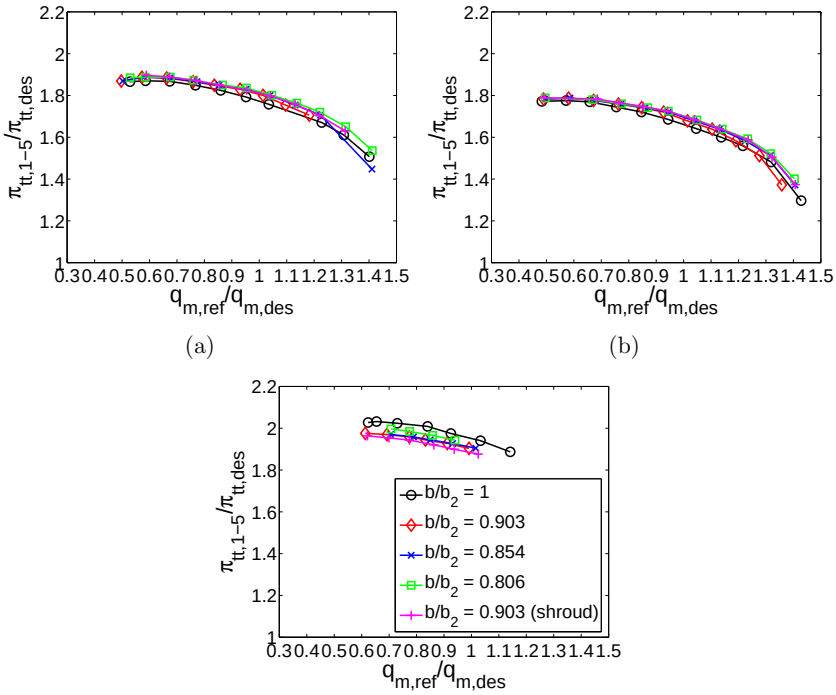

Figure 5.16: Total-to-total stage pressure ratio of the vaneless geometries. (a) $N/N_{\text{des}} = 1.00$, (b) $N/N_{\text{des}} = 0.95$ and (c) $N/N_{\text{des}} = 1.05$.

speeds and somewhat lower at the higher rotational speed.

5.3.2 Impeller, diffuser and volute performance

To establish some idea of how each component is affected by either the pinch or the vaned diffuser, the isentropic total-to-static efficiency, the total-to-static pressure ratio, the total pressure loss, and the static pressure rise coefficients are presented for each component. For the impeller, the efficiency and the pressure ratio are calculated from inlet to the measurement plane after the impeller. For the diffuser, they are calculated from inlet to the diffuser exit, so it is combined impeller and diffuser performance. The pressure coefficients are calculated from impeller exit to diffuser exit, from diffuser inlet to the compressor exit cone outlet, and from impeller exit to the com-

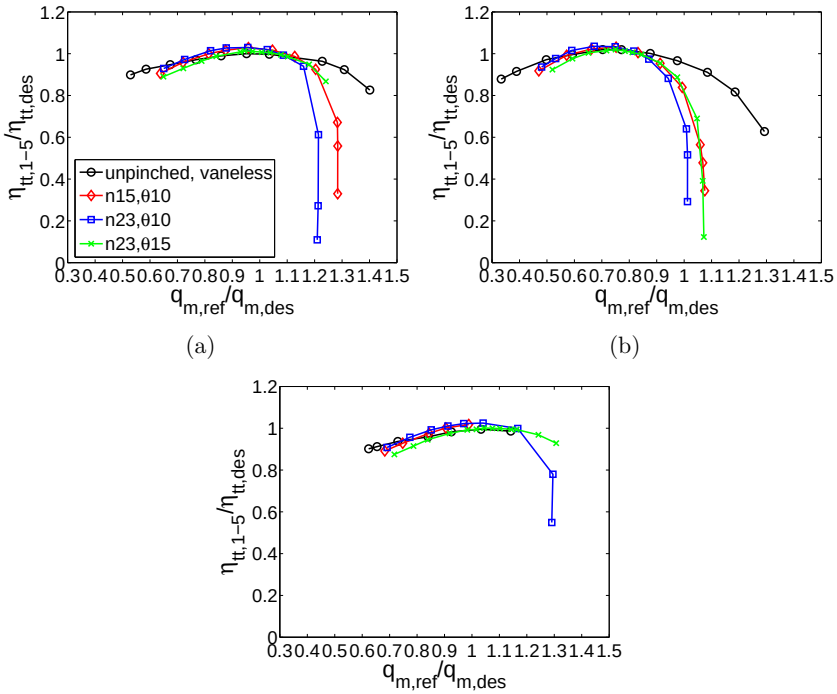

Figure 5.17: Isentropic total-to-total stage efficiencies of the of the vaned geometries. (a) $N/N_{\text{des}} = 1.00$, (b) $N/N_{\text{des}} = 0.82$ and (c) $N/N_{\text{des}} = 1.06$.

pressor exit cone outlet. All these performance values are calculated from the flow field measurements, so they are at the design operating speed, and similarly to the CFD results, the measurement results are also compared to the respective vaneless unpinched values.

The vaneless diffuser impeller and combined impeller and diffuser efficiencies are presented in Figure 5.19. The geometry with the least pinch seems to have lower impeller efficiency at the low mass flow, and at the design flow it has approximately the same impeller efficiency as the unpinched case. All other pinched cases have higher impeller efficiency than the unpinched one with all mass flows, except for the case with most pinch at high mass flow, where it has the same efficiency as the unpinched one. For the low and design flows the case with only the shroud pinch has the highest impeller efficiency, the case with $b_{2'}/b_2 = 0.854$ has the second highest, and the case with least

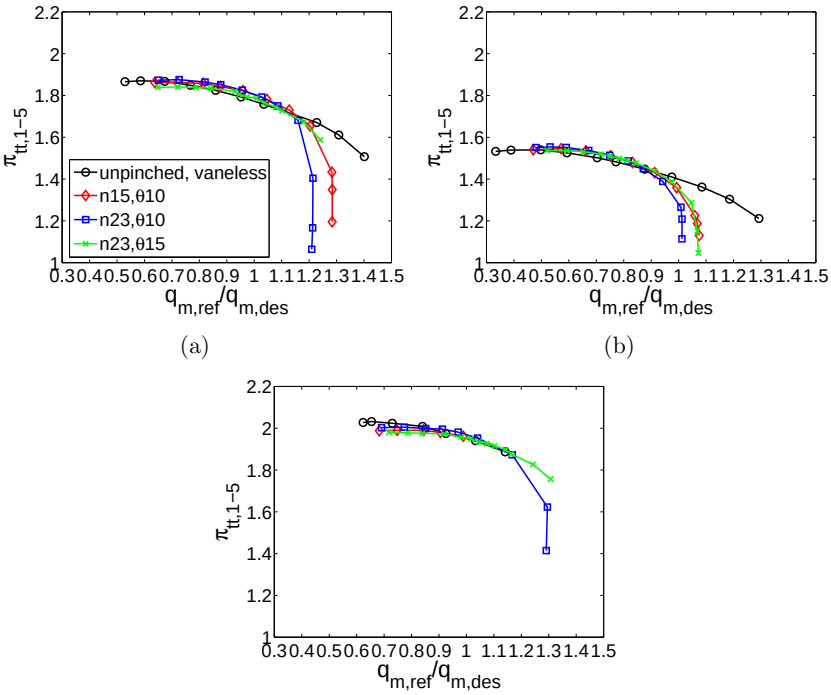

Figure 5.18: Total-to-total stage pressure ratio of the vaned geometries. (a) $N/N_{\text{des}} = 1.00$, (b) $N/N_{\text{des}} = 0.82$ and (c) $N/N_{\text{des}} = 1.06$.

pinch has the lowest efficiency. At high flow, the shroud pinch has the highest, the case with least pinch at the shroud has the second highest, and the case with most pinch has the lowest impeller efficiency.

For the combined impeller and diffuser performance, all the cases with all three mass flows have higher efficiency than the unpinched case, except for the case with least pinch at the shroud at low flow. At the design and low flows, the shroud pinch case has the highest efficiency, the case with most pinch has the second highest, and the case with least pinch the lowest efficieny. At high flow, the case with least pinch at the shroud has the second highest efficiency, and otherwise the order remains the same it was for the impeller efficiency.

The impeller and the combined impeller and diffuser total-to-static pressure

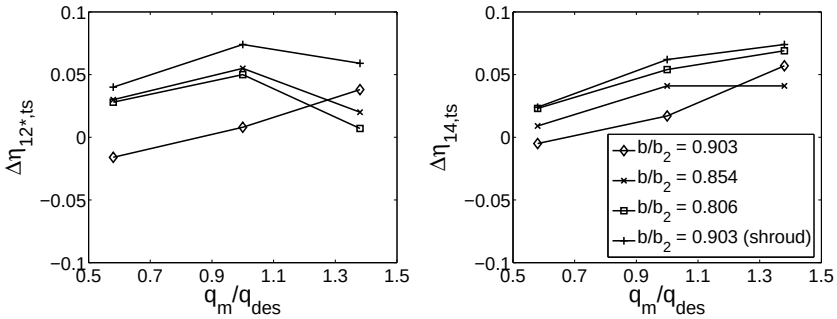

(a) (b)

Figure 5.19: Change in total-to-static isentropic efficiency for the vaneless geometries. (a) impeller and (b) impeller and diffuser

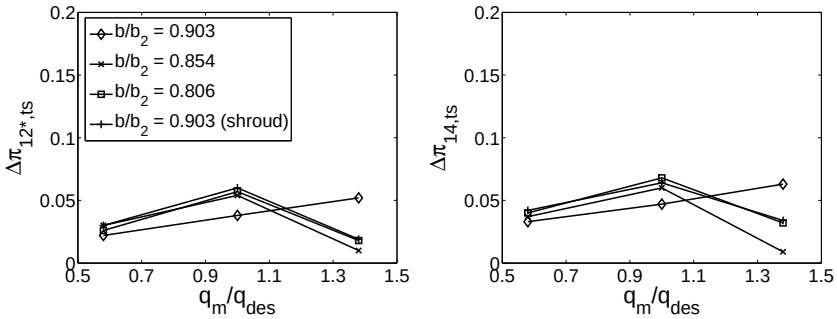

(a) (b)

Figure 5.20: Change in total-to-static pressure ratio for the vaneless geometries. (a) impeller and (b) impeller and diffuser

ratios are presented in Figure 5.20. All the pinched cases have higher pressure ratios for the impeller and the combined impeller and diffuser than the unpinched case. At the design and low flows, the case with the least pinch at the shroud has the lowest pressure ratios for both the impeller and the combined impeller and diffuser. At the high flow it has the highest pressure ratios. The differences between the other pinched cases are minor.

The vaneless diffuser total pressure loss coefficients for the diffuser, the volute and the combined diffuser and volute are presented in Figure 5.21. In the diffuser, all the pinched cases have lower loss coefficients than the unpinched

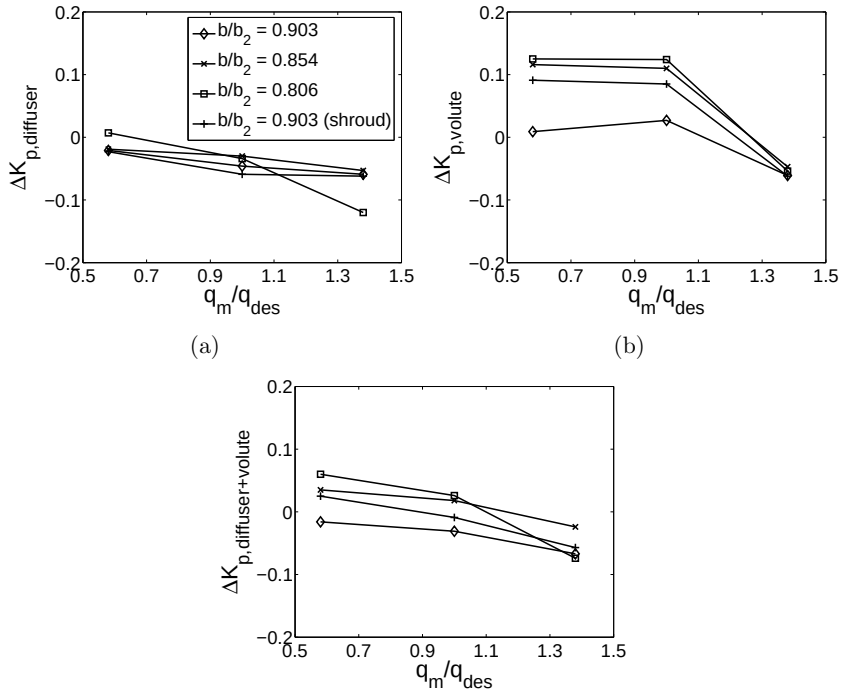

Figure 5.21: Change in total pressure loss coefficient for the vaneless geometries. (a) diffuser, (b) volute and (c) diffuser and volute

geometry, except for the case with the most pinch, which has slightly higher loss at the low flow. The case with the most pinch has the lowest pressure loss coefficient at the high flow. Otherwise there is not much difference between the different pinched cases. At the design and low flows, the pinched geometries have higher pressure losses at the volute, but the case with the least pinch at the hub and at the shroud has hardly any higher losses. At the high flow, all the pinched geometries have lower volute pressure losses than the unpinched case, and there are is difference between the different pinched cases. The $b_{2'}/b_2 = 0.903$ (hub & shroud) has the lowest combined pressure losses, and they are somewhat lower than those of the unpinched case. The case with the shroud pinch has the second lowest combined pressure losses and they are scarcely any higher at the low flow, almost the same at the design flow and lower at the high flow than those of the unpinched geometry.

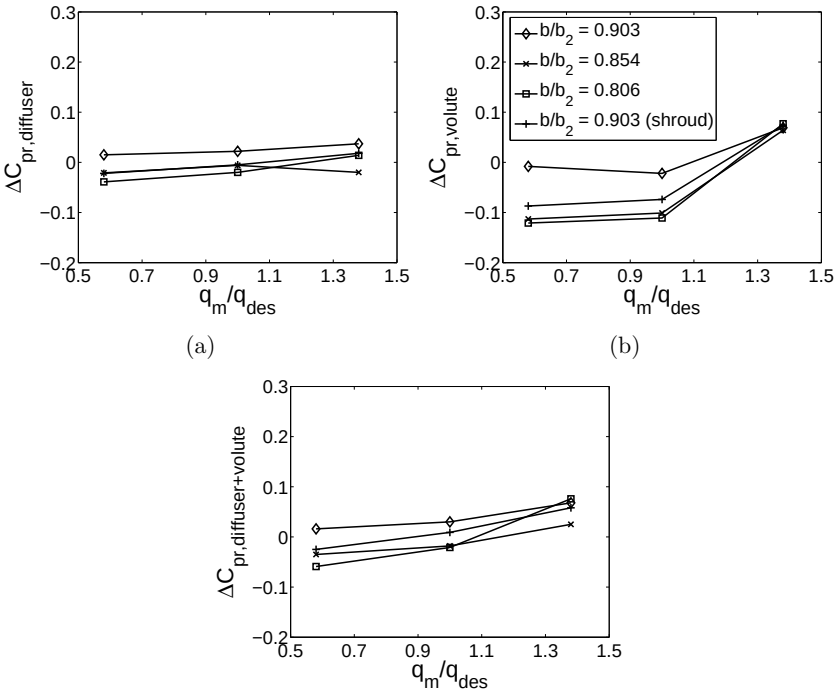

Figure 5.22: Change in static pressure rise coefficient for the vaneless geometries. (a) diffuser, (b) volute and (c) diffuser and volute

The vaneless diffuser static pressure rise coefficients for the diffuser, the volute, and the combined diffuser and volute are presented in Figure 5.22. The pressure rise coefficients in the diffuser at the design and at the low flow are higher than that of the unpinched only with the $b_{2'}/b_2 = 0.903$ (hub & shroud) geometry. At the high flow it is higher with the said geomtry, while the $b_{2'}/b_2 = 0.903$ (shroud) and the $b_{2'}/b_2 = 0.806$ have about the same pressure rise coefficient than the unpinched case. At the design and low flows, all the cases have lower pressure rise in the volute than the unpinched one, with the $b_{2'}/b_2 = 0.903$ (hub & shorud) beign very close to the unpinched case. At the high flow, all the pinched cases have higher pressure rise in the volute than the unpinched one, and there are no differences between the different pinched cases. The combined pressure rise coefficients behave similarly to the other two pressure rise coefficients.

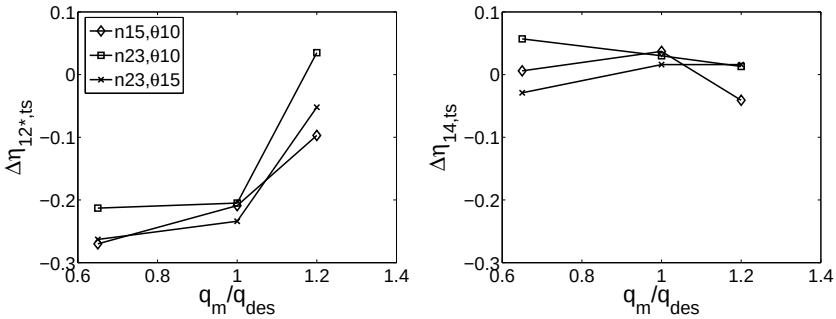

(a) (b)

Figure 5.23: Change in total-to-static isentropic efficiency for the vaned geometries. (a) impeller and (b) impeller and diffuser

The vaned diffuser efficiencies and pressure ratios are presented in Figures 5.23 and 5.24. At all flow rates, the impeller efficiency is significantly lower than that of the vaneless unpinched case for all the vaned diffusers except the 23-vaned with the vane turning angle of 10°, which has slighly better efficiency at the high flow. At the low flow, the 23-vaned with the vane turning angle of 10° has higher combined efficiency, the 15-vaned diffuser approximately the same, and the 23-vaned with the vane turning angle of 15° has lower combined efficiency than the unpinched vaneless diffuser. At the design flow, the 23-vaned with the vane turning angle has approximately the same combined efficiency, and the other two vaned diffusers have somewhat higher combined efficiency than the unpinched vaneless one. At the high flow the 15-vaned has lower combined efficiency than, and the two 23-vaned have approximatly the same combined efficiency than the unpinched vaneless construction. The combined pressure ratio of the impeller and the diffuser for both 23-vaned cases are higher at all mass flows. The case with more vane turning has the lowest pressure ratio of all vaned geometries at the low flow, about the same pressure ratio with the design flow, and the best pressure ratio at the high flow. The 15-vaned diffuser has about the same pressure ratio at the design and the flow as the 23-vaned with the same vane turning, but it has clearly the lowest pressure ratio at the high flow, and it is worse than that of the unpinched vaneless geometry. The changes in the impeller efficiencies are so drastic with the the low and the design flows, that there is reason to consider that the vaned results are being influenced the diffuser vanes as mentioned previously.

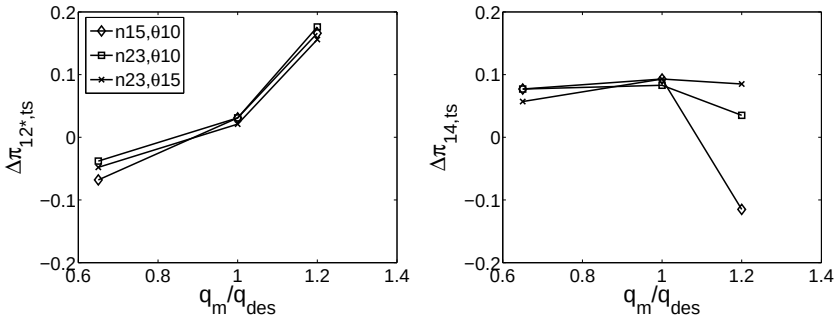

(a) (b)

Figure 5.24: Change in total-to-static pressure ratio for the vaned geometries. (a) impeller and (b) impeller and diffuser

The pressure loss and rise coefficents for the vaned geometries are presented in Figures 5.25 and 5.26. The pressure loss coefficients in the diffuser at the low and design flows are about the same for all the vaned and the unpinched vaneless cases. At the high flow, the pressure losses in the diffuser are higher with the vaned diffusers, and there are no major differences between the vaned cases. In the volute, the 23-vaned diffuser with more vane turning has clearly lower pressure loss coefficient at the low and high flows than the unpinched case. At the design flow, the pressure loss in the volute is approximately the same as for the unpinched geometry. At the low and design flow, the other two diffusers have slighlty higher pressure losses in the volute than the unpinched case. There are no major differences between the two diffusers. At the high flow, the 15-vaned diffuser has slightly lower pressure losses than the unpinched one, and the 23-vaned with a lower vane turning angle falls between the other two diffusers. The combined pressure loss coefficient for the 15-vaned diffuser is very close to that of the unpinched vaneless case at the design and the flow. At the high flow it is higher. This is the case also with both 23-vaned diffusers, but they have lower pressure losses at the high flow than the 15-vaned one.

The pressure rise coefficent in the diffuser is higher at the low and design flow for all the geometries, and there are no major differences between the vaned cases. At the high flow it is lower than that of the unpinched vaneless case. It is the lowest for the 15-vaned diffuser and the second lowest for the 23-vaned one with less vane turning. The pressure rise in the volute behaves opposite to the pressure rise in the diffuser when the mass flow is increased.

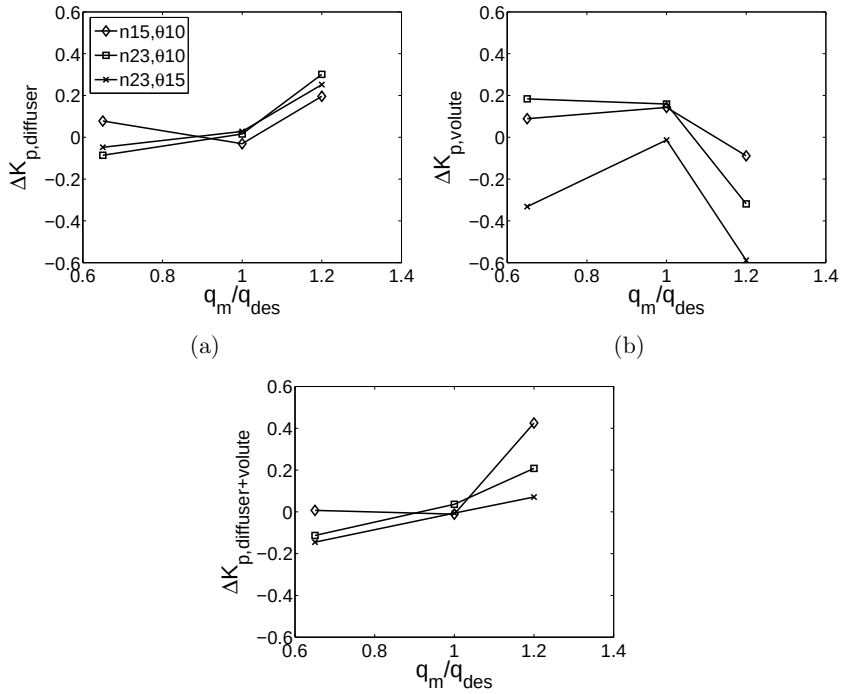

Figure 5.25: Change in total pressure loss coefficient for the vaned geometries. (a) diffuser, (b) volute and (c) diffuser and volute

The 23-vaned diffuser with more vane turnign has the highest pressure rise in the volute, while the 15-vaned one has the lowest. The combined pressure rise coefficient behaves similarly to the diffuser pressure rise coefficient.

5.3.3 Flow fields

Absolute flow angles measured from the radial direction, before and after the vaneless diffusers at the design, low and high mass flows are presented in Figures 5.27, 5.28 and 5.29, respectively. At the design flow there is clearly a backflow area with the unpinched geometry after the impeller (flow angle exceeds 90°). When the pinch is implemented, the backflow area becomes extinct. When the pinch is implemented at both the hub and the shroud, the more pinch there is, the more radial the flow is. However, even though the

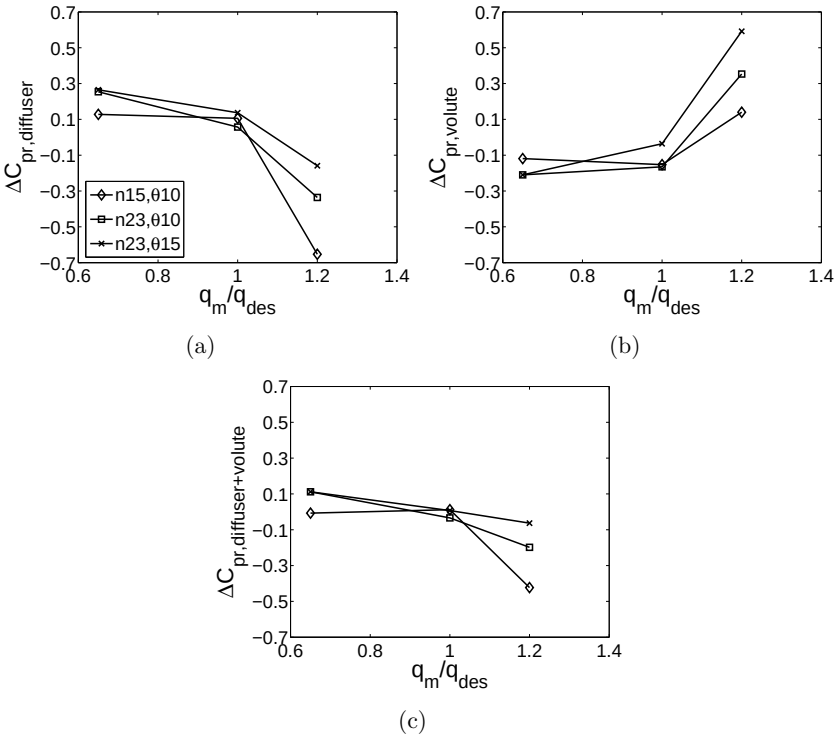

Figure 5.26: Change in static pressure rise coefficient for the vaned geometries. (a) diffuser, (b) volute and (c) diffuser and volute

case with pinch only at the shroud has the shared least pinch, the flow is the second most radial. After the diffuser the pinch does not have much effect. Nearer to the hub (approximately 40% of the channel width) the axial angle distributions are the same for all the geometries. Above that, closer to the shroud, the more pinch is implemented, the more radial the flow is.

At the low flow, after the impeller, there are no significant differences between the different pinched cases. Solely the implementation of the pinch makes the flow more radial near the shroud. Near the hub, the unpinched case and the case $b_{2'}/b_2 = 0.903$ (hub & shroud) have somewhat more (about 5°) radial flow. After the diffuser, the pinch has a notable effect only on the flow angles near the hub, where the two cases with the most shroud pinch have somewhat more radial flow. At the high flow, the axial flow angle distributions after the impeller and the diffuser behave similarly to those at the

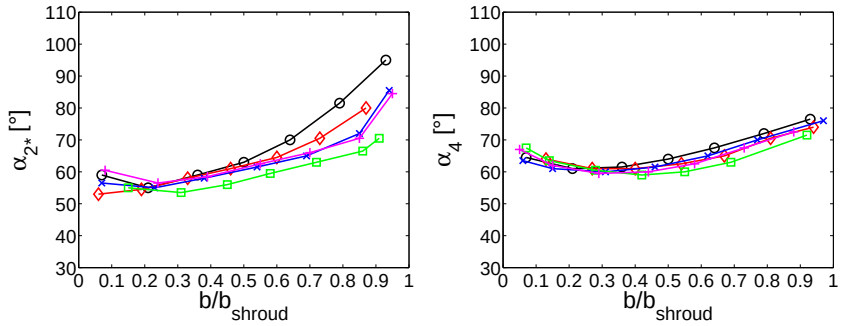

(a) (b)

Figure 5.27: Absolute flow angle distributions for the vaneless diffusers from the radial direction at the design flow, (a) after the impeller and (b) after the diffuser.

design flow. After the diffuser, the differences between the different geometries are slightly more evident at the high flow.

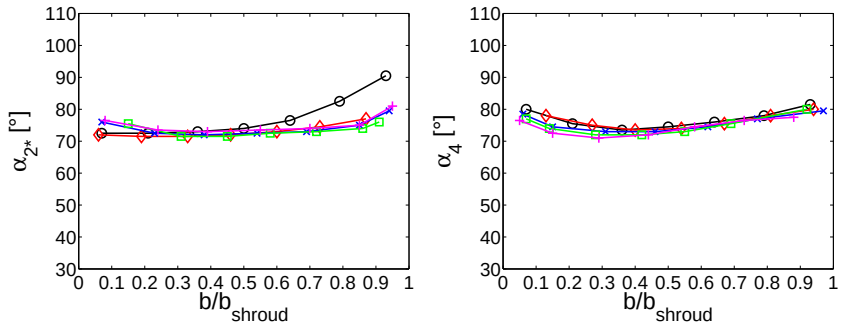

(a) (b)

Figure 5.28: Absolute flow angle distributions for the vaneless diffusers from the radial direction at the low mass flow, (a) after the impeller and (b) after the diffuser.

The flow velocity distributions of the vaneless cases at the design, low and high flows are presented in Figures 5.30, 5.31 and 5.32, respectively. The flow velocities have been calculated using the total pressure measured with the cobra probe, the static pressure measured with the closest mounting, and the

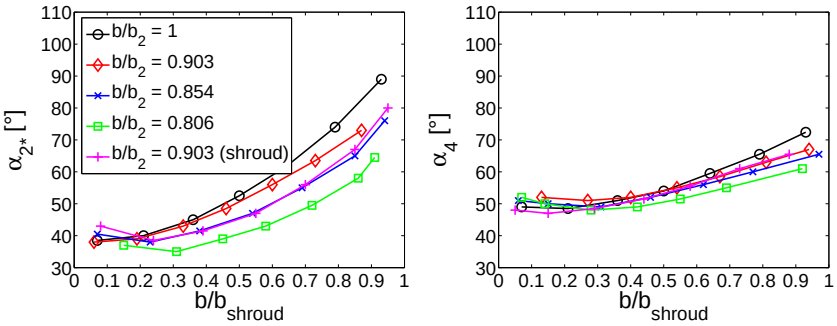

(a) (b)

Figure 5.29: Absolute flow angle distributions for the vaneless diffusers from the radial direction at the high mass flow, (a) after the impeller and (b) after the diffuser.

total temperature measured with all the Kiel probes (mean value). After the impeller, at all mass flows, the velocity distributions are clearly more uniform when the pinch is implemented. The pinch evidently decreases the slow flow area near the shroud, caused by the impeller exit flow. After the diffuser, the flow velocities have decreased and the flow is more uniform. At the design and high flow, the pinch increases the velocities after the diffuser. At the low flow, the pinch has only a minor effect of decreasing the flow velocities near the shroud.

The radial velocity distributions before and after the vaneless diffusers, for all three mass flows, are presentd in Figures 5.33, 5.34 and 5.35. The radial velocity component has been calculated with the measured flow angle and the above-mentioned calculated flow velocity. The pinch increases the radial velocity in general. Only at the hub, the radial velocities are approximately the same with the pinched and unpinched cases. Increased radial velocities are obvious: because the flow area is decreased, the radial flow velocity must increase in order to fulfill the continuation equation. All in all, the more pinch, the more uniform the radial velocity profiles are. This is the case especially before the diffuser, but the trend can be seen after the diffuser as well.

The tangential velocity profiles for the vaneless cases are presented in Figures 5.36, 5.37 and 5.38. The tangential velocity component is obtained in the same way as the radial velocity component. The implementation of the pinch increases the tangential velocities, especially after the impeller, near

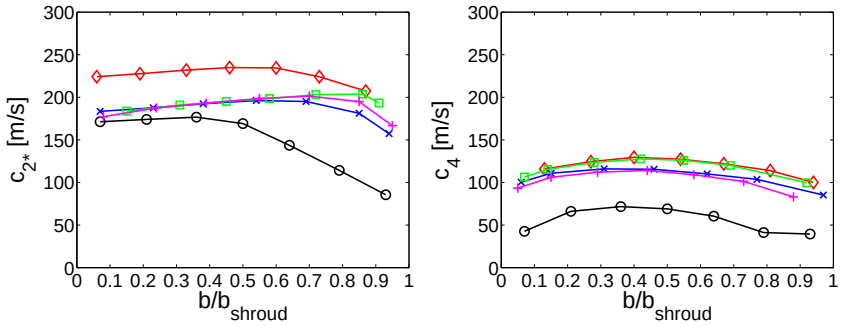

(a) (b)

Figure 5.30: Absolute flow velocity distributions for the vaneless diffusers at the design flow, (a) after the impeller and (b) after the diffuser.

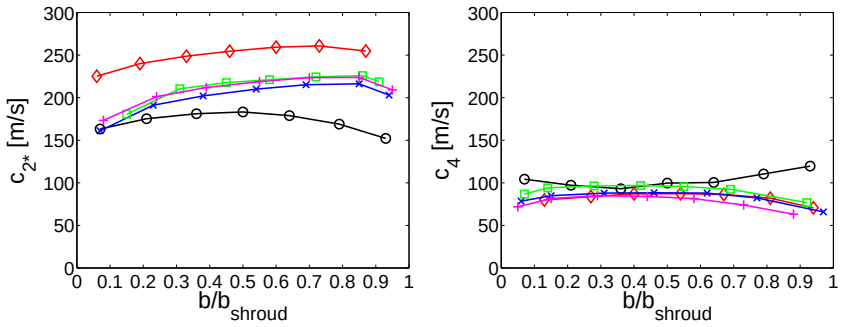

(a) (b)

Figure 5.31: Absolute flow velocity distributions for the vaneless diffusers at the low mass flow, (a) after the impeller and (b) after the diffuser.

the shroud. At the impeller exit the pinch also makes the tangential velocity profiles more slightly less uniform, but after the diffuser the pinch makes the tangential velocity profiles somewhat more uniform.

Axial absolute flow angle distributions before and after the vaned diffusers are presented in Figures 5.39, 5.40 and 5.41. At the design flow, the n23,θ10 has the most tangential flow both before and after the diffuser. The different angle profile for this diffuser might be either because the probe traverse hole is closer to a diffuser vane for this geometry, or it is possible that the

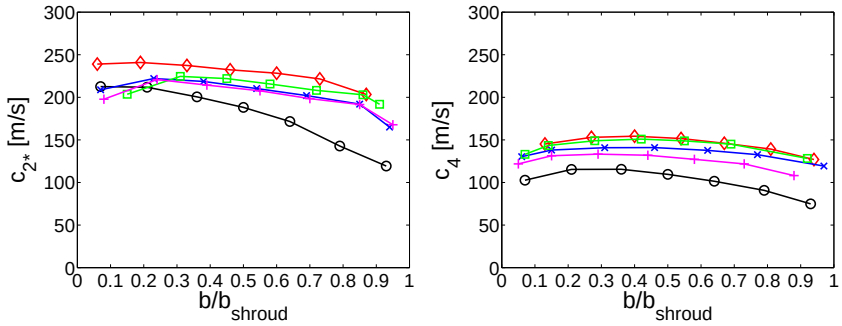

(a) (b)

Figure 5.32: Absolute flow velocity distributions for the vaneless diffusers at the high mass flow, (a) after the impeller and (b) after the diffuser.

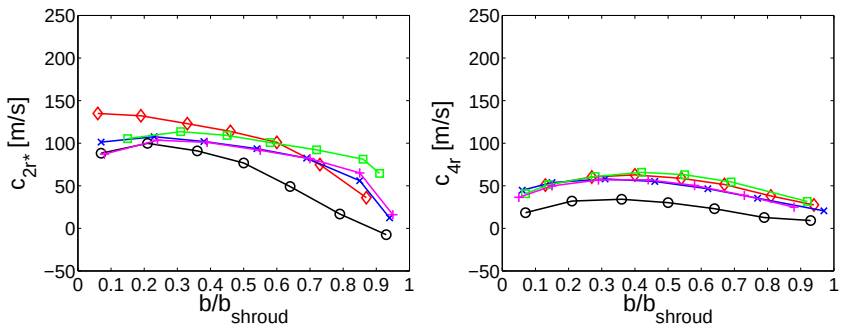

(a) (b)

Figure 5.33: Radial velocity distributions for the vaneless diffusers at the design flow, (a) after the impeller and (b) after the diffuser.

angle indicator on the traversion device has moved (nulling process failed). This should be kept in mind, because if the former is the reason, it might cause distortion to all the diffuser inlet profiles for this geometry, and if the latter is the reason, all the values are incorrect but the profile shapes should be correct. Before the diffuser, the 15-vaned and the n23,θ15 have almost identical angle profiles, and they are quite close to those of the unpinched vaneless diffuser. There is a small backflow area after the impeller, near the shroud for every case. After the diffuser, the n23,θ15 has the most radial angle profile. The angle distribution is clearly more uniform after the dif-

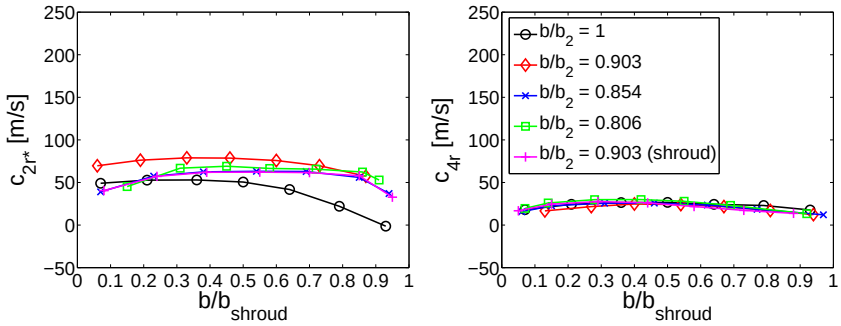

(a) (b)

Figure 5.34: Radial velocity distributions for the vaneless diffusers at the low mass flow, (a) after the impeller and (b) after the diffuser.

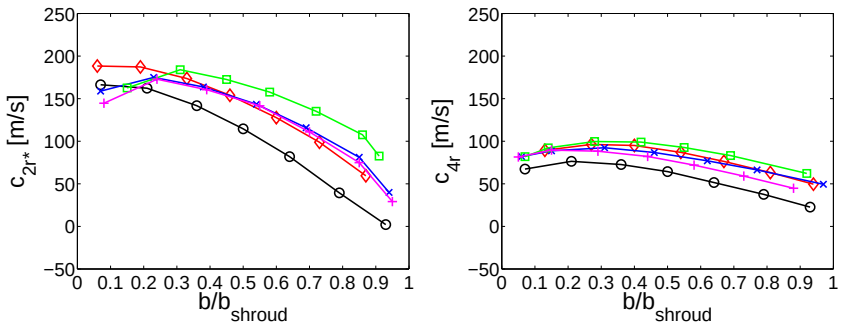

(a) (b)

Figure 5.35: Radial velocity distributions for the vaneless diffusers at the high mass flow, (a) after the impeller and (b) after the diffuser.

fuser for every case. However, unlike with the vaneless diffusers, the flow is slightly more tangential near the hub than near the shroud.

At the low flow, the two 23-vaned diffusers have similar profiles after the impeller, the n23,θ15 having more radial flow. Near the hub the 15-vaned diffuser falls between the two 23-vaned ones. Near the shroud (approximately the upper 40% of the channel), the flow angle exceeds 90° and is almost 110°[1]

[1]The maximum turning angle from the radial direction for the cobra probe, which the traversion device allowed, was 62°, so the flow angle might be even larger.

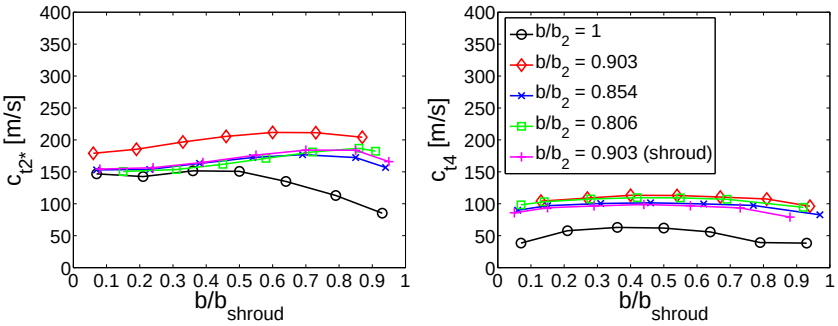

(a) (b)

Figure 5.36: Tangential velocity distributions for the vaneless diffusers at the design flow, (a) after the impeller and (b) after the diffuser.

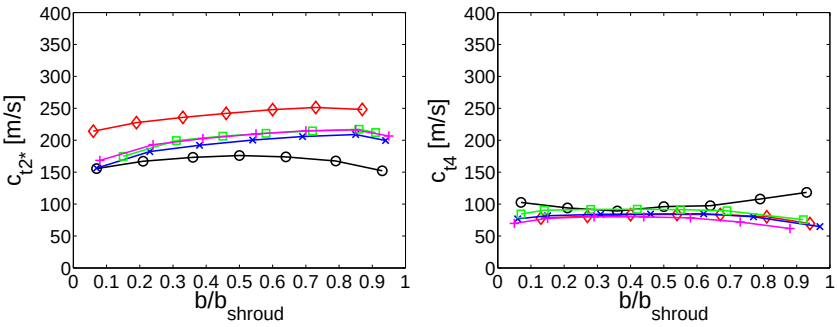

(a) (b)

Figure 5.37: Tangential velocity at distributions for the vaneless diffusers the low mass flow, (a) after the impeller and (b) after the diffuser.

for the upper 30% of the channel. After the diffuser, the angle profiles are similar to those of the design flow. At the high flow before the diffuser, the n23,θ10 has the least radial flow, while the n15,θ15 has the most radial flow, and after the diffuser the angle distributions are similar to those at the design and low flows.

The absolute flow velocity profiles for the vaned diffusers are presented in Figures 5.42, 5.43 and 5.44. These velocities has been obtained in the same way as they were for the vaneless configurations. At the design and high

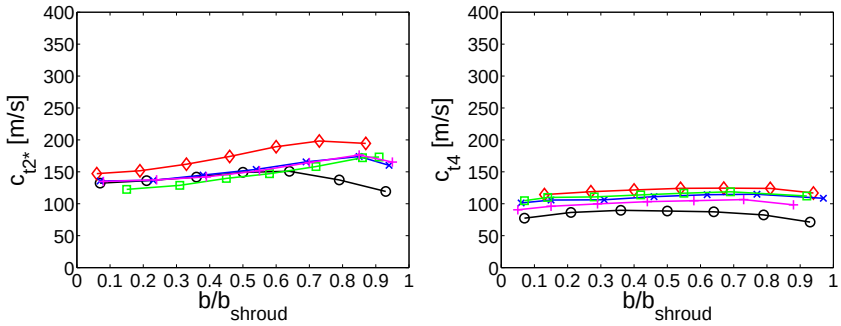

(a) (b)

Figure 5.38: Tangential velocity distributions for the vaneless diffusers at the high mass flow, (a) after the impeller and (b) after the diffuser.

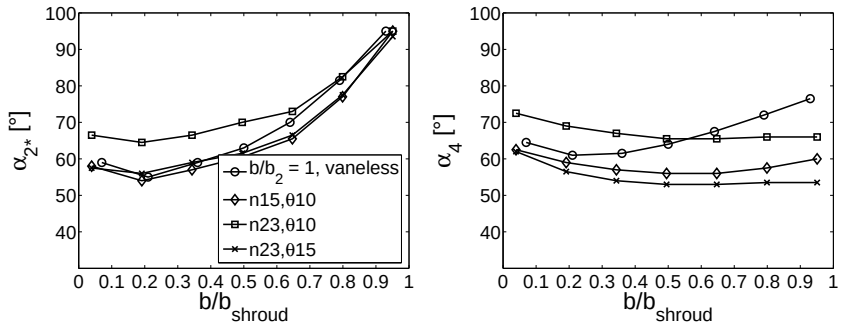

(a) (b)

Figure 5.39: Absolute flow angle distributions for the vaned diffusers from the radial direction at the design flow, (a) after the impeller and (b) after the diffuser.

flows, the velocity profiles before the diffuser are almost the same for all the vaned diffusers, and the profiles are very similar to that of the unpinched vaneless case, although the velocities are higher for the vaned diffusers. Before the diffuser at the low flow, a slow flow area near the shroud is clearly visible for all the vaned diffusers, and all the profiles are very skewed. After the diffuser at the design and high flows, the diffuser with 15 vanes has the highest velocity and the n23,θ10 has the slowest. It seems that the surface area of the vanes is the dominant factor in slowing the flow. Even though the diffuser with 15 vanes has longer vanes, the total surface area of the diffuser

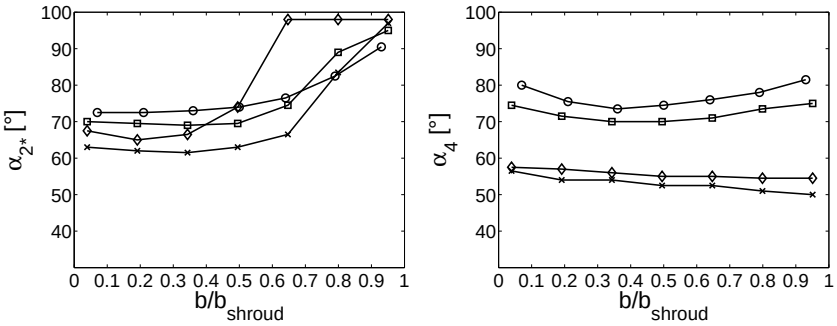

(a) (b)

Figure 5.40: Absolute flow angle distributions for the vaned diffusers from the radial direction at the low mass flow, (a) after the impeller and (b) after the diffuser.

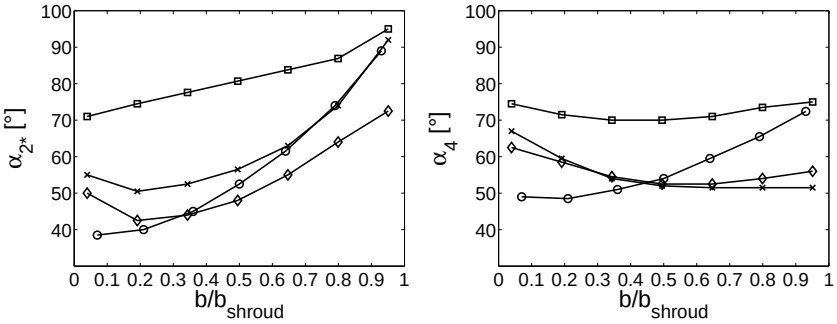

(a) (b)

Figure 5.41: Absolute flow angle distributions for the vaned diffusers from the radial direction at the high mass flow, (a) after the impeller and (b) after the diffuser.

vanes is smaller. The effect of the length is seen when the two 23-vaned diffusers are compared. The one with more vane turning has a marginally shorter flow path than the one with less vane turning, and it also has slightly higher flow velocity. At the low flow, the two vanes with the same amount of vane turning, the n15,θ10 and the n23,θ10, have almost identical velocity profiles, while the third diffuser has a similar profile, but the velocity is slower.

The radial velocity components for the vaned diffusers, attained like those in

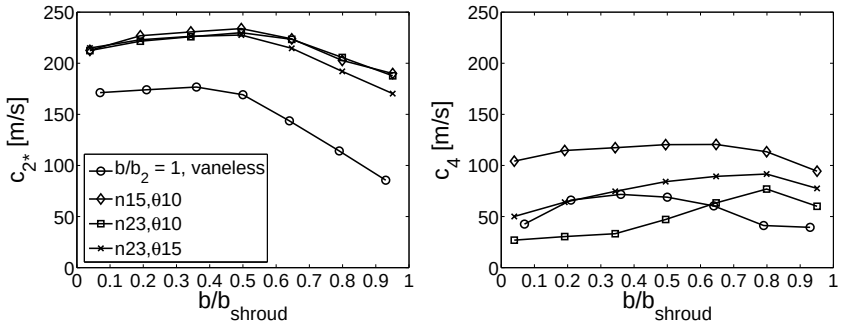

(a) (b)

Figure 5.42: Absolute flow velocity distributions for the vaned diffusers at the design flow (a) after the impeller and (b) after the diffuser.

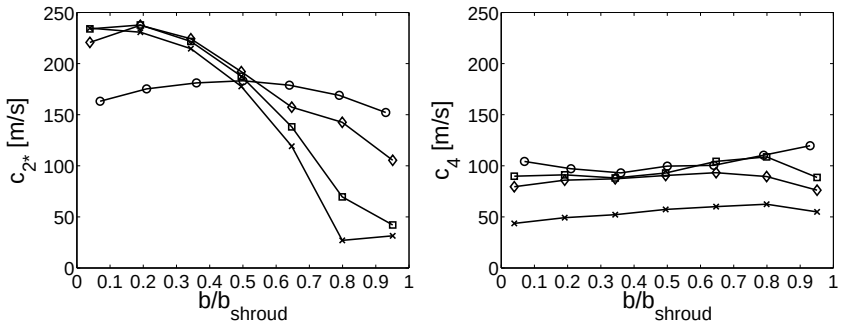

(a) (b)

Figure 5.43: Absolute flow velocity distributions for the vaned diffusers at the low mass flow, (a) after the impeller and (b) after the diffuser.

the vaneless cases, are presented in Figures 5.45, 5.46 and 5.47. The radial velocity profiles before the diffusers in general follow a similar trend as that of the vaneless unpinched geometry. The radial velocity is slower nearer the shroud. At every mass flow, the 15-vaned diffuser has the highest radial velocity and the n23,θ10 the lowest. The profiles at the diffuser exit for each diffuser follow the same trend; the radial velocity distributions are very even and the radial velocity near the shroud is somewhat higher.

The tangential velocity components for the vaned diffusers, attained like

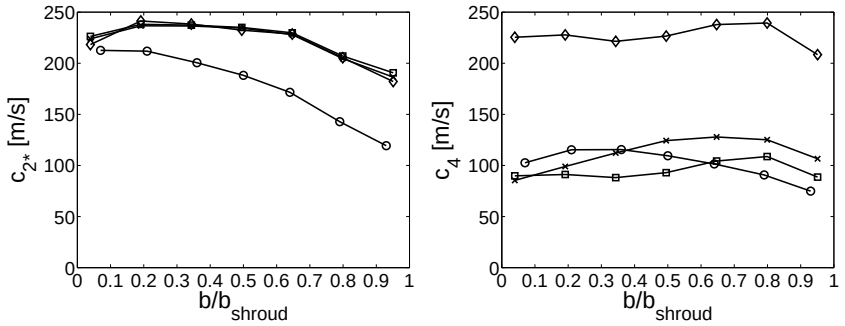

(a) (b)

Figure 5.44: Absolute flow velocity distributions for the vaned diffusers at the high mass flow, (a) after the impeller and (b) after the diffuser.

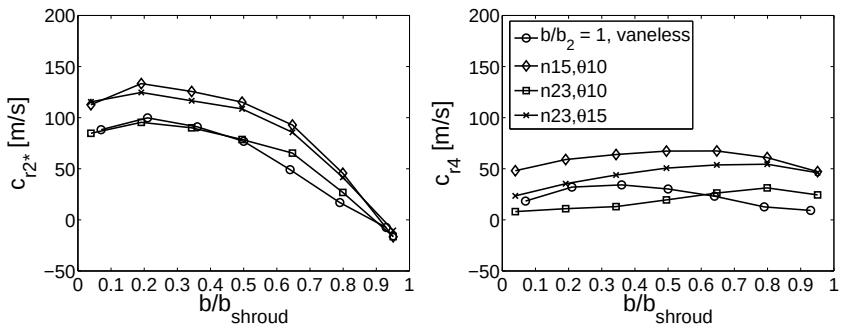

(a) (b)

Figure 5.45: Radial velocity distributions for the vaned diffusers at the design flow (a) after the impeller and (b) after the diffuser.

those in the vaneless cases, are presented in Figures 5.48, 5.49 and 5.50. The tangential velocity distributions before the diffuser at the design and high flow are very even for all the vaned diffusers. The n23,θ10 has the highest tangential velocity, and the 15-vaned diffuser has the lowest tangential velocity at the high flow. At the design flow, the tangential velocities near the hub are identical with the n23,θ15 and the 15-vaned diffuser. Near the shroud, the n23,θ15 has slightly lower tangential velocities. At the low flow, the tangential velocities are also slow near the shroud. After the diffuser, the tangential velocity distributions are very even for all the vaned diffusers. At

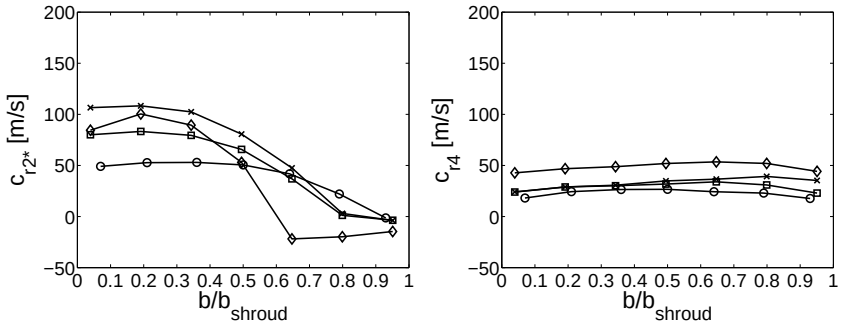

(a) (b)

Figure 5.46: Radial velocity distributions for the vaned diffusers at the low mass flow, (a) after the impeller and (b) after the diffuser.

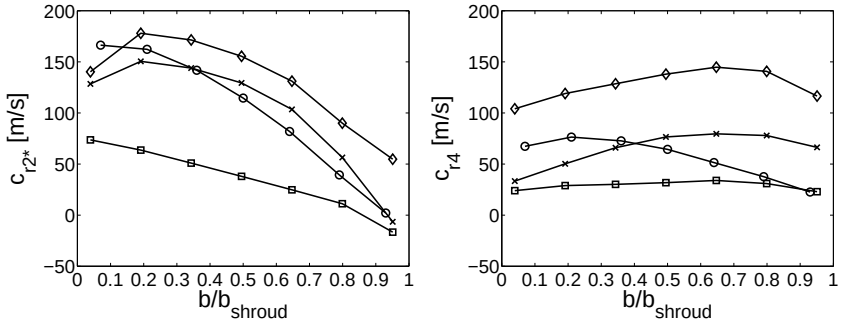

(a) (b)

Figure 5.47: Radial velocity distributions for the vaned diffusers at the high mass flow, (a) after the impeller and (b) after the diffuser.

the design flow and at the high flow, the 15-vaned diffuser has the highest tangential velocity, while at the low flow the n23,θ10 has the highest tangential velocity. At the design, flow the n23,θ10 has the lowest tangential velocity, at the low flow the n23,θ15 has the lowest tangential velocity, and at the high flow the two 23-vaned diffusers have tangential velocities very close to each other.

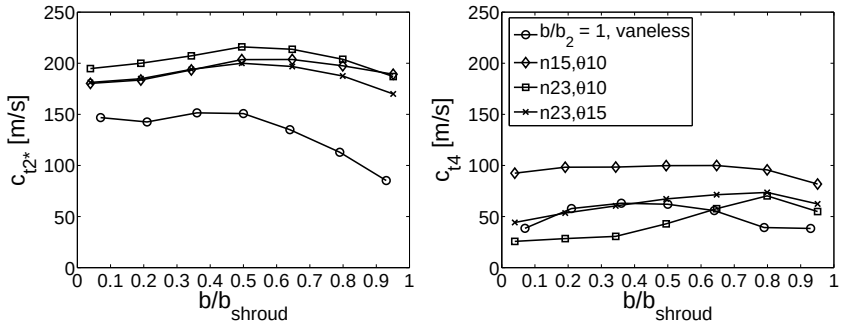

(a) (b)

Figure 5.48: Tangential velocity distributions for the vaned diffusers at the design flow (a) after the impeller and (b) after the diffuser.

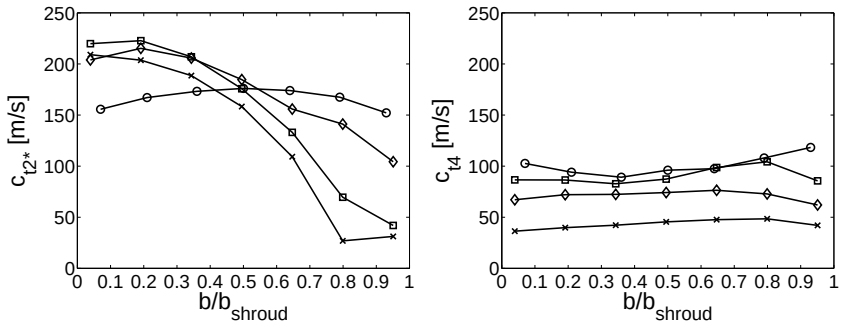

(a) (b)

Figure 5.49: Tangential velocity distributions for the vaned diffusers at the low mass flow, (a) after the impeller and (b) after the diffuser.

5.3.4 Static pressure distributions

The volute pressure rise and loss coefficients suggest that the volute does not match properly when the diffuser is pinched or the vaned diffuser is installed. Therefore the circumferential pressure distributions and the radial static pressure distributions in the diffuser are studied. The circumferential pressure distributions before the diffusers for both the vaneless and vaned diffusers are presented in Figures 5.51 and 5.52, respectively.

The circumferential static pressure distributions before the diffuser for the

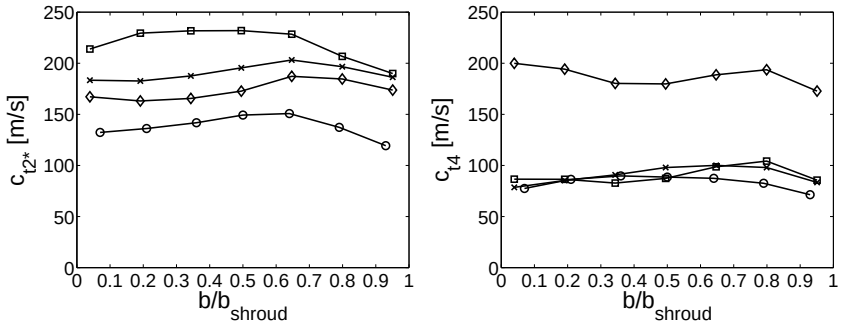

(a) (b)

Figure 5.50: Tangential velocity distributions for the vaned diffusers at the high mass flow, (a) after the impeller and (b) after the diffuser.

different vaneless diffusers are similar at all the mass flows. At the design flow, the pressure distribution is very even. At the low flow, the pressure is lower at 90° and higher at 180°, and at the high flow the pressure is higher at 90°. For the vaned diffusers, the pressure distribution at the design flow is quite even, and all the diffusers have a similar profile. At off-design conditions, the two 23-vaned diffusers have more even distribution than the 15-vaned diffuser. All in all, the pressure distributions are more even with the vaned diffusers, which is logical in the sense that the diffuser vanes hinder the interaction between the volute and the impeller.

The circumferential pressure distributions after the diffusers for the vaneless and vaned diffusers are presented in Figures 5.53 and 5.54, respectively. Also the pressure distributions after the diffuser are similar for all the vaneless diffusers. The pressure distribution is very even at the design conditions, which suggests that the pinches used in this study do not significantly affect the matching of the volute. At the low flow, the pressure increases to the direction of the rotation, and at the high flow the pressure decreases to the direction of the rotation. This is in line with results reported in the literature, in e.g. (Reunanen, 2001) and (Shaaban and Seume, 2007). For the vaned diffusers, the circumferential static pressure distribution after the diffuser is slightly skewed at the design flow, and the pressure decreases to the direction of the rotation. At the low flow, the the distribution is quite even, and at the high flow the pressure distributions resemble those at the design flow.

The radial static pressure distribution in the diffuser at the three different

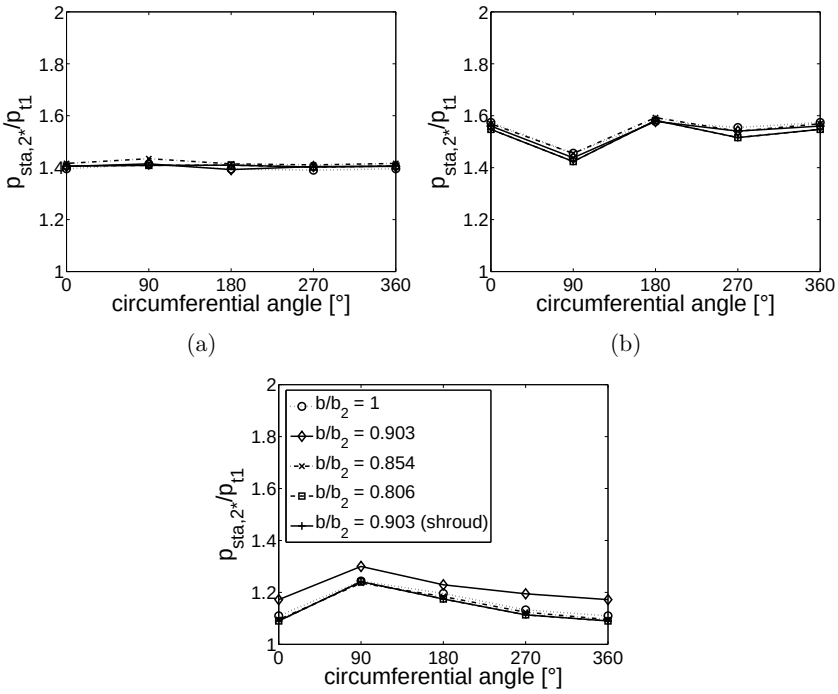

Figure 5.51: Circumferential static pressure distributions before the vaneless diffusers, (a) $q_{\mathrm{m}}/q_{\mathrm{m,des}} = 1.0$ diffuser, (b) $q_{\mathrm{m}}/q_{\mathrm{m,des}} = 0.65$ and (c) $q_{\mathrm{m}}/q_{\mathrm{m,des}} = 1.2$.

mass flows for the vaneless and vaned diffusers are presented in Figures 5.55 and 5.56, respectively. The vaneless diffuser static pressure distributions are very alike for the different constructions. At the design flow, the cases $b_{2'}/b_2 = 0.854$, $b_{2'}/b_2 = 0.903$ (shroud) $b_{2'}/b_2 = 1.0$ have slightly a higher pressure rise in the beginning of the diffuser than the other two. At the low flow, there are no significant differences between the pinched geometries, and at the high flow the $b_{2'}/b_2 = 1.0$ and the $b_{2'}/b_2 = 0.903$ (hub & shroud) have a somewhat higher pressure rise in the beginning of the diffuser.

At the design and low flow, the static pressure distributions for the vaned diffusers are quite similar, and there are no major differences in the profiles. At the design flow, the 15-vaned diffuser has the highest static pressure rise at the last section, while the two 23-vaned diffusers have a higher pressure

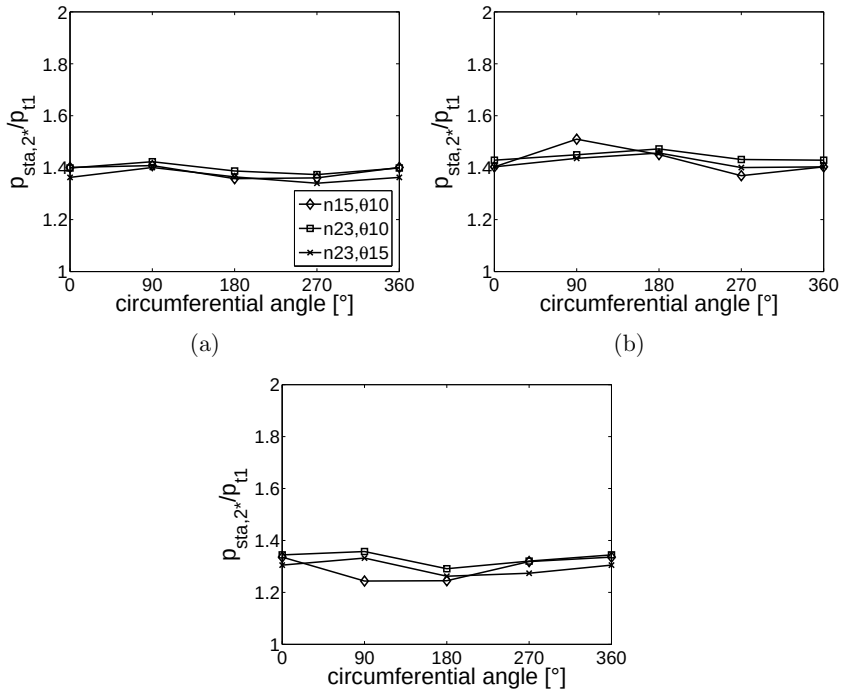

Figure 5.52: Circumferential static pressure distributions before the vaned diffusers, (a) $q_{\mathrm{m}}/q_{\mathrm{m,des}} = 1.0$ diffuser, (b) $q_{\mathrm{m}}/q_{\mathrm{m,des}} = 0.65$ and (c) $q_{\mathrm{m}}/q_{\mathrm{m,des}} = 1.2$.

rise in the middle sections. At the low flow, most of the static pressure increase occurs in the beginnig of the diffuser. Most of the pressure increase has already occured when the radial distance $r/r_2 = 1.3$ is reached. At the high flow, it is evident that the third static pressure tab is too close to a diffuser vane in all the geometries. The pressure distribution suggests that at the high flow, the 15-vaned diffuser does not work as well as the other two. This is in line with the static pressure rise coefficients in the vaned diffusers.

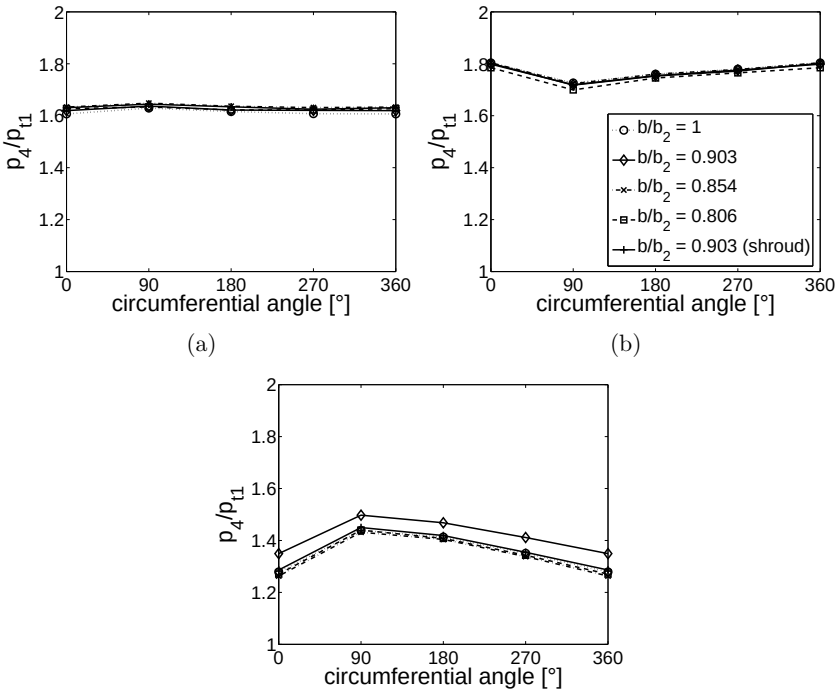

(a) (b)

(c)

Figure 5.53: Circumferential static pressure distributions after the vaneless diffusers, (a) $q_{\mathrm{m}}/q_{\mathrm{m,des}} = 1.0$ diffuser, (b) $q_{\mathrm{m}}/q_{\mathrm{m,des}} = 0.65$ and (c) $q_{\mathrm{m}}/q_{\mathrm{m,des}} = 1.2$.

5.4 Comparison between the measurements and the CFD

5.4.1 Comparison of the overall performance parameters of the vaneless cases

The numerical and the measured total-to-static isentropic efficiency, total-to-static pressure ratios, and pressure loss and rise coefficients changes for the pinched cases, achieved by deducting the efficiency of the unpinched case from the efficiency of the pinched case, are presented in Tables 5.3, 5.4, and 5.5, respectively.

Considering the efficiency changes of different pinched constructions, it is evident that the $k - \epsilon$ turbulence model fails to predict the efficiencies. It

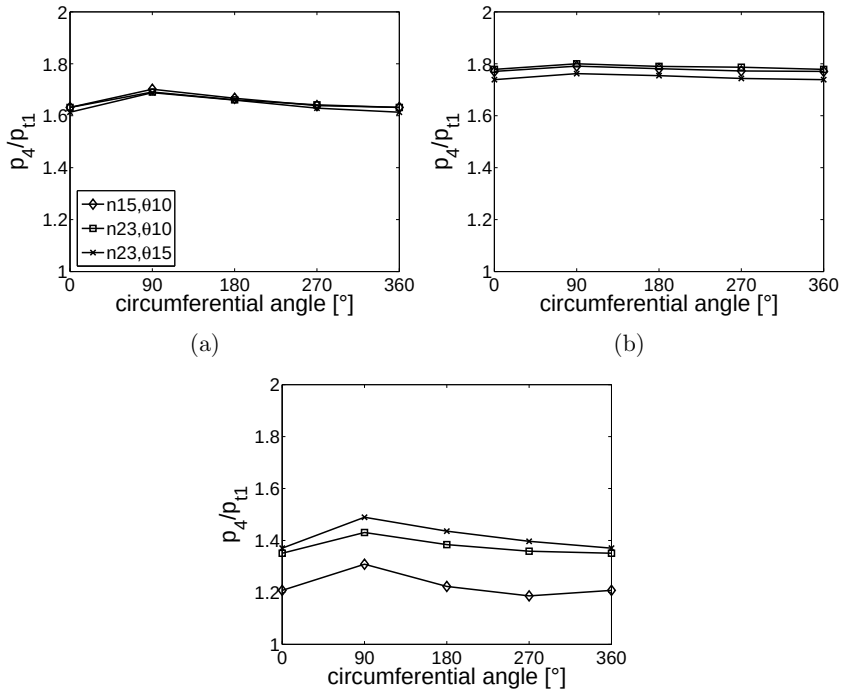

Figure 5.54: Circumferential static pressure distributions after the vaned diffusers, (a) $q_{\mathrm{m}}/q_{\mathrm{m,des}} = 1.0$ diffuser, (b) $q_{\mathrm{m}}/q_{\mathrm{m,des}} = 0.65$ and (c) $q_{\mathrm{m}}/q_{\mathrm{m,des}} = 1.2$.

Table 5.3: Total-to-static isentropic efficiency of vaneless diffusers compared to the efficiency of the unpinched geometry; numerical and measured results.

	$k-\epsilon$		$k-\omega$-SST		measured	
Case	$\Delta\eta_{\mathrm{ts},2^*}$	$\Delta\eta_{\mathrm{ts},4}$	$\Delta\eta_{\mathrm{ts},2^*}$	$\Delta\eta_{\mathrm{ts},4}$	$\Delta\eta_{\mathrm{ts},2^*}$	$\Delta\eta_{\mathrm{ts},4}$
$b_{2'}/b_2 = 0.903$	-0.02	-0.05	-0.01	-0.07	0.01	0.02
$b_{2'}/b_2 = 0.854$	-0.02	-0.03	-0.01	0.03	0.06	0.04
$b_{2'}/b_2 = 0.806$	-0.02	-0.02	0.01	0.04	0.05	0.05
$b_{2'}/b_2 = 0.903$ (shroud)	-0.01	-0.03	0.04	0.04	0.07	0.06

predicts lower impeller and stage efficiencies for all constructions, while the

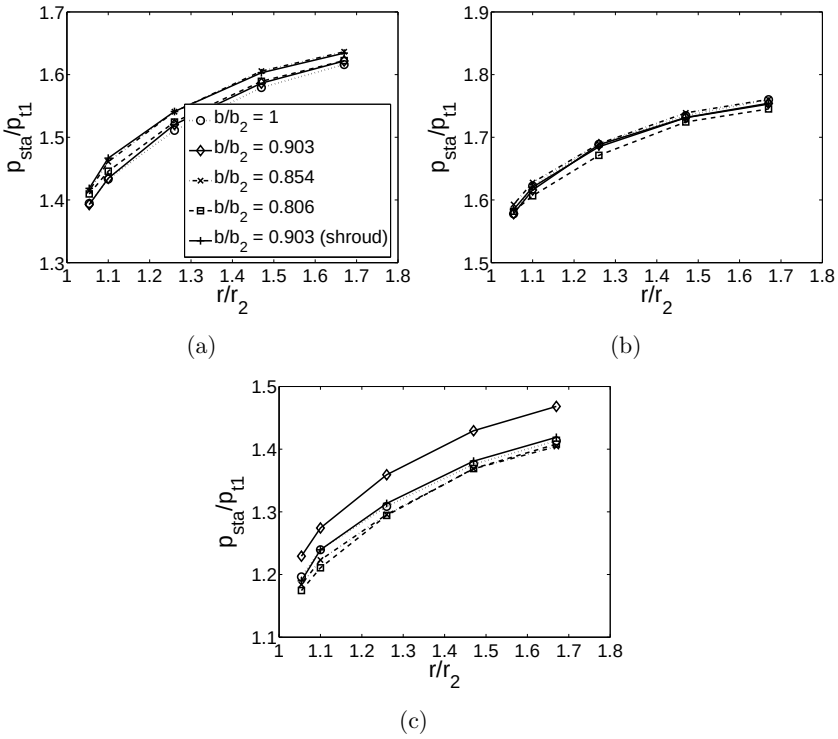

Figure 5.55: Static pressure distributions in the vaneless diffusers, (a) $q_{\mathrm{m}}/q_{\mathrm{m,des}} = 1.0$ diffuser, (b) $q_{\mathrm{m}}/q_{\mathrm{m,des}} = 0.65$ and (c) $q_{\mathrm{m}}/q_{\mathrm{m,des}} = 1.2$. Note that the y-axes are different for the subfigures.

measurements indicate that pinch improves the efficiencies. The $k-\omega$-SST model predicts better impeller efficiencies for the two geometries with the most pinch at the shroud. The measurements indicate that these pinches improve impeller efficiency even more than what the $k-\omega$-SST model indicates. The $k-\omega$-SST model predicts better stage efficiencies for all the pinched geometries, except for the $b_{2'}/b_2 = 0.903$ construction. The predictions for the three other geometries are within two percentage points from the measured ones.

Similarly to the efficiency, the $k-\epsilon$ turbulence model fails to predict the pressure ratios as well. It predicts worse impeller and stage pressure ratios for all the pinched geometries, while the measurement results indicate otherwise. The $k-\omega$-SST model predicts better impeller pressure ratios, the

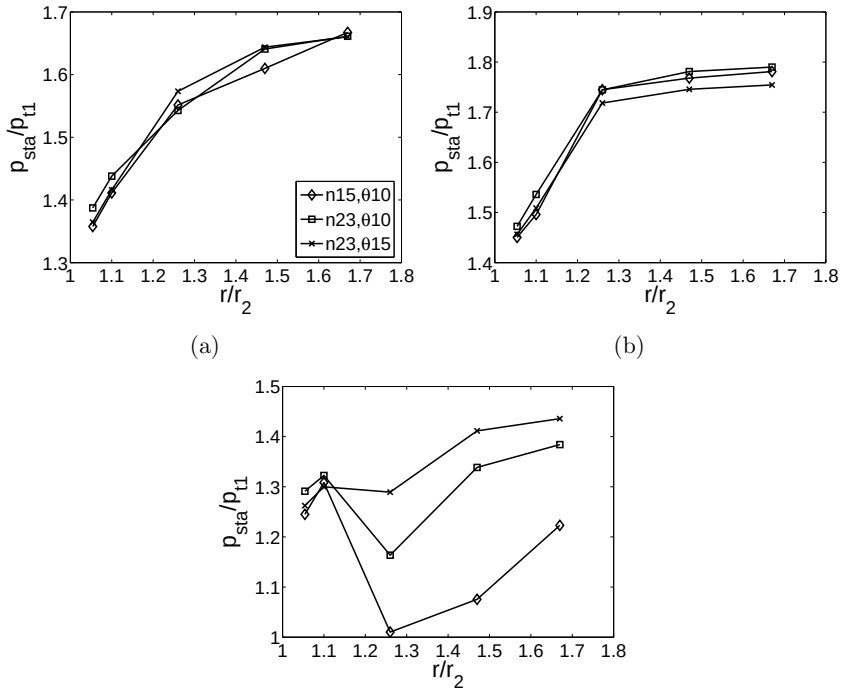

Figure 5.56: Static pressure distributions in the vaned diffusers, (a) $q_{\mathrm{m}}/q_{\mathrm{m,des}}$ = 1.0 diffuser, (b) $q_{\mathrm{m}}/q_{\mathrm{m,des}}$ = 0.65 and (c) $q_{\mathrm{m}}/q_{\mathrm{m,des}}$ = 1.2. Note that the y-axes are different for the subfigures.

Table 5.4: Total-to-static pressure ratios of vaneless constructions compared to the unpinched geometry; numerical and measured results.

	$k-\epsilon$		$k-\omega$-SST		measured	
Case	$\Delta\pi_{\mathrm{ts},2^*}$	$\Delta\pi_{\mathrm{ts},4}$	$\Delta\pi_{\mathrm{ts},2^*}$	$\Delta\pi_{\mathrm{ts},4}$	$\Delta\pi_{\mathrm{ts},2^*}$	$\Delta\pi_{\mathrm{ts},4}$
$b_{2'}/b_2 = 0.903$	-0.04	-0.08	0.03	0.01	0.04	0.05
$b_{2'}/b_2 = 0.854$	-0.04	-0.07	0.02	-0.12	0.05	0.06
$b_{2'}/b_2 = 0.806$	-0.04	-0.06	0.03	-0.10	0.06	0.07
$b_{2'}/b_2 = 0.903$ (shroud)	-0.04	-0.08	0.04	-0.13	0.06	0.06

improvement being approximatley half of what the measurements indicate. However, the $k-\omega$-SST model indicates lower stage pressure ratios, and they are even lower than what the $k-\epsilon$ indicates.

Table 5.5: Total pressure loss and static pressure rise coefficients for the vaneless diffusers compared to the unpinched geometry; measured and numerical results.

	$k-\epsilon$		$k-\omega$-SST		measured	
Case	ΔK_{p}	ΔC_{pr}	ΔK_{p}	ΔC_{pr}	ΔK_{p}	ΔC_{pr}
$b_{2'}/b_2 = 0.903$	0.18	-0.12	0.02	-0.09	-0.05	0.02
$b_{2'}/b_2 = 0.854$	0.16	-0.08	-0.06	-0.08	-0.03	-0.01
$b_{2'}/b_2 = 0.806$	0.15	-0.08	-0.09	-0.11	-0.03	0.02
$b_{2'}/b_2 = 0.903$ (shroud)	0.16	-0.10	-0.05	0.05	-0.06	-0.01

Considering the total pressure loss and static pressure rise coefficients, the $k-\epsilon$ model once again fails to predict the changes. It indicates higher pressure losses and lower pressure rises. The measurements show that the losses are lower and the pressure rise coefficients are lower for two of the pinched geometries ($b_{2'}/b_2 = 0.854$ and $b_{2'}/b_2 = 0.903$ (shroud)) and higher for the other two geometries, although the changes are minimal. The $k-\omega$-SST turbulence model predicts lower pressure losses for all geometries, except for the $b_{2'}/b_2 = 0.903$ case, and lower pressure rises for all geometries, except for the $b_{2'}/b_2 = 0.903$ (shroud) construction. The changes in the coefficients, predicted by the $k-\omega$-SST model, are more drastic than those measured.

5.4.2 Comparison of the overall performance parameters of the vaned cases

The numerical and measured isentropic total-to-static efficiencies, total-to-static pressure ratios, and total pressure loss and pressure rise coefficients for the vaned diffusers are presented in Tables 5.6, 5.7 and 5.8, respectively.

It is evident that here both turbulence models fail to predict the impeller efficiency, but this might also be due to problems in the measurements. Better accuracy is achieved with the stage efficiency. Considering the pressure ratios, the measurements indicate slightly higher impeller and stage pressure

Table 5.6: Total-to-static isentropic efficiency of vaned diffusers compared to the efficiency of the unpinched vaneless geometry; measured and numerical results.

	$k-\epsilon$		$k-\omega$-SST		measured	
Case	$\Delta\eta_{\mathrm{ts},2^*}$	$\Delta\eta_{\mathrm{ts},4}$	$\Delta\eta_{\mathrm{ts},2^*}$	$\Delta\eta_{\mathrm{ts},4}$	$\Delta\eta_{\mathrm{ts},2^*}$	$\Delta\eta_{\mathrm{ts},4}$
n15,θ10	0.01	0.02	0.01	0.05	-0.21	0.04
n23,θ10	0.02	0.00	-	-	-0.21	0.03
n23,θ15	0.00	0.01	-	-	-0.23	0.02

ratios, whilst the $k-\epsilon$ model predicts lower pressure ratios. The $k-\omega$-SST model predicts higher impeller and stage pressure ratios, but it predicts higher change in the impeller pressure ratio and lower change in the stage pressure ratio, than the measured ones.

Table 5.7: Total-to-static pressure ratios for the vaned costructions compared to the unpinched vaneless geometry; measured and numerical results.

	$k-\epsilon$		$k-\omega$-SST		measured	
Case	$\Delta\pi_{\mathrm{ts},2^*}$	$\Delta\pi_{\mathrm{ts},4}$	$\Delta\pi_{\mathrm{ts},2^*}$	$\Delta\pi_{\mathrm{ts},4}$	$\Delta\pi_{\mathrm{ts},2^*}$	$\Delta\pi_{\mathrm{ts},4}$
n15,θ10	-0.02	-0.02	0.11	0.04	0.03	0.09
n23,θ10	-0.02	-0.03	-	-	0.03	0.08
n23,θ15	-0.03	-0.03	-	-	0.02	0.09

Table 5.8: Total pressure loss and static pressure rise coefficients for the vaned diffusers compared to the unpinched vaneless geometry; measured and numerical results.

	$k-\epsilon$		$k-\omega$-SST		measured	
Case	ΔK_{p}	ΔC_{pr}	ΔK_{p}	ΔC_{pr}	ΔK_{p}	ΔC_{pr}
n15,θ10	0.07	0.07	-0.01	0.27	-0.03	0.11
n23,θ10	0.09	-0.01	-	-	0.02	0.06
n23,θ15	0.08	0.06	-	-	0.03	0.14

The $k-\epsilon$ turbulence model predicts higher total pressure loss and lower static pressure rise coefficients for the vaned diffusers than what the measurements

indicate. The $k-\omega$-SST model predicts the total pressure loss coefficient quite well, but overestimates the static pressure rise coefficient.

5.4.3 Comparison of the flow fields

The measured and numerical axial flow angle distributions before and after the vaneless diffusers are presented in Figures 5.57 and 5.58, and the axial radial velocity distributions in Figures 5.59 and 5.60. The agreement between the measured angle profiles before the diffuser are quite good with both turbulence models, the ones calculated with the $k-\omega$-SST model being slightly better. After the diffuser, the $k-\epsilon$ model predicts the angle distributions rather well. The $k-\omega$-SST model fails to predict the angle distributions for the unpinched and $b_{2'}/b_2 = 0.903$ constructions. For the other three cases, the $k-\omega$-SST model works better, but still predicts more skewed angle profiles than the $k-\epsilon$ model.

The $k-\omega$-SST turbulence model predicts the radial velocity distributions after the impeller better than the $k-\epsilon$ model, which also predicts the profiles rather well. For the unpinched vaneless diffuser, near the hub, the $k-\epsilon$ model predicts the magnitude of the radial velocity better, but in general the $k-\omega$-SST model predicts the distribution better, even though it overpredicts the radial velocity. In general, most differences in the profiles are near the hub. After the diffuser, the $k-\epsilon$ model predicts the distributions better for the unpinched and $b_{2'}/b_2 = 0.903$ cases than the $k-\omega$-SST model. For the other three cases, there are no major differences between the two turbulence models, and the agreement with the measurements is rather good, the greatest differences being near the hub.

The measured and numerical axial flow angle distributions before and after the vaned diffusers are presented in Figures 5.61 and 5.62, and radial velocity distributions in Figures 5.63 and 5.64. After the impeller, in the only vaned diffuser, the 15-vaned, which was modeled with both turbulence models, there are no differences in the angle profiles between the two turbulence models. In general, after the impeller, the agreement between the numerical and measured angle profiles is satisfactory. The greatest differences are near the shroud, and the measured angle profiles are more skewed than the numerical ones. After the diffuser, the agreement between the numerical and measured profiles is better, and there are no differences between the turbulence models.

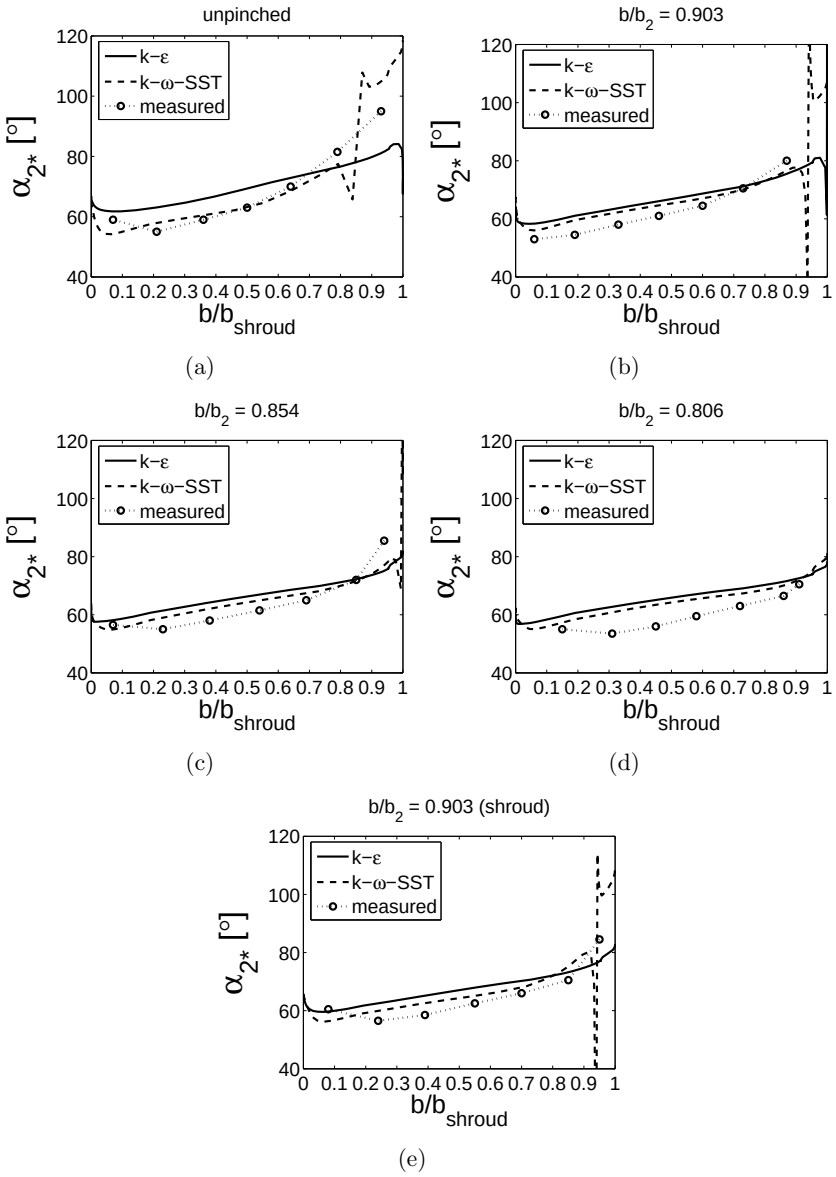

Figure 5.57: Axial flow angle distributions before the vaneless diffusers, both turbulence models and measurement results. (a) $b_{2'}/b_2 = 1.00$, (b) $b_{2'}/b_2 = 0.903$, (c) $b_{2'}/b_2 = 0.854$, (d) $b_{2'}/b_2 = 0.806$, and (e) $b_{2'}/b_2 = 0.903$ (shroud).

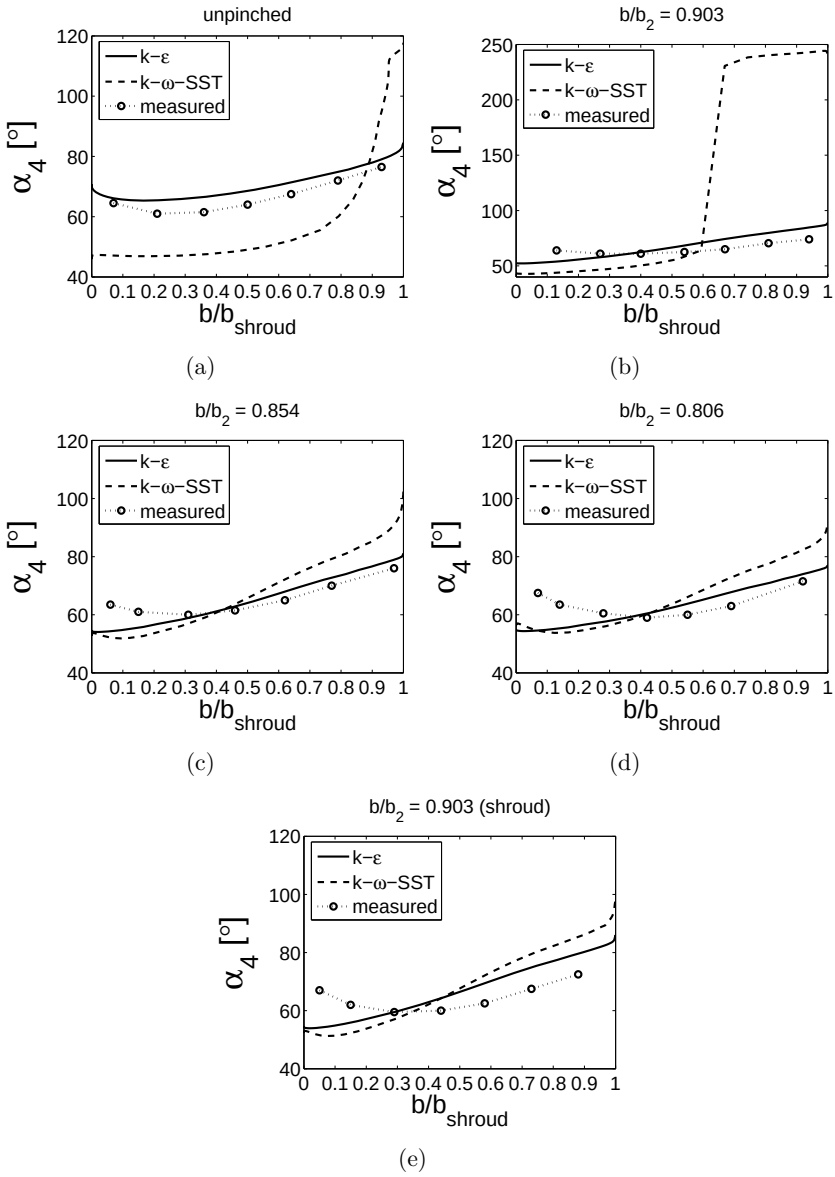

Figure 5.58: Axial flow angle distributions after the vaneless diffusers, both turbulence models and measurement results. (a) $b_{2'}/b_2 = 1.00$, (b) $b_{2'}/b_2 = 0.903$, (c) $b_{2'}/b_2 = 0.854$, (d) $b_{2'}/b_2 = 0.806$, and (e) $b_{2'}/b_2 = 0.903$ (shroud).

The numerical results predict more even radial velocity distributions after the impeller than the ones measured, the largest differences being near the shroud, where the numerical results overpredict the radial velocity. Near the hub the numerical radial velocity is lower than the measured velocity, excpet for the 23-vaned diffuser with the vane turning angle of 10°, for which the numerical prediction of the radial velocity is spot on. After the diffuser, the numerical profiles are more accurate than before the diffuser. There are no major differences between the two turbulence models.

For the vaneless diffuser, the $k-\omega$-SST turbulence model predicts the performance parameters, such as efficiency, pressure ratio, total pressure loss coefficient, and pressure rise coefficient, better than the $k-\epsilon$ model. The two best geometries according to the $k-\omega$-SST model are also the two best according to the measurements. The $k-\omega$-SST model also predicts the flow field after impeller better than the $k-\epsilon$ model. After the diffuser, the $k-\epsilon$ predicts the flow field better for the unpinched and $b_{2'}/b_2 = 0.903$ cases. For the other three, there are no major differences between the two turbulence models. In general, the flow field predictions after the impeller are better than those after the diffuser. This is most likely due to the problem discussed in chapter 4.2, that total grid nondependecy was not achieved in the diffuser, so the diffuser grid should have been more dense. All in all, the overall accuracy of the $k-\omega$ results is satisfactory, and excellent at times.

Even though the vaned diffuser grid was not dense enough, the flow field predictions are satisfactory. In general, both turbulence models failed to predict the performance parameters for the vaned constructions.

5.5 Conclusions

Eight different diffusers were studied experimentally: five vaneless diffusers and three vaned ones. The vaneless diffusers varied in the diffuser width, so that one of the vaneless diffusers had the diffuser width $b_{2'}/b_2 = 1.0$, which was the basic original geometry to which the results were compared. Three of the other four vaneless diffusers had pinch implemented both at the hub and at the shroud walls, and the diffuser widths $b_{2'}/b_2$ were 0.903, 0.854 and 0.806. The fifth diffuser had pinch only at the shroud wall, and the diffuser width $b_{2'}/b_2$ was 0.903. Two of the vaned diffusers had 23 vanes, and vane turning angles θ of 10° and 15°. The third vaned diffuser had 15 vanes, and the vane turning angle θ was 10°.

The overall performance of the compressor was measured for each construction according to relevant standards. All the pinched geometries had better isentropic total-to-total stage peak efficiency than the unpinched geometry. Also with the pinched diffusers, the peak efficiency area was around the design operating point, while with the unpinched geometry the peak efficiency was achieved only at lower rotational speeds and mass flows. The peak efficiencies were approximately 2 percentage points higher with the pinched diffusers, and the design operating point efficiencies were approximately 4 percentage points higher with the pinched constructions than those of the unpinched one. The pinches studied in this work did not affect the operating range of the compressor significantly. The efficiency increments were clearly more notable at the design and higher flows. The axial angle and velocity profiles after the impeller were more distorted at the design and high flow, so the soothing effects of pinch were more benefical at these flow rates.

Both of the vaned diffusers with the vane turning angle θ of 10° had better peak efficiency than the vaneless unpinched diffuser, the increment being approximately 2 percentage points. The third vaned diffuser (n23,θ15) had approximately the same peak efficiency as the vaneless unpinched construction. The peak efficiency area was located slightly lower than the design mass flows for all the vaned configurations. All vaned diffusers had a considerably narrower operating range. The vaned diffusers choked at lower mass flows and stalled at higher mass flows than the vaneless diffusers. The 23-vaned diffuser with the vane turning of 10° had the highest peak efficiency, but only just. The n23,θ10 diffuser had the highest design point pressure ratios at all rotational speeds, but the difference was only minor.

The static pressure before and and after the diffuser was measured at four different circumferential locations and at three different radius ratios in the diffuser. The total pressure and temperature were measured with Kiel probes at three different circumferential locations, before and after the diffuser. A cobra probe was used to measure the total pressure and flow angle at the fourth circumferential location. These results were then used to calculate the isentropic efficiency and pressure ratio, the pressure loss and rise coefficients, and absolute flow velocity and its radial and tangential components. The flow fields were measured at the design operating speed and with three different mass flows: $q_{\mathrm{m}}/q_{\mathrm{m,des}} = 0.65$, 1.00 and 1.20 for the vaned diffusers, and $q_{\mathrm{m}}/q_{\mathrm{m,des}} = 0.58$, 1.00 and 1.38 for the vaneless ones.

All pinched cases, except the case $b_{2'}/b_2 = 0.903$ (hub & shroud), had better isentropic impeller total-to-static efficiency than the unpinched case at all

three mass flows, except for the case with the most pinch, which had approximately the same impeller efficiency as the unpinched one at the high flow. The $b_{2'}/b_2 = 0.903$ (hub & shroud) had lower impeller efficiency at the low flow, approximately the same impeller efficiency at the design flow, and second highest efficiency at the high flow. The case with only shroud pinch had the best impeller efficiency at all mass flows. It also had the best efficiency over the combined impeller and diffuser. The case with the most pinch had the second highest impeller efficiency. In general, all the pinched geometries had better efficiency over the impeller and diffuser, except for the $b_{2'}/b_2 = 0.903$ (hub & shroud), which had approximately the same efficiency at the low flow as the unpinched diffuser. All the pinched diffusers had better impeller and combined impeller and diffuser total-to-static pressure ratios. There were no significant differences between the different pinches, except for the $b_{2'}/b_2 = 0.903$ (hub & shroud), which had the highest pressure ratios at the high flow. All pinched geometries had a somewhat lower pressure loss coefficient at the diffuser and higher pressure loss coefficient at the volute than the unpinched geometry. All other pinched geometries, except for the $b_{2'}/b_2 = 0.903$ (hub & shroud), had a slightly lower pressure rise coefficient at the diffuser and even lower pressure rise coefficient at the volute. The pinches did not affect the circumferential static pressure distributions, so the worse volute performance was most likely due to the different velocity profile at the diffuser exit.

The pinches made the flow field after the impeller more uniform, and decreased the size of the low flow velocity area, and there were no back flow areas near the shroud. Also the flow fields after the impeller were more uniform with the pinched geometries. In general, the two best constructions were the two cases with the most pinch at the shroud: $b_{2'}/b_2 = 0.806$ and $b_{2'}/b_2 = 0.903$ (shroud), the shroud pinch being slightly better.

All vaned diffusers had lower impeller and combined impeller and diffuser isentropic total-to-static efficiencies than the vaneless unpinched geometry. The impeller total-to-static pressure ratios for the vaned diffusers were lower at the low flow, approximately the same at the design flow, and higher at the high flow. The pressure ratios over the combined impeller and diffuser were higher, except for the 15-vaned diffuser at the high flow. The total pressure loss coefficients at the diffuser were approximately the same at the design flow and at the low flow for the vaned diffusers as those of the unpinched vaneless diffuser. The n23,θ15° had a lower pressure loss coefficient at the volute for all mass flows. The two other diffusers had lower pressure loss coefficients at the volute at the high flow. The static pressure rise coefficients in the

diffuser were higher for all the vaned diffusers at the low and at the design flows and lower at the high flow, when compared to the vaneless unpinched construction. The pressure rise coefficients for the vaned diffusers at the volute were lower at the low and at the design flows and higher at the high flow.

The more vane turning there was, the more radial was the flow at the impeller exit. The best vaned diffuser, in general, seemed to be the n23,θ10. The effect of the vane turning angle to the flow velocities was not so straightforward. At the design flow and at the low flow, the flow decelerated more in the diffuser when the turning angle was smaller, whilst at the high flow the flow decelerated more when the vane turning angle was higher. In general, the vaned diffusers had a more uniform flow field at the diffuser exit than the vaneless unpinched diffuser. The effect of vane number was even more ambiguous, and prehaps it should not be used as a design parameter from the aerodynamic perspective.

A more probable reason for the different angle profiles for the n23,θ10 diffuser is that before the diffuser the angle traversion hole was closer to the diffuser vane than for the other vaned geometries. Also, for this geometry, the angle traversion hole after the diffuser was almost directly at the imaginary extension of the chamber line, which might have caused distortions to the angle and velocity profiles after the diffuser.

When the CFD and measurement results are compared, it seems that the $k-\omega$-SST turbulence model predicts the overall performance better than the $k-\epsilon$ turbulence model. The $k-\omega$-SST model predicts the flow field at the impeller exit slightly better. At the diffuser exit, the $k-\epsilon$ model predicts the flow field better for the unpinched and the $b_{2'}/b_2 = 0.903$ cases, better than the $k-\omega$-SST model. For the other three vaneless cases there are no major differences. For the vaned diffusers both turbulence were equally wrong in their overll performance predictions. The flow field predictions were better, and there were no major differences beteween the the two turbulence models.

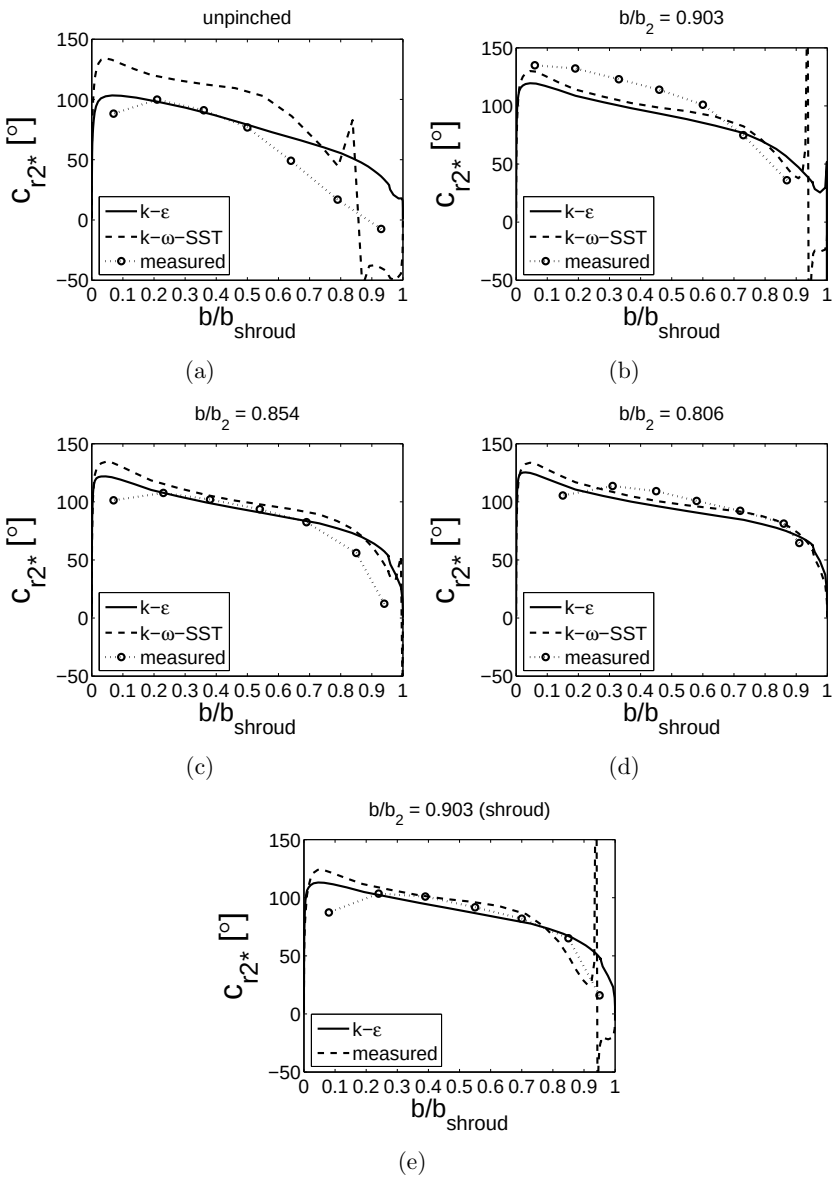

Figure 5.59: Axial radial velocity distributions before the vaneless diffusers, both turbulence models and measurement results. (a) $b_{2'}/b_2 = 1.00$, (b) $b_{2'}/b_2 = 0.903$, (c) $b_{2'}/b_2 = 0.854$, (d) $b_{2'}/b_2 = 0.806$, and (e) $b_{2'}/b_2 = 0.903$ (shroud).

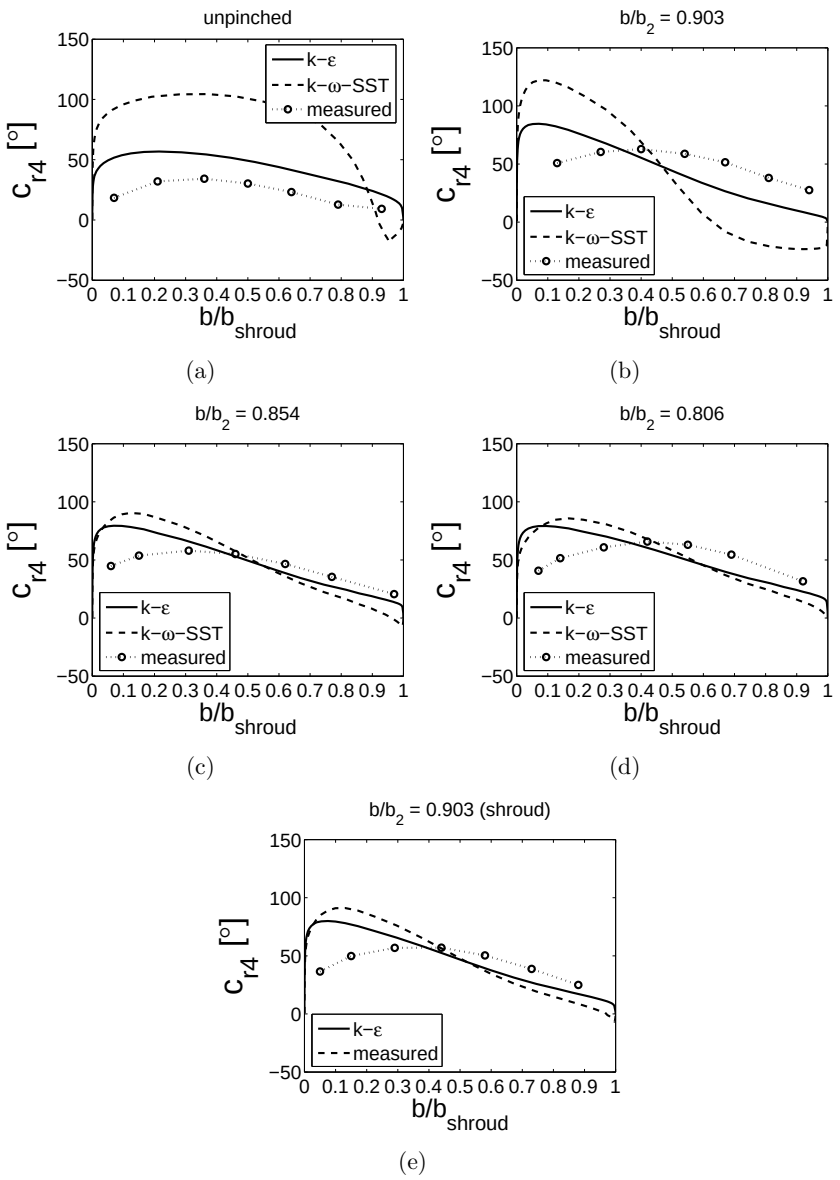

Figure 5.60: Axial radial velocity distributions after the vaneless diffusers, both turbulence models and measurement results. (a) $b_{2'}/b_2 = 1.00$, (b) $b_{2'}/b_2 = 0.903$, (c) $b_{2'}/b_2 = 0.854$, (d) $b_{2'}/b_2 = 0.806$, and (e) $b_{2'}/b_2 = 0.903$ (shroud).

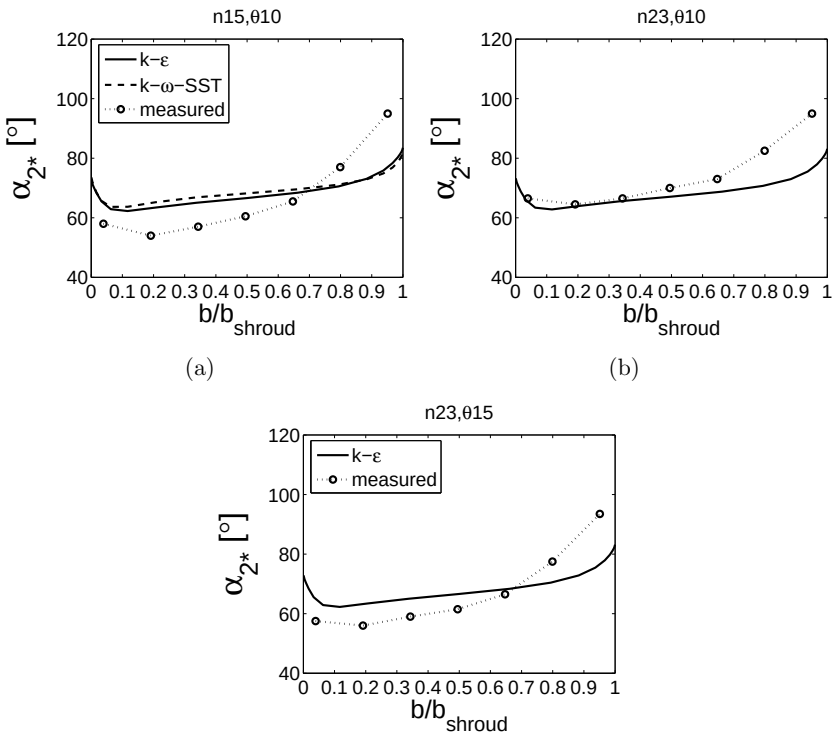

Figure 5.61: Axial flow angle distributions before the vaned diffusers, both turbulence models and measurement results. (a) 15-vaned, (b) 23-vaned, vane turning 10°, and (c) 23-vaned, vane turning 15°.

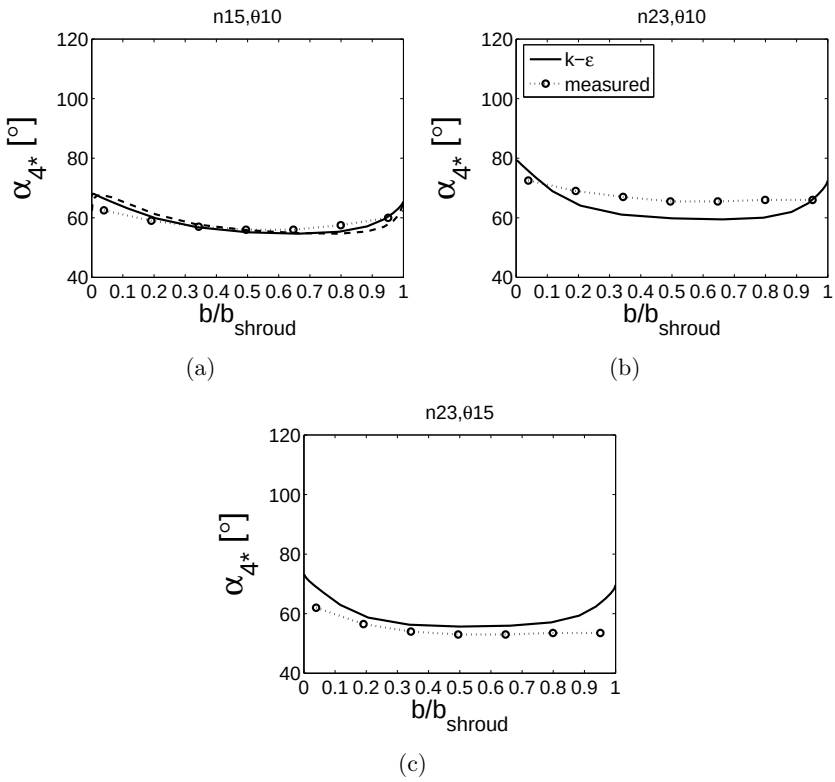

Figure 5.62: Axial flow angle distributions after the vaned diffusers, both turbulence models and measurement results. (a) 15-vaned, (b) 23-vaned, vane turning 10°, and (c) 23-vaned, vane turning 15°.

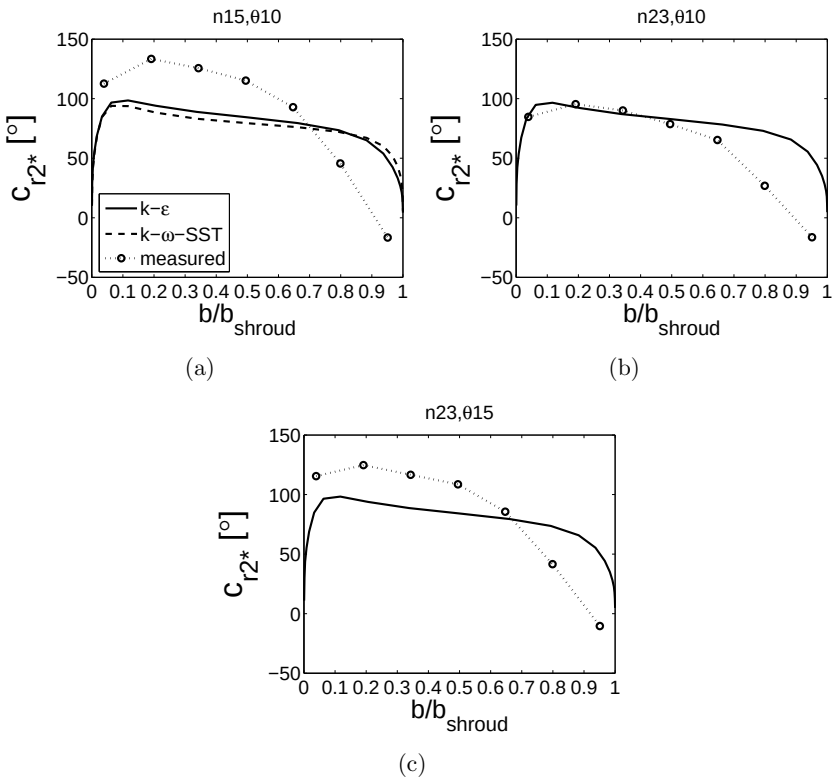

Figure 5.63: Axial radial velocity distributions before the vaned diffusers, both turbulence models and measurement results. (a) 15-vaned, (b) 23-vaned, vane turning 10°, and (c) 23-vaned, vane turning 15°.

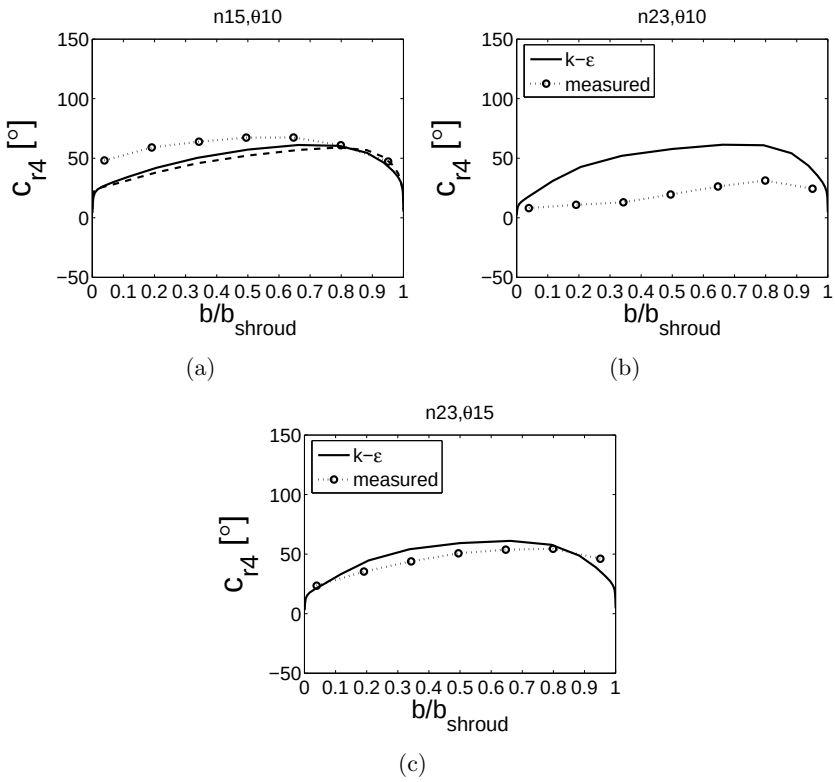

Figure 5.64: Axial radial velocity distributions after the vaned diffusers, both turbulence models and measurement results. (a) 15-vaned, (b) 23-vaned, vane turning 10°, and (c) 23-vaned, vane turning 15°.

6 Conclusions and discussion

The performance and the flow field in centrifugal compressor diffusers were investigated both numerically and experimentally. Five different vaneless diffusers and six different vaned diffusers were studied numerically. The vaneless diffusers varied only by the diffuser width. The vaneless diffusers were: an unpinched one , three diffusers with pinch divided evenly at the hub and at the shroud with diffuser widths $b_{2'}/b_2$ of 0.903, 0.854 and 0.806, and one diffuser with pinch only at the shroud wall and the diffuser width of $b_{2'}/b_2$ = 0.903. Four of the six numerically investigated vaned diffusers had the vane turning angle of 10° and 15, 17, 19 and 23 diffuser vanes, and the two other diffusers had 23 vanes and vane turning angles of 15 and 20°. None of the vaned configurations had pinch implemented to them. In addition to these calculations, a coarse grid sensitivity study was performed and a NASA low speed compressor was also modeled to see how the CFD results would compare to a well measured case. Some of the cases were modeled using two turbulence models: Chien's $k - \epsilon$ and the $k - \omega$-SST.

All the five vaneless and three of the vaned diffusers were also investigated experimentally. The vaned diffusers were the 15-vaned and two of the 23-vaned ones. The 15-vaned diffuser had the vane turning angle of 10°, and the 23-vaned ones had the vane turning angles of 10° and 15°. The compressor operating map was measured for each construction in compliance with relevant standards. The flow fields before and after the diffuser were measured with three Kiel probes to measure the total pressure at three different circumferential locations, a cobra probe to measure the total pressure and flow angle at the fourth circumferential location, and four static pressure taps at four different circumferential locations. Thermocouples were inserted along with the Kiel probes to measure the total temperature. The static pressure was also measured in the diffuser at three different radii at one circumferential location.

When comparing the CFD results to the measurement results, it was evident that the $k - \omega$-SST model predicted the performance and flow field after the impeller better than the $k - \epsilon$ model, as was expected. In the present author's opinion, the $k - \omega$-SST model should be used as a standard turbulence model in this type of centrifugal compressor calculations. However, if the $k - \omega$-SST model is used, more consideration towards the grid must be given. The CFD indicated that it is possible to improve the performance of the centrifugal compressor by implementing pinch. The two best constructions were the two cases with most pinch at the shroud. One interesting result was that pinch

improved also the impeller efficiency. The experimental results indicated the same. This is most likely due to a more uniform flow field at the impeller exit. The pinches also decreased the size of the slow flow region near the shroud at the impeller exit. Another factor most likely improving the impeller efficiency slightly was that according to the CFD results, the pinches decreased the tip clearance mass flow near the impeller blade trailing edge. This should then lead to lower secondary losses, and therefore to a higher impeller efficiency. This effect was more profound with the two geometries with most pinch at the shroud. These two geometries also had the best combined impeller and diffuser efficiency. The $k-\omega$-SST turbulence model results predicted that these two geometries would have 4 percentage points better design operating point efficiency than the unpinched geometry. Also the impeller pressure ratio was slightly higher with these two geometries, but the combined impeller and diffuser pressure ratio was lower. The pressure rise coefficient in the diffuser was lower for the $b_{2'}/b_2 = 0.806$ and higher for the $b_{2'}/b_2 = 0.903$ (shroud), and the total pressure loss coefficients were lower for these two geometries when compared to the unpinched geometry. The diffuser grid in the numerical simulations of the vaneless cases should have been more dense.

For the vaned diffusers, both turbulence models predicted the impeller efficiency to be almost the same as for the unpinched vaneless diffuser. The combined impeller and diffuser efficiency was predicted to be a few percentage points higher. The $k-\epsilon$ model predicted slightly lower impeller and combined pressure ratios, while the $k-\omega$-SST model predicted higher impeller pressure ratios and lower combined pressure ratios. The pressure loss coefficients in the diffuser were higher with the $k-\epsilon$ and lower with the $k-\omega$-SST model, and the pressure rise coefficients were higher for most diffusers with both turbulence models, as compared to those of the vaneless unpinched diffuser. Both turbulence models predicted that the 17- and 19-vaned diffusers would be clearly worse than the 15- and all the 23-vaned diffusers. The $k-\omega$-SST model predicted the flow to separate at the hub near the diffuser exit in the 23-vaned diffuser with the vane turning angle of 15°.

According to the operating map measurements, all the pinched geometries had higher peak efficiency than the unpinched geometry, the increment being approximately 2 percentage points for all the pinched geometries. The peak efficiency for the unpinched geometry was achieved at lower values than the design operating speed and mass flow. The peak efficiency area of the pinched geometries was around the design operating point, and the desing operating point efficiencies were approximately 4 percentage points higher

for the pinched geometries. There were no significant differences between the different pinched cases, and pinch did not affect the operating range significantly. The two vaned diffusers with the vane turning angle of 10° had better a peak efficiency, approximately 2 percentage points higher than the unpinched vaneless diffuser. The third vaned diffuser had the same peak efficiency as the unpinched vaneless diffuser. The peak efficiency of the vaned diffusers occured at higher rotational speeds and at slighly lower mass flows than for the unpinched vaneless construction. The operating range was considerably narrower for the vaned diffusers.

According to the measurements, pinch made the flow field more uniform at the impeller exit and the diffuser exit. The slow flow area after the impeller was smaller and the impeller efficiency was better. The impeller efficiency was best for the case with only shroud pinch. All pinched geometries had higher impeller and combined pressure ratios than the unpinched vaneless one. The pressure loss coefficients in the diffuser were lower for the pinched geometries, and higher in the volute. However, pinch did not affect the circumferential pressure distribution, so the worse volute performance was most likely due to changes in the flow angles and velocities. Also according to the flow field measurements, the two cases with most pinch at the shroud were the two best ones.

In general, it is possible to improve the performance of a centrifugal compressor with pinch. Shroud pinch seems to be slighly better than pinch at both the hub and at the shroud walls. The two best cases were the ones with most pinch at the shroud, the pinch being approximately twice the height of the tip clearance. The other pinched geometries had shroud pinches of approximately 0.5 and 1 times the height of the tip clearance. To the author, it seems that the pinch should be at least the height of the tip clearance, in order to offer sufficient benefit, preferably more. The vaned diffusers are more expensive to manufacture and they narrow the operating range considerably, so there is no point in using the vaned diffusers studied here at these pressure levels. The pinched diffuser is also quite easy to retrofit to an existing compressor.

The best vaned diffuser geometries had higher peak efficiency than the unpinched vaneless geometry. According to the flow field measurements, the 23-vaned diffuser with the vane turning angle of 10° seemed to be the best vaned diffuser. The vaned diffusers studied here were most likely poorly designed, because it is possible to achieve better efficiency increments with the vaned diffusers. When the vaned diffusers were originally designed, the vane set-

ting angle was chosen from the vaneless unpinched measurements performed previously. The average flow angle was chosen as the diffuser vane setting angle. The idea was that then the average incidence at the design flow would be zero. However, as most of the mass flow goes near the hub where the flow is more radial, the incidence there is quite negative at the design flow. When the mass flow is reduced, the incidence near the hub increases, so the peak performance of the vaned diffusers should occur at lower than design mass flow, which seems to be the case according to compressor operating maps. At the design rotational speed, at the point where the peak efficiency of the best vaned diffuser is achieved, the efficiency increment is approximately 4 percentage points to that of the vaneless unpinched construction. All in all, in the author's opinion, if two-dimensional diffuser vanes are preferred, it should be considered choosing the vane setting angle so that the incidence is zero near the hub, where most of the mass flow passes through the diffuser. Perhaps then the peak efficiency point of the vaned diffuser would be closer to the design operating point. In the author's opinion, the number of diffuser vanes should probably not be used as a design parameter, from the aerodynamic perspective.

All in all it, seems that the benefits of moderate pinches outnumber the possible defects, so pinch should be included in any design, and, in the author's opinion, preferably to the shroud. Pinch should also make it possible to design longer diffusers, which would then recover more of the kinetic energy. Pinch deteriorates the volute performance somewhat, but if a longer diffuser is designed, the volute is relatively simple to redesign. In the future, there is still need for more research considering pinch. There is no certainty that the pinches studied here are the best possible, so geometries with even more pinch should be investigated. There may also be a need to form some general guidelines for pinch design to be included in the preliminary one-dimensional design of the centrifugal compressor.

References

(2003). ISO 5167 Measurement of Fluid Flow by Means of Pressure Differential Devices Insterted in Circular Cross-Section Conduits Running Full.

(2005). ISO 5389 Turbocompressors - Perfomance Test Code.

Abidogun, K. B. (2002). Effects of Vaneless Diffuser Geometries on Rotating Stall. In *IPC2002-27203, 4th International Pipeline Conference, ASME*.

Ayder, E. and Van den Braembussche, R. (1994). Numerical Analysis of the Three-Dimensional Swirling Flow in Centrifugal Compressor Volutes. *Journal of Turbomachinery*, 116(3):462–468.

Cellai, A., De Lucia, M., Ferrara, G., Ferrari, L., Mengoni, C., and Baldassarre, L. (2003a). Application of Low Solidity Vaned Diffuser to Prevent Rotating Stall in Centrifugal Compressors: Experimental Investigation. In *GT-2003-38386, ASME TURBO EXPO*.

Cellai, A., Ferrara, G., Ferrari, L., Mengoni, C., and Baldassarre, L. (2003b). Experimental Investigation and Characterization of the Rotating Stall in a High Pressure Centrifugal Compressor Part III: Influence of Diffuser Geometry on Stall Inception and Perfomance (2nd Impeller Tested). In *GT2003-38390, ASME TURBO EXPO*.

Chien, K. (1982). Predictions of Channel and Boundary-Layer Flows with a Low-Reynolds-Number Turbulence Model. *AIAA Journal*, 20(1):33–38.

Clements, W. and Artt, D. (1989). The Influence of Diffuser Vane Leading Edge Geometry on the Perfomance of a Centrifugal Compressor. In *89-GT-169, Gas Turbine and Aeroengine Congress and Exposition, ASME*.

Di Liberti, J.-L., Wilmsen, B., and Engeda, A. (1996). The Effect of the Vaneless Diffuser Width on the Performance of a Centrifugal Compressor. In *FED vol. 237, pp 797-803. Fluids Engineering Division Conference, ASME*.

Eckardt, D. (1975). Instantaneous Measurements in the Jet-Wake Discharge of Centrifugal Compressor Impeller. *Journal of Engineering for Power*, 97:337–346.

Engeda, A. (1998). Design and Investigation of Four Low Solidity Vaned Diffusers to Assess the Effect of Solidity and Vane Number. In *98-GT-252, International Gas Turbine & Aeroengine Congress & Exhibition, ASME*.

Engeda, A. (2001). The Unsteady Perfomance of Centrifugal Compressors with Different Diffusers PART 1: Results of Vaneless and Conventional Vaned Diffuser. In *FEDSM2001-18267, Fluids Engineering Division Summer Meeting*.

Engeda, A. (2002). The Influence of a Diffuser Width on the Unsteady Performance of a Centrifugal Compressor Stage. In *FEDSM2002-31250, Fluids Engineering Division Summer Meeting, ASME*.

Engeda, A. (2003). Experimental and Numerical Investigation of the Performance of a 240 kW Centrifugal Compressor with Different Diffusers. *Experimental Thermal and Fluid Science*, 28(1):55–72.

Ferrara, G., Ferrari, F., and Baldassarre, L. (2004). Rotating Stall in Centrifugal Compressor Vaneless Diffuser: Experimental Analysis of Geometrical Parameters Influence on Phenomenon Evolution. *International Journal of Rotating Machinery*, 10:433–442.

Ferrara, G., Ferrari, L., Mengoni, C., P., De Lucia, M., and Baldassarre, L. (2002a). Experimental Investigation and Characterization of the Rotating Stall in a High Pressure Centrifugal Compressor Part I: Influence of Diffuser Geometry on Stall Inception. In *GT-2002-30389, ASME TURBO EXPO*.

Ferrara, G., Ferrari, L., Mengoni, C., P., De Lucia, M., and Baldassarre, L. (2002b). Experimental Investigation and Characterization of the Rotating Stall in a High Pressure Centrifugal Compressor Part II: Influence of Diffuser Geometry on Stage Performance. In *GT-2002-30390, ASME TURBO EXPO*.

Gallier, K., Lawless, P. B., and Fleeter, S. (2007). PIV Characterization of High Speed Centrifugal Compressor Impeller-Diffuser Interaction. In *AIAA/ASME/SAE/ASEE Joint Propulsion Conference, AIAA 2007-5019*.

Hagelstein, D., Hillewaert, K., Van den Braembussche, R., Engeda, A., Keiper, R., and Rautenberg, M. (2000). Experimental and Numerical Investigation of the Flow in a Centrifugal Compressor Volute. *Journal of Turbomachinery*, 122:22.

Hathaway, M., Chriss, R., Strazisar, A., and Wood, J. (1995). Laser Anemometer measurements of Three-Dimensional Rotor Flow Field in the NASA Low-Speed Centrifugal Compressor. Technical report, NASA Technical Paper 3527.

He, N. and Tourlidakis, A. (2001). Analysis of Diffusers with Different Number of Vanes in a Centrifugal Compressor Stage. In *2001-GT-0321, ASME TURBO EXPO*.

Hellsten, A. (1998). On the Solid-Wall Boundary Condition of ω in the $k-\omega$-Type Turbulence Models. Report B-50, Laboratory of Aerodynamics, Helsinki University of technology.

Hellsten, A. (2004). *New Two-Equation Turbulence Model for Aerodynamics Applications*. PhD thesis, Helsinki Univeristy of Technology.

Hellsten, A. and Laine, S. (1997). Extension of the $k-\omega$-SST Turbulence Model for Flows Over Rough Surfaces. In *AIAA Paper 97-3577-CP*.

Hohlweg, W., Direnzi, L., and Aungier, R. (1993). Comparison of Conventional and Low Solidity Vaned Diffusers. In *93-GT-98, International Gas Turbine and Aeroengine Congress and Exposition, ASME*.

Issac, J., Sitaram, N., and Govardhan, M. (2003). Performance and Wall Static Pressure Measurements on Centrifugal Compressor Diffusers. *Proceedings of the Institution of Mechanical Engineers, Part A: Journal of Power and Energy*, 217(5):547–558.

Issac, J., Sitaram, N., and Govardhan, M. (2004). Effect of Diffuser Vane Height and Position on the Performance of a Centrifugal Compressor. *Proceedings of the Institution of Mechanical Engineers, Part A: Journal of Power and Energy*, 218(8):647–654.

Jones, B. and Launder, W. (1972). The Prediction of Laminarization with a Two-Equation Model of Turbulence. *International Journal of Heat and Mass Transfer*, 15:301–314.

Justen, F., Ziegler, K., and Gallus, H. (1999). Experimental Investigation of Unsteady Flow Phenomena in a Centrifugal Compressor Vaned Diffuser of Variable Geometry. *Journal of Turbomachinery*, 121:763.

Kim, W. and Engeda, A. (1997). Comparison of Pressure Recovery and Overall Performance of Different Diffusers for Centrifugal Compressor. In *FEDSM97-3029 Fluids Engineering Division Summer Meeting, ASME*.

Kim, Y., Engeda, A., Aungier, R., and Amineni, N. (2002). A Centrifugal Compressor Stage with Wide Flow Range Vaned Diffusers and Different Inlet Configurations. *Proceedings of the Institution of Mechanical Engineers, Part A: Journal of Power and Energy*, 216(4):307–320.

Krain, H. (1988). Swirling Impeller Flow. *Journal of turbomachinery*, 110(1):122–128.

Lee, Y., Luo, L., and Bein, T. (2001). Direct Method for Optimization of a Centrifugal Compressor Vaneless Diffuser. *Journal of Turbomachinery*, 123:73.

Liu, R. and Xu, Z. (2004). Numerical Investigation of a High-Speed Centrifugal Compressor with Hub Vane Diffusers. *Proceedings of the Institution of Mechanical Engineers, Part A: Journal of Power and Energy*, 218(3):155–169.

Ludtke, K. (1983). Aerodynamic Tests on Centrifugal Process Compressors - The Influence of the Vaneless Diffusor. *Journal of engineering for power*, 105(4):902–909.

Menter, F. (1992). Improved Two-Equation $k - \omega$ Turbulence Models for Aerodynamic Flows. Technical report, NASA.

Pinarbasi, A. and Johnson, M. (1994a). Detailed flow measurements in a centrifugal compressor vaneless diffuser. *Journal of Turbomachinery*, 116(3):453–460.

Pinarbasi, A. and Johnson, M. (1995a). Experimental Flow Field Investigation in a Centrifugal Compressor Vaned Diffuser. In *95-GT-80, International Gas Turbine and Aeroengine Congress and Exposition, ASME.*

Pinarbasi, A. and Johnson, M. (1995b). Off-Design Flow Measurements in a Centrifugal Compressor Vaneless Diffuser. *Journal of Turbomachinery*, 117:602.

Pinarbasi, A. and Johnson, M. (1996). Detailed Stress Tensor Measurements in a Centrifugal Compressor Vaneless Diffuser. *Journal of Turbomachinery*, 118:394.

Pinarbasi, A. and Johnson, M. (1997). Detailed Off Design Flow Measurements in a Centrifugal Compressor Vaned Diffuser. In *97-GT-343, International Gas Turbine and Aeroengine Congress and Exhibition, ASME.*

Pinarbasi, A. and Johnson, M. W. (1994b). Off Design Reynolds Stress Tensor Measurements in a Centrifugal Compressor Vaneless Diffuser. In *FED-Vol. 203, Turbulence in Complex Flows, ASME.*

Rautaheimo, P., Salminen, E., and Siikonen, T. (1999). Numerical Simulation of the Flow in the NASA Low-Speed Centrifugal Compressor, Technical report No. 119. Technical report, Helsinki University of Technology, Laboratory of Applied Thermodynamics.

Reunanen, A. (2001). *Experimental and Numerical Analysis of Different Volutes in a Centrifugal Compressor*. PhD thesis, Lappeenranta University of Technology.

Sallinen, P. and Backman, J. (2003). Additional Information to the Report "Compressor Testing Facility" - HST-Compressor Testing Facility Measurements; A Detailed Description and Uncertainty Calculation. Technical report, Laboratory of Fluid Dynamics, Lappeenranta University of Technlogy, Unpublished, Internal Report.

Seidel, U. (1994). *Radialverdichter-Kennfeldregelung mittels Nachleitrad*. PhD thesis, Leibniz Universität Hannover.

Senoo, Y. and Kinoshita, Y. (1977). Influence of Inlet Flow Conditions and Geometries of Centrifugal Vaneless Diffusers on Critical Flow Angle for Reverse Flow. *Journal of Fluids Engineering*, 99:98–103.

Shaaban, S. and Seume, J. (2007). Aerodynamic Perfomance of Small Turbocharger Compressors. In *GT2007-27558, ASME TURBO EXPO*.

Shum, Y., Tan, C., and Cumpsty, N. (2000). Impeller–Diffuser Interaction in a Centrifugal Compressor. *Journal of Turbomachinery*, 122:777.

Siikonen, T., Rautaheimo, P., and Salminen, E. (2004). *FINFLO User Guide, version 7.2*. Finflo Ltd.

Stahlecker, D. and Gyarmathy, G. (1998). Investigations of Turbulent Flow in a Centrifugal Compressor Vaned Diffuser by 3-component Laser Velocimetry. In *98-GT-300, Gas Turbine and Aeroengine Congress and Exhibition, ASME*.

Tang, J. (2006). *Computational Analysis and Optimization of Real Gas Flow in Small Centrifugal Compressors*. PhD thesis, Lappeenranta University of Technology.

Turunen-Saaresti, T. (2004). *Computational and Experimental Analysis of Flow Field in the Diffusers of Centrifugal Compressors*. PhD thesis, Lappeenranta University of Technology.

Turunen-Saaresti, T., Grönman, A.-P., and Jaatinen, A. (2009). Experimental Study of Pinch in Vaneless Diffuser of Centrifugal Compressor. In *GT2009-60162, ASME TURBO EXPO*.

Turunen-Saaresti, T., Reunanen, A., and Larjola, J. (2006). Computational and Experimental Study of Pinch on the Performance of a Vaneless Diffuser in a Cntrifugal Compressor. *Journal of Thermal Science*, 15(4):306–313.

Van den Braembuscsche, R. A., Frigne, P., and Roustan, M. (1980). Rotating Non-Uniform Flow in Radial Compressors. In *Proc. No. 282 AGARD Conference*.

Van den Braembussche, R., Ayder, E., Hagelstein, D., Rautenberg, M., and Keiper, R. (1999). Improved Model for the Design and Analysis of Centrifugal Compressor Volutes. *Journal of Turbomachinery*, 121:619.

Wilcox, D. (1988). Reassessment of the Scale-Determining Equations for Advanced Turbulence Models. *AIAA Journal*, 26:1299–1310.

Wilcox, D. (1998). *Turbulence Modeling for CFD*. DCW Industries, 2nd edition.

Yingkang, Z. and Sjolander, S. A. (1987). Effect of Geometry on the Performance of Radial Vaneless Diffusers. *Journal of Turbomachinery*, 109:550–556.

Yoshinaga, Y., Kaneki, T., Kobayashi, H., and Hoshino, M. (1987). A study of Performance Improvement for High Specific Speed Centrifugal Compressors by Using Diffusers with Half Guide Vanes. *Journal of fluids engineering*, 109(4):359–367.

Ziegler, K., Gallus, H., and Niehuis, R. (2003a). A Study on Impeller-Diffuser Interaction—Part I: Influence on the Performance. *Journal of Turbomachinery*, 125:173.

Ziegler, K., Gallus, H., and Niehuis, R. (2003b). A Study on Impeller-Diffuser Interaction—Part II: Detailed Flow Analysis. *Journal of Turbomachinery*, 125:183.

A Measurement uncertainty

The measurement uncertainties have been calculated according to an internal laboratory report (Sallinen and Backman, 2003), and for each measurement maximum relative uncertainty is given. For the operating map measurements, the uncertainty for the mass flow $e_{\mathrm{q_m}}$ is

$$\begin{aligned} e_{\mathrm{q_m}} &= [\left(e_{\mathrm{C}}\frac{\partial q_{\mathrm{m}}}{\partial C}\right)^2 + \left(e_{\epsilon}\frac{\partial q_{\mathrm{m}}}{\partial \epsilon}\right)^2 + \left(e_{\mathrm{d}}\frac{\partial q_{\mathrm{m}}}{\partial d}\right)^2 \\ &+ \left(e_{\Delta\mathrm{p}}\frac{\partial q_{\mathrm{m}}}{\partial \Delta p}\right)^2 + \left(e_{\rho}\frac{\partial q_{\mathrm{m}}}{\partial \rho}\right)^2 + \left(e_{\mathrm{D}}\frac{\partial q_{\mathrm{m}}}{\partial D}\right)^2]^{0.5} \end{aligned} \tag{A.1}$$

and the relative uncertainty for the mass flow $E_{\mathrm{q_m}}$ is

$$E_{\mathrm{q_m}} = \frac{e_{\mathrm{q_m}}}{q_{\mathrm{m}}} \tag{A.2}$$

After the partial differentiations in Eq. A.1 and then inserting that equation to Eq. A.2, the relative uncertainty for the mass flow is

$$\begin{aligned} E_{\mathrm{q_m}} &= [(E_{\mathrm{C}})^2 + (E_{\epsilon})^2 + \left(2E_{\mathrm{d}}\left(1 + \frac{\beta^4}{1-\beta^4}\right)\right)^2 \\ &+ \left(\frac{E_{\Delta\mathrm{p}}}{2}\right)^2 + \left(\frac{E_{\rho}}{2}\right)^2 + \left(2E_{\mathrm{D}}\left(\frac{\beta^4}{1-\beta^4}\right)\right)^2]^{0.5} \end{aligned} \tag{A.3}$$

The relative uncertainties for the coefficient of discharge E_{C}, the pipe diameter E_{D} and the nozzle orifice diameter E_{d} arise from the geometry. Also the diameter ratio of the nozzle β arises from the geometry of the nozzle. For the pressure difference over the nozzle Δp the relative uncertainty is that of the pressure difference transducer and the relative uncertainty for the expansibilty factor E_{ϵ} is

$$E_{\epsilon} = 0.02\frac{\Delta p}{p} \tag{A.4}$$

where the Δp is the pressure difference over the nozzle and p is the pressure at the nozzle. The density is calculated using the pressure, the temperature, and the specific gas constant. The relative uncertainty for the density is

$$E_{\rho} = \left[\left(\frac{e_{\mathrm{p}}}{p}\right)^2 + \left(\frac{e_{\mathrm{T}}}{T}\right)^2 + \left(\frac{e_{\mathrm{R}}}{R}\right)^2\right]^{0.5} \tag{A.5}$$

the uncertainties for the pressure and the temperature arise from the instruments, and the uncertainty for the specific gas constant E_{R} is

$$e_{\mathrm{R}} = \left[\left(e_{\omega_{\mathrm{v}}} \frac{\partial R}{\partial \omega_{\mathrm{v}}} \right)^2 \right]^{0.5} \tag{A.6}$$

where the uncertainty of the water vapour content $e_{\omega_{\mathrm{v}}}$ is

$$e_{\omega_{\mathrm{v}}} = \left[\left(e_{\varphi} \frac{\partial \omega_{\mathrm{v}}}{\partial \varphi} \right)^2 \right]^{0.5} \tag{A.7}$$

The uncertainty for the relative humdity e_{φ} comes from the instrument. In a similar fashion, the uncertainty for the efficiency is

$$\begin{aligned} e_{\eta} &= [\left(e_{\mathrm{T_{t1}}} \frac{\partial \eta}{\partial T_{\mathrm{t1}}} \right)^2 + \left(e_{\mathrm{T_{t2}}} \frac{\partial \eta}{\partial T_{\mathrm{t2}}} \right)^2 + \left(e_{\mathrm{T_{t2}-T_{t1}}} \frac{\partial \eta}{\partial \left(T_{\mathrm{t2}} - T_{\mathrm{t1}} \right)} \right)^2 \\ &+ \left(e_{\pi} \frac{\partial \eta}{\partial \pi} \right)^2 + \left(e_{\mathrm{R}} \frac{\partial \eta}{\partial R} \right)^2 + \left(e_{\overline{\mathrm{c_p}}} \frac{\partial \eta}{\partial \overline{c_{\mathrm{p}}}} \right)^2]^{0.5} \end{aligned} \tag{A.8}$$

and the relative uncertainty for efficiency E_{η} is

$$E_{\eta} = \frac{e_{\eta}}{\eta} \tag{A.9}$$

The uncertainties for the temperature measurements are straightforward and arise from the instruments. The uncertainty for the specific gas constant is calculated with Eq A.6. The uncertainty for the pressure ratio e_{π} is

$$e_{\pi} = \left[\left(e_{\mathrm{p_1}} \frac{\partial \pi}{\partial p_1} \right)^2 + \left(e_{\mathrm{p_2}} \frac{\partial \pi}{\partial p_2} \right)^2 \right]^{0.5} \tag{A.10}$$

where the uncertainties for the pressures e_{p} arise from the pressure transducers. The uncertainty for the specific heat capacity $e_{\overline{\mathrm{c_p}}}$ is

$$e_{\overline{\mathrm{c_p}}} = \left[\left(e_{\overline{\mathrm{T}}} \frac{\partial \overline{c_{\mathrm{p}}}}{\partial \overline{T}} \right)^2 + \left(e_{\omega_{\mathrm{v}}} \frac{\partial \overline{c_{\mathrm{p}}}}{\partial \omega_{\mathrm{v}}} \right)^2 \right]^{0.5} \tag{A.11}$$

where the uncertainty for the temperature arises, as before, from the instrumentation, and the uncertainty for the water vapour content ω_{v} can be calculated with Eq A.7. The total relative uncertainty in the total pressure ratio is

$$E_{\pi,\mathrm{tot}} = \left[\left(\ln \left(\frac{p_2}{p_1} \right) \right)^2 \left(4E_{\mathrm{f}}^2 + E_{\mathrm{T}_1}^2 \right) + E_{\mathrm{p}_1}^2 + E_{\mathrm{p}_2}^2 \right]^{0.5} \tag{A.12}$$

The maximum relative uncertainties, using the 95.4% confidence interval, for the mass flow, total efficiency and total pressure ratios are:

$$\begin{aligned} E_{\mathrm{q_m},95.4} &= \pm 0.48\% \\ E_{\eta,95.4} &= \pm 1.34\% \\ E_{\pi,95.4} &= \pm 0.93\% \end{aligned} \tag{A.13}$$

The above-mentioned uncertainties are for single measurements. The points used to draw the operating maps (Figs. 5.7-5.14) are mean values of ten different measurements, so in practice the uncertainties are smaller. These uncertainties can also be used to estimate the uncertainties for the pressure ratios and efficiencies when the impeller, diffuser and volute performances are considered.

The absolute flow velocity has been calculated using the total and static pressures p_{t} and p, the total temperature T_{t}, the specific heat capacity c_{p}, and the specific gas constant R. The uncertainty for the absolute velocity can be estimated with

$$\begin{aligned} e_{\mathrm{c}} &= [\left(e_{\mathrm{c_p}} \frac{\partial c}{\partial c_{\mathrm{p}}} \right)^2 + \left(e_{\mathrm{R}} \frac{\partial c}{\partial R} \right)^2 + \left(e_{\mathrm{p}} \frac{\partial c}{\partial p} \right)^2 \\ &+ \left(e_{\mathrm{p_t}} \frac{\partial c}{\partial p_{\mathrm{t}}} \right)^2 + \left(e_{\mathrm{T_t}} \frac{\partial c}{\partial T_{\mathrm{t}}} \right)^2]^{0.5} \end{aligned} \tag{A.14}$$

where the uncertainties for the pressures and the temperature arise from the instrumentation, and the uncertainties for the specific heat capacity and gas constant can be obtained with Eqs. A.11 and A.6, respectively. The maximum relative uncertainties occur when the flow velocities are smaller. If the velocities are larger, the uncertainty is smaller.

The flow angles had to be read manually from the scale of the traversion device, and therefore a reasonable accuracy to take the angle from the scale was approximately $\pm 0.5°$. The pressure transducer used to measure the pressure difference between the left and right holes of the cobra probe was calibrated to small pressure differences, so it is presumable that the manual reading has caused almost all uncertainty in the angle measurements.

The radial and tangential components of the absolute flow velocities have been calculated using the absolute flow velocity and the flow angle. The uncertainty of the radial velocity, caused by the uncertainty in the angle measurement, is estimated to be

$$\begin{aligned} \left|e_{\mathrm{c_r}}\right|_{\alpha} &= c_{\mathrm{r1}} - c_{\mathrm{r2}} \\ &= c\cos\alpha_1 - c\cos\alpha_2 \\ &= c\left(\cos\alpha_1 - \cos\left(\alpha_1 \pm e_{\alpha}\right)\right) \end{aligned} \tag{A.15}$$

and similarly to the tangential velocity

$$\left|e_{\mathrm{c_t}}\right|_{\alpha} = c\left(\sin\alpha_1 - \sin\left(\alpha_1 \pm e_{\alpha}\right)\right) \tag{A.16}$$

The uncertainties caused by the uncertainties in the angle measurements need to be combined with the uncertainties in the absolute velocity measurements, which causes most of the uncertainty in the radial and tangential components. The uncertainties in the pressure distributions arise directly from the pressure transducers. The maximum relative uncertainties in the flow field measurements are then:

$$\begin{aligned} E_{\mathrm{c}} &= \pm 5.4\% \\ E_{\alpha} &= \pm 1.4\% \\ E_{\mathrm{c_r}} &= \pm 5.5\% \\ E_{\mathrm{c_t}} &= \pm 5.5\% \\ E_{\mathrm{p}} &= \pm 0.25\% \end{aligned} \tag{A.17}$$

ACTA UNIVERSITATIS LAPPEENRANTAENSIS

308. PELTOLA, SATU. Capability matrix – identifying and evaluating the key capabilities of purchasing and supply management. 2008. Diss.

309. HONKAPURO, SAMULI. Performance benchmarking and incentive regulation – considerations of directing signals for electricity distribution companies. 2008. Diss.

310. KORHONEN, KIRSI. Facilitating coordination improvement efforts in cross-functional process development programs. 2008. Diss.

311. RITVANEN, VIRPI. Purchasing and supply management capabilities in Finnish medium-sized enterprises. 2008. Diss.

312. PYNNÖNEN, MIKKO. Customer driven business model – connecting customer value to firm resources in ICT value networks. 2008. Diss.

313. AL NAZER, RAMI. Flexible multibody simulation approach in the dynamic analysis of bone strains during physical activity. 2008. Diss.

314. The Proceedings of the 7th MiNEMA Workshop. Middleware for Network Eccentric and Mobile Applications. Ed. by Pekka Jäppinen, Jouni Ikonen and Jari Porras. 2008.

315. VÄÄTÄNEN, JUHA. Russian enterprise restructuring – the effect of privatisation and market liberalisation on the performance of large enterprises. 2008. Diss.

316. DABAGHMESHIN, MAHSA. Modeling the transport phenomena within the arterial wall: porous media approach. 2008. Diss.

317. HAIMALA, JUHA. Supplier´s position in project marketing networks. 2008. Diss.

318. UOTILA, TUOMO. The use of future-oriented knowledge in regional innovation processes: research on knowledge generation, transfer and conversion. 2008. Diss.

319. LAPPALAINEN, TOMMI. Validation of plant dynamic model by online and laboratory measurements – a tool to predict online COD loads out of production of mechanical printing papers. 2008. Diss.

320. KOSONEN, ANTTI. Power line communication in motor cables of variable-speed electric drives – analysis and implementation. 2008. Diss.

321. HANNUKAINEN, PETRI. Non-linear journal bearing model for analysis of superharmonic vibrations of rotor systems. 2008. Diss.

322. SAASTAMOINEN, KALLE. Many valued algebraic structures as measures of comparison. 2008. Diss.

323. PEUHU, LEENA. Liiketoimintastrategisten vaatimusten syntyminen ja niiden toteutumisen arviointi keskisuurten yritysten toiminnanohjausjärjestelmähankkeissa: Tapaustutkimus kolmesta teollisuusyrityksestä ja aineistolähtöinen teoria. 2008. Diss.

324. BANZUZI, KUKKA. Trigger and data link system for CMS resistive plate chambers at the LHC accelerator. 2008. Diss.

325. HIETANEN, HERKKO. The pursuit of efficient copyright licensing – How some rights reserved attempts to solve the problems of all rights reserved. 2008. Diss.

326. SINTONEN, SANNA. Older consumers adopting information and communication technology: Evaluating opportunities for health care applications. 2008. Diss.

327. KUPARINEN, TONI. Reconstruction and analysis of surface variation using photometric stereo. 2008. Diss.

328. SEPPÄNEN, RISTO. Trust in inter-organizational relationships. 2008. Diss.

329. VISKARI, KIRSI. Drivers and barriers of collaboration in the value chain of paperboard-packed consumer goods. 2008. Diss.

330. KOLEHMAINEN, EERO. Process intensification: From optimised flow patterns to microprocess technology. 2008. Diss.

331. KUOSA, MARKKU. Modeling reaction kinetics and mass transfer in ozonation in water solutions. 2008. Diss.

332. KYRKI, ANNA. Offshore sourcing in software development: Case studies of Finnish-Russian cooperation. 2008. Diss.

333. JAFARI, AREZOU. CFD simulation of complex phenomena containing suspensions and flow through porous media. 2008. Diss.

334. KOIVUNIEMI, JOUNI. Managing the front end of innovation in a networked company environment – Combining strategy, processes and systems of innovation. 2008. Diss.

335. KOSONEN, MIIA. Knowledge sharing in virtual communities. 2008. Diss.

336. NIEMI, PETRI. Improving the effectiveness of supply chain development work – an expert role perspective. 2008. Diss.

337. LEPISTÖ-JOHANSSON, PIIA. Making sense of women managers´ identities through the constructions of managerial career and gender. 2009. Diss.

338. HYRKÄS, ELINA. Osaamisen johtaminen Suomen kunnissa. 2009. Diss.

339. LAIHANEN, ANNA-LEENA. Ajopuusta asiantuntijaksi – luottamushenkilöarvioinnin merkitys kunnan johtamisessa ja päätöksenteossa. 2009. Diss.

340. KUKKURAINEN, PAAVO. Fuzzy subgroups, algebraic and topological points of view and complex analysis. 2009. Diss.

341. SÄRKIMÄKI, VILLE. Radio frequency measurement method for detecting bearing currents in induction motors. 2009. Diss.

342. SARANEN, JUHA. Enhancing the efficiency of freight transport by using simulation. 2009. Diss.

343. SALEEM, KASHIF. Essays on pricing of risk and international linkage of Russian stock market. 2009. Diss.

344. HUANG, JIEHUA. Managerial careers in the IT industry: Women in China and in Finland. 2009. Diss.

345. LAMPELA, HANNELE. Inter-organizational learning within and by innovation networks. 2009. Diss.

346. LUORANEN, MIKA. Methods for assessing the sustainability of integrated municipal waste management and energy supply systems. 2009. Diss.

347. KORKEALAAKSO, PASI. Real-time simulation of mobile and industrial machines using the multibody simulation approach. 2009. Diss.

348. UKKO, JUHANI. Managing through measurement: A framework for successful operative level performance measurement. 2009. Diss.

349. JUUTILAINEN, MATTI. Towards open access networks – prototyping with the Lappeenranta model. 2009. Diss.